Democratic and Popular Algerian Republic Ministry of Higher Education and Scientific Research

A. MIRA UNIVERSITY - BEJAIA

جامعة بجاية
Tasdawit n Bgayet
Université de Béjaïa

Faculty of Technology

Department of Mechanical Engineering

Laboratory of Mechanics, Materials and Energy (L2ME)

PhD Dissertation

In partial Fulfilment of the Requirement for the Degree of DOCTORATE

Domain: Science and Technology

Field: Mechanical Engineering

Specialty: Materials Engineering

Presented By

Mr. HARA Hamza

Title

Synthesis and Characterization of an Alumina-Based Powder Doped with Cobalt and Manganese by the Sol-Gel Method

Defended on 14/02/2026

In front of the Jury composed of:

First and last names	Grade		
Mr SAD-EDDINE Abdelhamid	Professor	Univ. of Bejaia	President
Mr YOUNES Rassim	Professor	Univ. of Bejaia	Thesis director
Mr BRADAI Mohand Amokrane	Professor	Univ. of Bejaia	Thesis co-director
Mr BENABBAS Abderrahim	Professor	Univ. of Bouira	Examiner
Mr AKNOUCHE Hamid	Professor	Univ. of Boumerdes	Examiner

Academic year : 2025/2026

République Algérienne Démocratique et Populaire
Ministère de l'Enseignement Supérieur et de la Recherche Scientifique
UNIVERSITE A. MIRA - BEJAIA

جامعة بجاية
Tasdawit n Bgayet
Université de Béjaïa

Faculté de Technologie

Département de Génie Mécanique

Laboratoire de Mécanique, Matériaux et Energétique (L2ME)

THÈSE

EN VUE DE L'OBTENTION DU DIPLOME DE DOCTORAT

Domaine : Sciences et Technologies

Filière : Génie Mécanique

Spécialité : Génie des Matériaux

Présentée

Par

Mr. HARA Hamza

Thème

Synthèse et caractérisation d'une poudre à base d'alumine dopée au cobalt et au manganèse par voie sol-gel.

Soutenue le 14/02/2026

Devant le jury composé de MM.

Noms et Prénoms	Grade		
Mr SAD-EDDINE Abdelhamid	Professeur	Univ. de Bejaia	Président
Mr YOUNES Rassim	Professeur	Univ. de Bejaia	Rapporteur
Mr BRADAI Mohand Amokrane	Professeur	Univ. de Bejaia	Co-Rapporteur
Mr BENABBAS Abderrahim	Professeur	Univ. de Bouira	Examinateur
Mr AKNOUCHE Hamid	Professeur	Univ. de Boumerdes	Examinateur

Année Universitaire : 2025/2026

Acknowledgements

Acknowledgements

First, I want to express my deep gratitude to God, who gave me the health, the will, and perseverance necessary to carry out this work.

My sincere thanks to Professor R. YOUNES and Professor M.A. BRADAI, respectively director and co-director of this thesis, for their supervision, their wise advice, their constructive criticism, as well as the quality of their orientations throughout this work. Their support was decisive in carrying out this research.

I also want to express my gratitude to my parents and my brothers, whose constant support, encouragement, and sacrifices were essential to my journey.

I thank the members of the jury for the honor they do me by agreeing to assess this work.

My gratitude also extends to the entire team of the Hall of Technology, the Mechanical Engineering Department, as well as to the Mechanical, Materials, and Energetic Laboratory (L2ME) of the University of Bejaia, for their support and their availability.

Finally, I warmly thank everyone who, directly or indirectly, contributed to my training and supported me throughout this route. To everyone, I say thank you.

Dedication

Dedication

I dedicate this thesis to the beings that are the dearest to me:

To my father, in testimony of recognition and gratitude, because the best reward that I can offer my parents is my success.

To my very dear mother, this noble being who sacrificed the most beautiful years of her life for my happiness and success.

To my brothers, Menad and Mohand Ou Abdellah, for their constant support.

In memory of my deceased grandparents and my uncle Ghilas Abdenour.

To all the members of my family, for their presence and affection.

To my precious friends: Bazine Sofiane, Bahouche Halima, Benabdelhak Wissam and Ouadda Dyhia.

To all my doctoral colleagues, with whom I shared this great scientific adventure.

List of Figures

List of figures

Chapter I

List of figures

Chapter II

Chapter III

List of figures

List of Tables

Chapter I

Table of Contents

Table of Contents

II Chapter II : Characterization methods and techniques

Table of Contents

Nomenclature

Nomenclature

G	Elastic constant
η	Viscosity
t_{gel}	Gelation time
A	Constant of Arhenius
E*	Apparent activation energy
h	Hydrolysis rate
Ph	Hydrogen potential: measures the acidity or basicity of a solution.
P	pressure
γ	Superficial solvent tension
θ	contact angle
a	cylinder diameter
α-Al_2O_3	The alpha phase of alumina
γ-Al_2O_3	The gamma phase of alumina
CFC	Face-centered cubic structure
θ-Al_2O_3	Theta-alumina phase
a, b, c	crystal parameters
β	Angle Beta
K -Al_2O_3	The kepa alumina phase
Kj	Kilojoule
Kg	kilogram
g	Gram
cm	centimeter
δ-Al_2O_3	The delta alumina phase
ρ	Density (g/cm^3)
M	Molecular weight (g/mol)
E	Young's modulus (GPa)
v	Poisson's ratio
σf	Flexural strength (MPa)
K1C	Toughness (Mpa.m1/2)
εr	Dielectric constant
σ	Electrical resistivity at 20°C (Ohm.cm)
Cp	Specific heat (J/K/kg)

Nomenclature

λ	Thermal conductivity (W/m/K)
α	Linear expansion (x10-6) from 20 to 1000°C
eV	Electron volte
nm	Nanometer
Å	Angstrom
ppm	parts per million: unit of measurement of concentration
GPa	Giga pascal
MPa	Mega pascal
ε	The molar extinction coefficient
log	Logarithm function
d_{hkl}	Interticular distance between crystal planes (hkl)
Al	Aluminum
O	Oxygen
Co	Cobalt
Mn	Manganese
K	Temperature in kelvin
°C	Temperature in degrees Celsius
BCC	Centered cubic structure
HCP	The hexagonal close-packed structure

General introduction

General introduction

Ceramic powders are of major industrial importance due to their excellent mechanical, optical, and thermal properties, as well as their broad range of applications. These materials are recognized as excellent thermal barriers thanks to their strong resistance to high temperatures, corrosion, wear, radiation, and oxidation. This combination of properties makes them an ideal choice for cutting tools, abrasion-resistant components, and applications in extreme environments [1–3].

The characteristics of the powder including particle size distribution, morphology, flowability, density, and phase composition are critical factors governing the performance of the raw material during thermal spraying. Optimising these interrelated parameters ensures reliable deposition and enhances both the mechanical and thermal performance of the resulting coatings [4–6].

The sol–gel route represents a particularly advantageous synthetic route for the development of advanced materials, owing to its ability to provide precise control over morphology, particle size. This process is based on the transition of a colloidal system (the “sol”) into a solid network (“gel”), thereby enabling the formation of homogeneous nanostructures. Through fine control of synthesis parameters, it becomes possible to tailor the physicochemical properties of materials such as porosity, specific surface area, crystallinity, and optical, catalytic, or mechanical properties according to the desired applications.

One of the major advantages of the sol–gel method lies in its low-temperature synthesis capability, often close to ambient conditions. This results in a significant reduction in energy consumption and production costs, while allowing the incorporation of thermally sensitive compounds or the fabrication of organic–inorganic hybrid materials. Moreover, the flexibility of the process permits the preparation of thin films, powders, fibres, and monoliths with high uniformity. Owing to these advantages, the sol–gel method stands out as a technique of choice in numerous industrial and scientific domains, notably in functional coatings, catalysis, sensors, ceramics, optics, and pharmaceuticals. Its combination of performance, versatility, and eco-efficiency makes it a particularly promising approach for the development of innovative materials [7, 8].

Alumina (Al_2O_3) is a white ceramic material and one of the most widely used due to its exceptional combination of properties and extensive industrial applications. Its refractory

nature, high stiffness, thermal and electrical insulation, corrosion and wear resistance, high hardness, low thermal expansion coefficient, and thermal stability make it a preferred material for use in mechanical, electronic, chemical, and medical sectors. Alumina exists in several polymorphic forms; among them, the α-Al_2O_3 phase is the most stable, while the γ, δ, and θ phases are metastable.

Alumina powders can be synthesised through various routes, including vapour-phase synthesis, precipitation, sol–gel processing, combustion synthesis, hydrothermal treatment, and chemical methods. Reducing the α-alumina particle size from the micrometre to the nanometre scale increases the surface area and reactivity of the powder. These improvements broaden its applications in transparent conductive coatings, biomaterials, drug delivery, environmental protection, microelectronics, and as anti-wear additives [9, 10].

Doping alumina can significantly influence its homogeneity, microstructure, optical, and mechanical properties. Doping is employed to modify or enhance specific characteristics of the powder for targeted applications [11].

Manganese-doped alumina is a ceramic material obtained by substituting aluminum ions (Al^{3+}) with manganese ions in the alumina crystal lattice. The substitution of manganese can alter both the physical and chemical properties of alumina, particularly its mechanical and magnetic behaviour. Within the alumina crystal lattice, manganese ions substitute aluminium ions, acting as substitutional impurities. The manganese concentration in the lattice can markedly affect the structural characteristics of the material. At low doping levels, the material exhibits a hexagonal close-packed (HCP) stacking, whereas at higher concentrations, it may transition to a cubic structure [12–14].

Using the sol–gel technique, it is also possible to incorporate cobalt ions into the alumina matrix, thereby significantly modifying the physicochemical properties of the resulting powder. Cobalt doping can influence several parameters, including particle size, crystallinity, specific surface area, porosity, and thermal stability. The impact of cobalt ions depends strongly on factors such as doping concentration, which plays a crucial role. At low concentrations, Co^{2+} ions can replace Al^{3+} ions within the lattice, inducing local distortions without drastically altering the overall structure. At higher levels, however, they may lead to secondary phase formation or alter phase transitions within alumina, thereby affecting the material's performance.

The sol–gel method, as a soft-chemistry approach, offers fine control over the chemical composition and dopant distribution at the nanometric scale. Parameters such as pH, ageing temperature, the nature of the cobalt precursor, and calcination conditions strongly influence the effective incorporation of cobalt and, consequently, the final properties of the powder [15–17].

The work presented in this thesis is organised into three distinct chapters, structured as follows:

- Chapter I introduces the fundamental definitions and general concepts necessary to understand the topic, covering the properties, polymorphs, industrial relevance, synthesis methods, and doping of alumina, along with a detailed description of the sol–gel route.
- Chapter II presents the synthesis protocol, including the materials, equipment, and characterisation techniques employed in this study.
- Chapter III discusses the results and analysis, encompassing thermogravimetric analysis (TGA), differential thermal analysis (DTA), Fourier-transform infrared spectroscopy (FTIR), UV–visible spectroscopy, X-ray diffraction (XRD), and microstructural morphology analysis.
- We finish this work with deep conclusion in order to sum up the main results of investigation

State of art

Numerous studies have been devoted to improving the mechanical and thermal performance of alumina-based ceramics through various synthesis routes, including sol–gel, hydrothermal, and combustion methods. However, despite significant progress, challenges remain in controlling particle morphology, homogeneity, and dopant distribution at the nanoscale. We could cite these:

Drdlikova et al. [11] found that manganese like europium and erbium segregates at grain boundaries due to its relatively low solubility in the alumina lattice. in addition, chromium, europium, erbium and manganese enhances both densification and grain growth, which is due to their multiple possible valence states.

Zvonarov et al. [12] have synthesized manganese doped alumina samples with under variation of the sintering temperature and the concentration of Mn ions. They found that at lower temperatures (100 °C), the luminescence decreases with the increase in the concentration of Mn ions, and for higher temperatures (1700 °C), the luminescence increases with the increase in Mn ions. They also found that the sensitivity of alumina ceramics doped with manganese to ionizing radiation increases with the growth of the sintering temperature under the electronic radiation of a dose of approximately 15 kGy, and this sensitivity decreases with the increase in the concentration of Mn ions.

Dhuban et al. [14] studied the manganese doping effect and sintering temperature on alumina properties, and they found that 0.1% manganese by weight was the most beneficial to improve the densification of alumina to 1500 °C, with a sample recording a relative density of 97.5% and a hardness of 14.7 GPA. In addition, alumina with 0.1% manganese by weight experienced lower grain growth and resulted in a homogeneous microstructure. On the other hand, the addition of 0.5% by weight and 1.0% by weight favored abnormal grain growth when sintered at 1500–1600 °C.

Crisan et al. [18] have prepared aluminum and silica-doped coating using the two-gel method (alkoxide and colloidal). They found that the prepared samples present catalytic activity in the ozone decomposition process, and the sol-gel method could be used for the coating of metal substrates with porous layers in porous Mn-doped alumina to make catalytic structures for the ozone decomposition process.

Navarrete et al. [19] studied the state of oxidation and the location of Mn cations in the alumina network for alumina pigments doped with manganese in the absence and presence of flows using mainly XPS, XANES, and EXAFS techniques. They found that, whatever the preparation method, the pink color of the pigments is mainly due to the species of Mn dissolved in the network of the alumina, in which they form a cluster containing 2 Mn cations. Incorporating a higher amount of Mn into the alumina network gives a more intense color due to the presence of a liquid phase which promotes the diffusion process involved in the formation of a solid solution.

Marinovi´c et al. [20] synthesized alumina doped with cobalt catalysts by the sol gel route and found that the annealing temperature affects the structural properties, the catalyst calcined at 500 °C proved to be the most effective.

Parveen et al. [21] found that alumina hybrids with glucose are amorphous and change to a semi-crystalline form upon cobalt doping.

Ramachandran et al. [22] synthesized zinc aluminate doped with cobalt nanoparticles by microwave-assisted combustion method and found that there was a change in the magnetic nature of zinc aluminate from diamagnetic behavior to superparamagnetic behavior with the increase of the Co dopant.

Taguchi et al. [23] synthesized cobalt aluminate by the coprecipitation method and found that the color of the products changed from dark green at low temperatures to blue between 800 and 1000 °C and the products prepared at temperatures above 1000 °C were bright blue. This color was attributed to the d-d transition of the Co^{+2} ion at the tetrahedral site in the spinel structure, decrease in the Co^{+2} ion at the tetrahedral site.

Bouck et al. [24] have successfully manufactured cobalt-alumina aerogels by the RSCE method. Based on the results of catalytic tests, they demonstrated that alumina-cobalt aerogels have the

ability to be used for the mitigation of automotive pollution, and they have confirmed that CoO and Co_3O_4 are more effective for catalyzing CO, and cobalt spinels have a high activity in the NOx catalyst.

Literature Review

I. Introduction

Ebelmen who noted in 1846 «the conversion of solid glass of silicic acid exposed to wet air» carried out the first Sol-Gel polymerization. Although known for more than 150 years, this sol-gel process has not met a real boom since the 1970s, from which the German firm Schott has set up an industrial process based on the chemistry of sol-gel. The applications that cover the materials developed by this process are now multiple. It offers many assets to produce materials of greater homogeneity and purity, at temperatures lower than those of conventional methods [25].

The word alumina, which comes from the Latin "alumen" characterizing the astringent stones (alum), designates the trivalent aluminum oxide. Obtaining aluminum is done from the thermal decomposition of hydrated aluminas (Hugo, 1982), which generally comes from bauxite and is composed of aluminum trihydroxides $Al(OH)_3$ (Bayerite and Gibbsite), the (oxyhydr) aluminum oxides $AlOOH.xH_2O$ (boehmite and diaspore) [26].

The aim of this chapter is, therefore, to present the general context as well as the bibliographic bases necessary for understanding the study. We will describe, in the first part, the Sol-Gel route that we used for the synthesis of gels. The second part will be devoted to aluminum Al_2O_3, its properties, and applications. The third part is reserved for alumina doping.

I.1.Sol-gel

The term sol-gel is a contraction of the terms "solution-gelation." Before the gel state is reached, the system is in the liquid state: it is made up of a mixture of colloidal oligomers and small macromolecules as well as, depending on the progress of the polymerization reaction, of different partially hydrolyzed monomers. This stable dispersion of colloidal particles within a liquid is called "sol." The size of the solid particles, denser than the liquid, must be small enough so that the forces responsible for dispersion are not overcome by gravity. The gel consists of an oxide network swollen by the solvent, with chemical bonds ensuring the mechanical cohesion of the material by giving it a rigid, non-deformable character (a gel can have an elastic character, but not macroscopic viscosity). The gel corresponds to the formation of a three-dimensional network of Van der Waals bonds. The time it takes for "sol" to turn into "gel" is called the gel time (or gel point) [27-29].

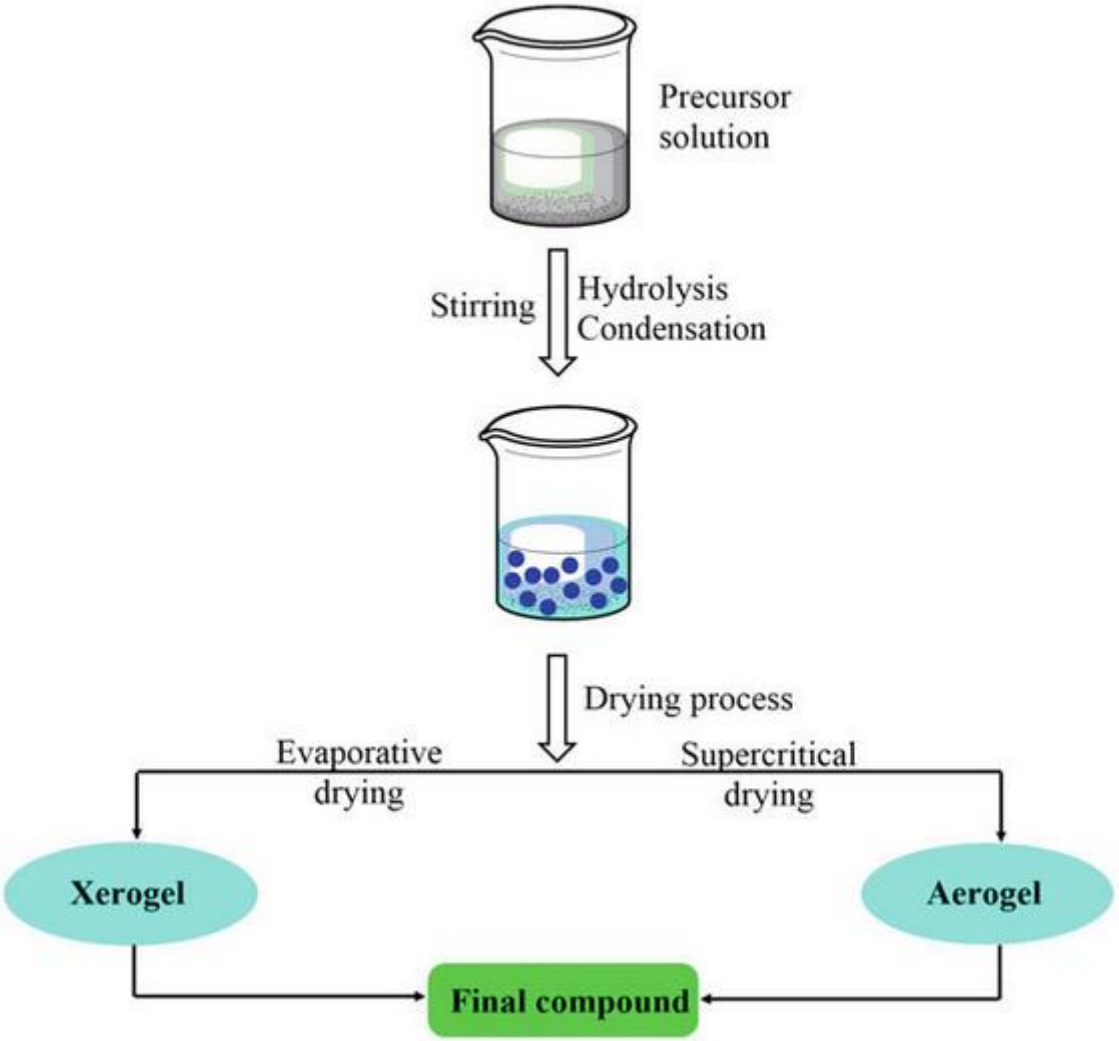

Figure I.1 Simplified schema of sol-gel processes [30].

I.1.1.The sol

It is a stable dispersion of colloidal particles suspended in a liquid (Fig.I.2). These colloidal particles are solid particles, ranging in size from 1-1000 nm. The gravitational forces on these particles are negligible. The rheological stability of this dispersion is generally ensured by the presence of a surface electric charge and is imposed by the catalytic conditions of the reaction medium (stability by electrostatic effect) [31].

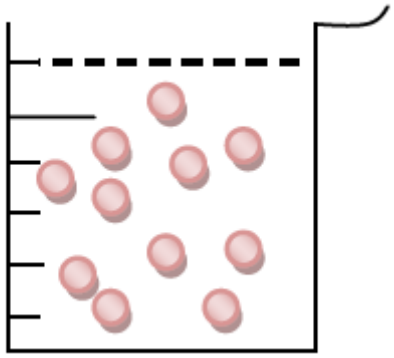

Figure.I.2 sol state

I.1.2. The gel

It is a semi-rigid, cross-linked network with pores smaller than the size of the three-dimensional molecule. The solvent and the molecules (or macromolecules) present in the medium are trapped within this network. In other words, the viscosity of the solution increases until an infinite three-dimensional network is obtained, trapping the solvent (Figure.I.3). If the liquid is water, we speak of an aquagel or hydrogel, and if it is alcohol, we speak of an alkogel [31].

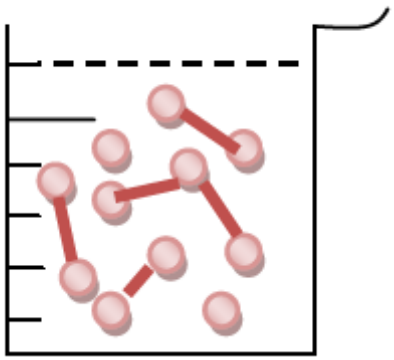

Figure I.3 Gel state

I.1.3.The precursor

The precursor is a chemical reagent used to initiate the reaction: it is often an alcoholate (alkoxide of formula $M(OR)_n$: where M is a metal, for example Zn, Al, etc., and R is an organic alkyl group C_nH_{n-1}) or a metal salt [32].

They can be very pure and have high solubility in a wide variety of organic solvents. The alcohol-based approach is the subject of most research work in the world. This great interest is due to the fact that the development of a solid from molecular precursors makes it possible to

chemically control each of the stages of the synthesis and therefore to orient them according to the targeted objective. In addition, the advantage of alkoxides is that many of them are commercially available, avoiding long synthetic procedures. Alkoxides also have some drawbacks, such as their price, which remains relatively expensive, as well as their responsiveness toward humidity, which requires working, in most cases, under a controlled atmosphere [30].

I.1.4 Sol-gel process route

I.1.4.1 Colloidal or inorganic route

Obtained from metallic salt in aqueous solution (chloride, nitrate, oxychloride, etc.). This process is cheap but difficult to control, which is why it is still rarely used. However, it is the preferred way of obtaining ceramic materials [33]. Colloidal sol-gel is based on the formation of a sol, that is to say a dispersion of dense particles (nucleation phenomenon) of nanometric size (from a few nanometres to a few tens of nanometres), which is destabilised in a controlled manner to form a three-dimensional network made up of the sol particles: the “colloidal” gel.

I.1.4.2 Polymeric or metallo-organic route

This route is made from metal alkoxides in organic solutions. It is relatively expensive, but allows granularity to be controlled fairly easily [33]. The sol-gel transition is achieved by the formation of polymer chains (growth phenomenon) which intertwine to form the three-dimensional network, thus creating a ‘polymeric’ gel [34].

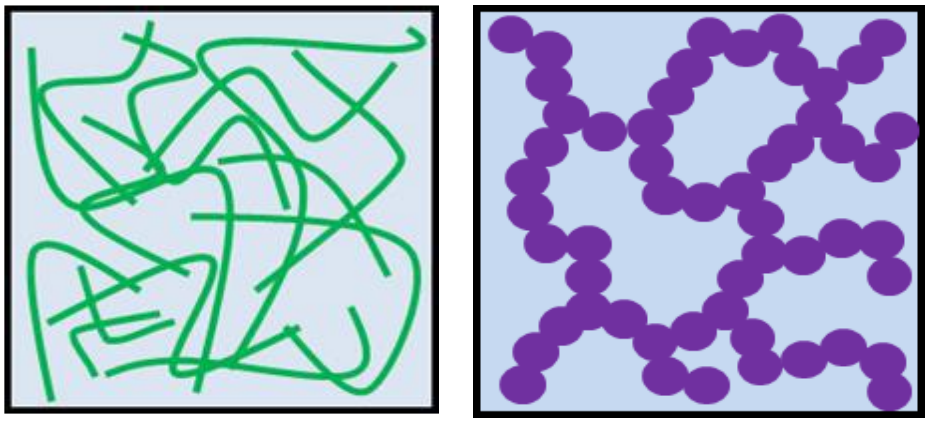

(a) (b)

Figure I.4 Polymer gel (a) Colloidal gel (b)

I.1.5 Reaction mechanism

Although the sol-gel process has been known for a century, all the complex mechanisms governing it are not yet fully understood. The chemistry of the sol-gel process is based on two reactions: hydrolysis and condensation [25].

I.1.5.1 Hydrolysis reaction

Hydrolysis is a nucleophilic substitution reaction on the M atom with transfer in the transition state of a proton towards the negatively charged - OR group, this step is followed directly by the departure of the positively charged ROH group, so it allows the transformation of the $M(OR)_z$ alkoxide groups into (M-OH) groups plus an alcohol (ROH), and therefore leads to hydroxylation of the precursor. It is defined by the following equation :

$$M(OR)_z + x\ H_2O \rightarrow M(OR)_{z-x}(OH)_x + x\ (ROH) \quad \text{Eq (I-1)}$$

It should be noted that alkoxides and water are not miscible, so the reactions take place in a common solvent, which generally corresponds to the alcohol generated during hydrolysis.
For an M atom with Z=4, the hydrolysis mechanism is as follows [31] :

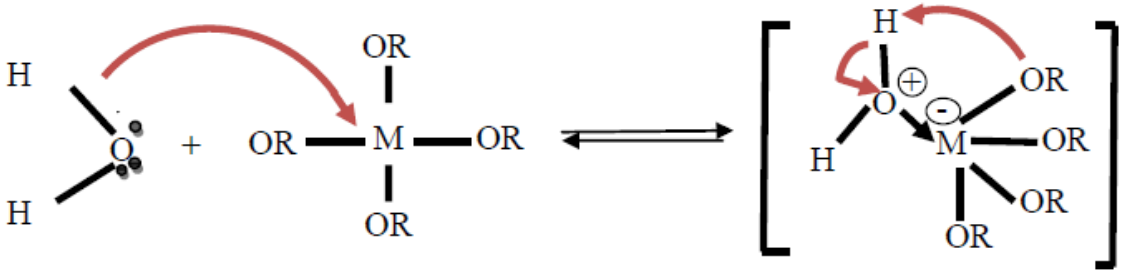

Figure I.5 Hydrolysis mechanism for metal alkoxides $M(OR)_z$

I.1.5.2 Condensation reaction

The groups (HO-M (OR) $_{n-1}$) generated during hydrolysis react either with each other to give a molecule of water (reaction 2). Or with a molecule of the alkoxide M(-OR) to give a molecule of alcohol (reaction 1), leading to the creation of M-O-M bridges where each oxygen atom becomes a bridge linking two atoms of the metal M This corresponds to the formation of a gel whose viscosity increases over time; this gel contains solvents and precursors that have not yet reacted [33].

This process is governed by the following reactions at room temperature:

$(OR)_{n-1} – M–OH+HO–M– (OR)_{n-1} \rightarrow (OR)_{n-1}–M–O–M– (OR)_{n-1}+R–OH$ ……..…Eq (I-2)

$(OR)_{n-1} – M–OH+HO–M– (OR)_{n-1} \rightarrow (OR)_{n-1}–M–O–M– (OR)_{n-1}+H_2O$ ….....Eq (I-3)

I.1.5.3 Gelation

The above reaction leads to the gelation of a gel composed of M-OM (or M-OH-M) chains whose viscosity increases with time. The gel still contains a solvent and unreacted precursors. After gelation, the material dries due to capillary forces in the pores, and this drying causes the volume to shrink when the alcohol or water evaporates [33].

I.1.5.4 Drying

From the same solution and depending on how the gel is dried, there are several types of drying that enable you to obtain different types of material:

- Xerogel: conventional drying (normal evaporation) results in a reduction in volume; from 5 to 10%. In this mode, the residual liquid pushes a very strong capillary force, resulting in a reduction in macroporosity and finally a dry gel structure.
- Aerogel: drying under supercritical conditions (in a high-pressure autoclave) results in little or no volume shrinkage. The gel gives a very open "aerogel" structure with good macroporosity [33].

I.1.6 Main stages of the Sol-Gel transition

The changes in mechanical properties during the Sol-Gel transition are spectacular. The structure of the frost at this moment of transformation (gel) is very different from that of the final network. It is described on a nanometric scale and is defined as having a fractal geometry. For a good interpretation of the phenomena linked to the Sol-Gel transition, the diagram chosen for gelification is generally that of growing polymer chains which are agglomerated by condensation to form clusters. During the advancement of hydrocondensation reactions, polymeric clusters are generated, the size of which increases over time. When one of these clusters reaches the infinite dimension, practically the dimension of the reaction container, the viscosity becomes similarly infinite: this is the sol-Gel transition point. From this moment, the infinite heap called "gel fraction" continues to grow by incorporating smaller polymeric groups. When all the links have been used, the gel is formed. From a macroscopic point of view, the transition can be followed by the mechanical behavior of the solution (its viscosity and its

elasticity). If we follow the evolution of these viscoelastic properties of the solution as a function of time, we then notice a divergence of the viscosity of the solution and an increase in the elastic constant (G) (or Coulomb modulus) in the frost phase. The evolution of the viscosity of a soil and that of its Coulomb modulus as a function of time is presented schematically in Figure I.6 [30].

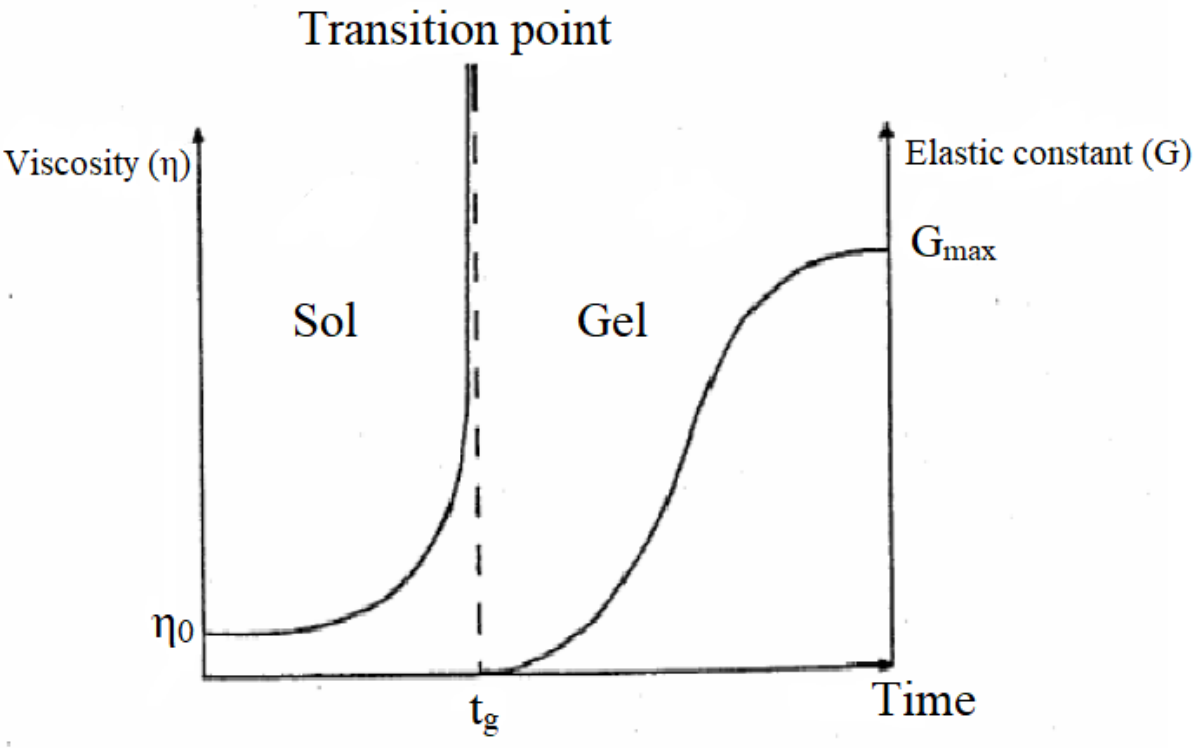

Figure I.6 Evolution of the viscosity of the solution and the elastic constant of the gel; tg corresponds to the time at the end of which the sol-gel transition is reached.

I.7 Physico-chemical parameters and their influence on structure

The structure of the condensed species depends on the relative reaction kinetics of each precursor in solution. The reactivities of the different precursors can be governed by several physico-chemical parameters presented below [25]:

- **Metal atom effect:** The electronic nature of metals largely influences the speed of the sol-gel process. A nucleophilic attack is all the more favored as the metal center is electrophilic. Transitional metals have low electronegativity compared to silicon; as a result, their alkoxides react violently with water [35].

- **Temperature:** Hydrolysis and condensation rates increase with temperature as soon as the sol is prepared [36].

  The Arrhenius law can evaluate the influence of temperature on the sol-gel process [35]:

  $(1/t_{gel}) = A\ e^{-E^*/RT}$ …….. Eq (I-4)

t_{gel}: Gelation time

A: Constant of Arhenius

E*: Apparent activation energy.

- **The nature of the solvents**: Solvents make it possible to obtain a homogeneous solution of controlled viscosity [36].

  In general, alkoxides are not (or are only slightly) miscible in water. It is therefore necessary to mix these precursors, water, and possibly the catalyst in a common solvent. It is then preferable to use as a solvent the alcohol corresponding to the ligand –OR of the alkoxide; this is in order to avoid possible reactions between the different components likely to modify the reaction kinetics. The starting ground is therefore generally an alcoholic solution. It is sometimes indicated to use a co-solvent to better control hydrolysis and condensation reactions. The choice of solvent is also dictated by imperatives of the process: ease of drying, integrity of the final material, and possibly, non-toxicity 30.

- **The rate of hydrolysis**: This is the ratio of the number of moles of water added to the number of moles of metal M. Its influence on the relative kinetics of hydrolysis and condensation is fairly complex, as the water added is not generally totally consumed, and because the residual water molecules, regenerated during condensation or formed by esterification, must also be taken into account. A large number of -OH groups bonded to the metal can block polymerisation and cause precipitation [25, 36]. With the increase in temperature, hydrolysis and condensation are accelerated.

  We define the hydrolysis rate (h) as:

  $h = [H_2O]/[Ti\ (OR)_n]$……..…… Eq (I-5)

  This report will regulate the hydrolysis reaction kinetics. You have to choose it according to the alkoxide and its affinity for water, which can be determined by the

model of partial loads. Depending on the relative speeds of hydrolysis and condensation, the products obtained can take different forms.

There are three (03) domains for the hydrolysis rate:

- h <1: In this area, gelification can never appear as long as hydrolysis is perfectly controlled, which means that there is no excess water locally.

- 1 <h <4: In such conditions, a polymer channel can be obtained.

- h> 4: polymers, gels and precipitates can be obtained when excess water is added to the alkoxide.

Depending on the relative speeds of hydrolysis and condensation, the products obtained can take different forms 30.

Table I. Products obtained according to the relative speeds of hydrolysis and condensation.

Hydrolysis speed	Condensation speed	Products obtained
Slow	Slow	Colloids/sol
Rapid	Slow	Polymeric gels
Rapid	Rapid	Colloidal gels or gelatinous precipitates
Slow	Rapid	Controlled precipitation

- **The use of catalysts**: An acidic Ph speeds up the hydrolysis reaction and slows down condensation, unlike a basic Ph. A high rate of hydrolysis (acidic Ph) therefore favours the growth of the network and leads to a polymeric solution. Under acid catalysis, which is the fastest synthesis route, the gel formed is called a 'polymeric gel': an open structure is obtained after gelation. A low rate of hydrolysis (basic Ph) favours nucleation and leads to the formation of a colloidal solution. In the case of basic catalysis, the size of the pores is controllable (unlike acid catalysis). The gel formed is called a 'colloidal gel' and has a large pore structure [25].

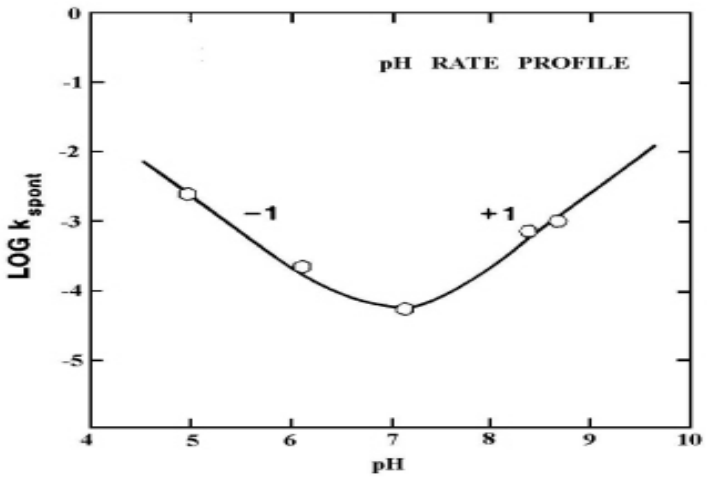

Figure I.7 Influence of Ph on hydrolysis [37].

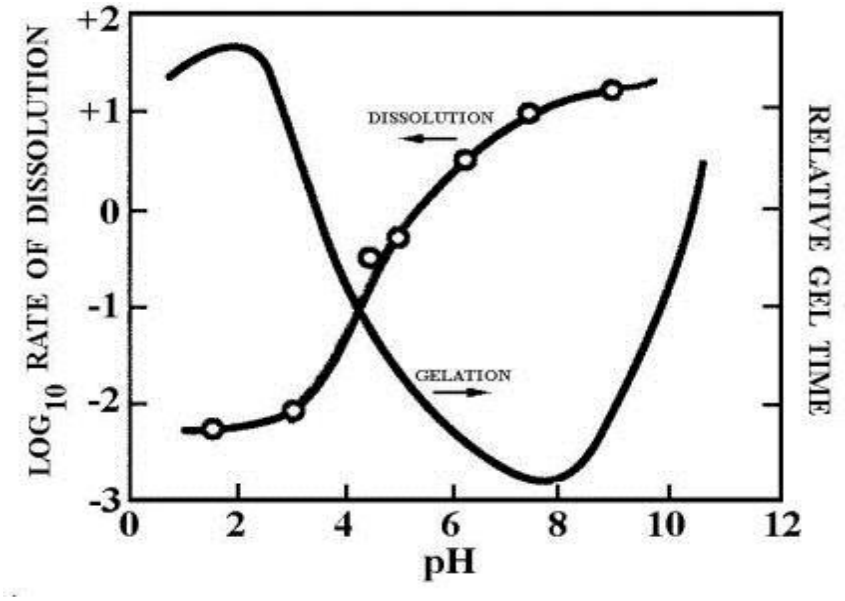

Figure I.8 Influence of Ph on gelation speed [37].

- **Drying effect:** The big problem for obtaining monolithic materials arises at the drying stage. The frost contracts until cracking and fracture, thus causing the loss of mechanical properties. This problem is due to the capillary effects exerted by the solvent on the walls of the frost canals.

  If these channels are assimilated to cylinders, then the following relation gives the pressure exerted by the solvent on the pores:

  $P = (2 \gamma \cos \theta) / a$ …… Eq (I-6)

P: pressure exerted on the walls

γ: Superficial solvent tension

θ: contact angle

a: cylinder diameter

A controlled evaporation of the solvent makes it possible to minimize these effects. This is why the frost goes through an aging stage, which decreases the evaporation speed and therefore reduces the fracture of the gels [35].

- **Calcination temperature effect**

  The frost obtained still contains a significant quantity of organic residues (solvent, ligands of precursors, alcohols). A heat treatment is necessary to eliminate these residues in order to stabilize the material. This heat treatment must be performed at a sufficiently high temperature to ensure perfect and total elimination of the residues [35].

I.1.8 Applications of the Sol Gel technique

Materials from Sol-Gel technology are found in four main industrial activities, namely [35]:

- Chemical applications that take up the synthesis of powders, catalysts, and membranes.
- Optical applications that include ophthalmic coverings and optical fiber syntheses.
- Biochemical applications, which include the formulation of drugs, the development of new treatments, cosmetic formulations, artificial bone tissues, and dentistry.
- Structure applications for manufacturing glasses, ceramics, insulation, refractory, or composite materials, fibers, abrasives, and coatings.

I.1.9 The advantages of the sol-gel method

- Sol gel formation is a relatively low-temperature process.
- Consumes less energy and therefore less pollution.
- Low-temperature sintering possible.
- Allows fine control of the chemical composition of the product.
- Can create very fine, high-purity powders [38].

I.1.10 Disadvantages of the sol-gel method

- High cost of raw materials (in the case of metal alkoxides).
- Often there is a large amount of shrinkage and cracking during drying.
- Very substrate dependent in the case of thin film synthesis.
- As several stages are involved, close monitoring of the process is necessary [38].

I.2 Alumina

Alumina is one of the most widely used technical ceramics. It can exist in various crystallographic phases. However, the only phase that is stable at the temperatures required for sintering is corundum, also known as α-alumina. Consequently, all dense aluminas are generally in the form of corundum. The other phases exist more particularly in the form of particles, highly porous materials or as intermediate phases in a chain of phase transformations leading to the formation of α-alumina [39].

I.2.1 Crystallographic structures of alumina

I.2.1.1 α-Alumina

α-Alumina, the most stable, crystallises in the trigonal system of symmetry D_{3D}^{6} - R-3c. The elementary lattice contains thirty atoms, corresponding to six Al_2O_3 units. The oxygen atoms are organised in an hcp stacking in which the aluminium atoms occupy two-thirds of the AlO_6 octahedral sites, as can be seen in Figures I.9. The primitive mesh is drawn in a rhombohedral system of axes with, at each node, a pattern containing two Al_2O_3 alumina molecules arranged in two triangular diamonds along the c axis of the corresponding hexagonal coordinate system [40].

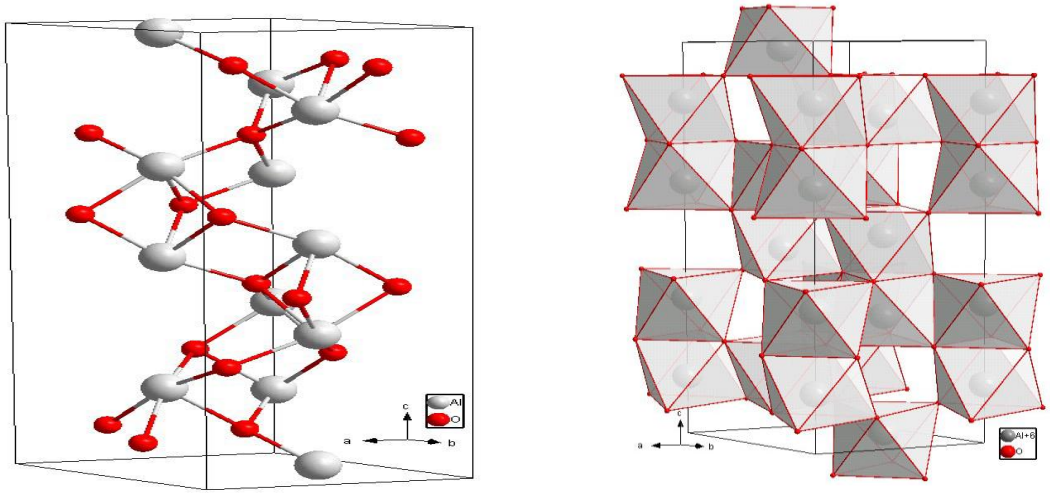

(a) (b)

Figure I.9 Elementary lattice of α-alumina (a) Stack of AlO_6 octahedra in α-alumina

I.2.1.2 γ -Alumina

Despite many years of study, the "phase" has not been completely determined and several models have been proposed in the literature. X-ray diffractograms show that the ɤ phase must be close to the AB_2O_4 cubic spinel structure with aluminium vacancies in order to obtain the stoichiometry of alumina. However, it appears that one of the points of discussion of this structure concerns the fact that some aluminium atoms occupy crystallographic sites that do not belong to the cubic spinel symmetry.

The oxygen atoms are arranged in a CFC structure, which, by symmetry, is reduced to eight oxygens, six of which have a coordination of four and two of which have a coordination of three with their aluminium neighbours. The positions of the aluminium atoms are found by symmetry thanks to six independent positions and occupy two octahedral sites for one tetrahedral site.

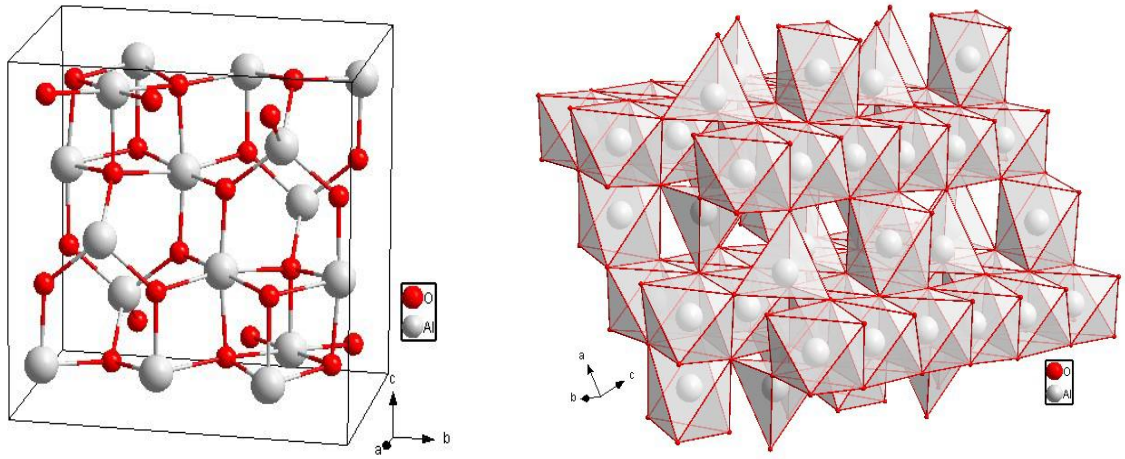

(a) (b)

Figure I.10 Elementary lattice of ɤ alumina (a) Stacking of AlO_6 octahedra and AlO_4 tetrahedra in γ alumina (b)

As shown in Figure I.10, the structure can be seen as a superposition of two types of planes. One plane is made up of octahedrons sharing edges and some unoccupied sites. A second plane made up of: tetrahedra which are placed at the aplomb of the non-occupied sites and share only their vertices with the other polyhedra, and octahedra sharing only their edges with their counterparts in the other planes [41].

I.2.1.3 θ-Alumina

The θ phase crystallises in the monoclinic system of C_{2h}-C12/m1 symmetry and is based on four crystal parameters a, b, c and β: a = 11.85 Å, b = 2.904 Å, c = 5.622 Å and β = 103.8°. The lattice contains 20 atoms arranged so that the oxygen atoms arrange themselves in a CFC structure built by symmetry from three independent positions, two of which have a coordinacy of four and the last of three. Aluminium atoms occupy as many octahedral sites as tetrahedral sites and are reduced to two independent positions [41].

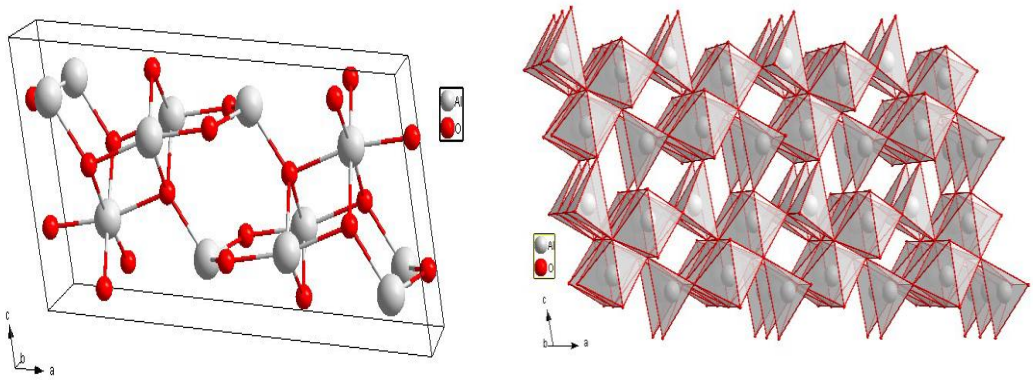

(a) (b)

Figure I.11 Elementary lattice of θ alumina (a) Stacking of AlO_6 octahedra and AlO_4 tetrahedra in θ alumina (b).

I.2.1.4 K-alumina

K-alumina crystallises in the orthorhombic system with C2h - Pna21 symmetry. The lattice parameters are a = 4.8437 Å, b = 8.33 Å and c = 8.9547 Å.

The elemental lattice contains 8 units, with the oxygen atoms forming a double hcp structure ABACABAC, from which the twenty-four oxygens of the lattice can be deduced from six atomic positions, three positions having a co-ordination of four and the other three a co-ordination of three. In this structure, shown in Figure I.12, the aluminium atoms occupy three octahedral sites for one tetrahedral site [41].

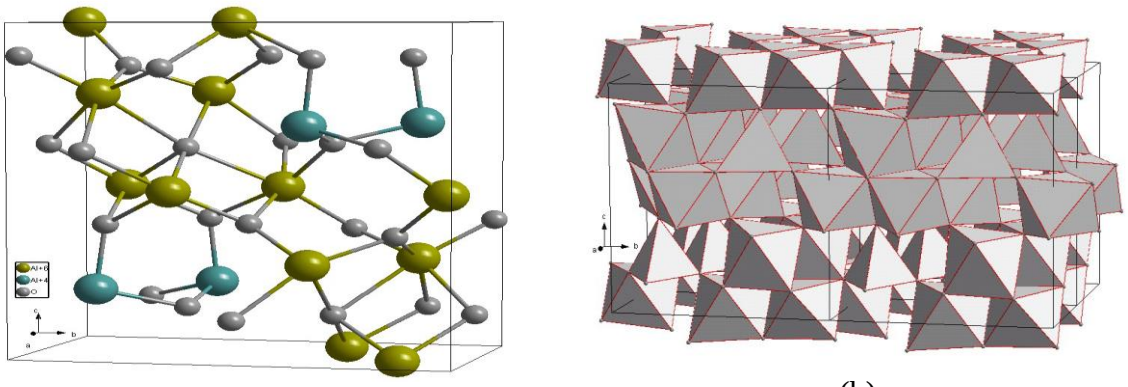

(a) (b)

Figure I.12 Elementary lattice of K(a) alumina Stacking of AlO_6 octahedra and AlO_4 tetrahedra in K(b) alumina

I.2.2 Aluminium hydroxides

Crystalline aluminium hydroxides are composed of six types of alumina hydrate:

Gibbsite (and/or hydrargillite, the name used in Europe and gibbsite generally in the rest of the world), bayerite, nordstrandite and, more recently, doyleite, discovered in 1985. Classified as four aluminium trihydroxides with a stoichiometric composition: $Al(OH)_3 = Al_2O_3\text{-}3H_2O$, and boehmite and diaspore, classified as two aluminium oxyhydroxides with stoichiometric compositions: $AlO(OH) = Al_2O_3\text{-}H_2O$ [41].

The most widely studied $Al(OH)_3$ phases are :

I.2.2.1 Gibbsite

This is the most common and thermodynamically stable hydroxide phase in natural systems (the major component in bauxite ores). Structurally, it contains OH- ions in consequent and opposite layers with a sequence arranged as (AB-BA-AB-BA...) in the direction perpendicular to the layers, which means that the OH- ions of adjacent groups are located directly opposite each other (Figure I.13) [41].

I.2.2.2 Bayerite

Crystallises under very basic conditions during bauxite processing (Bayer process). Its layers follow the sequence (AB-AB-AB-AB...), the OH- ions in one layer are offset from the previous layer, so that the ions in one layer fall into the spaces between the hydroxyls in neighbouring layers (Figure I.13) [41].

I.2.2.3 Nordstrandite

This crystallises as the precipitates age under slightly basic conditions (PH~7.5 - 9). Its structure follows the model of the bayerite layer, but with hydroxyl groups located in opposite directions, giving the sequence (AB-BA-BA-AB...) (figure I.13) [41].

I.2.2.4 Doyleite

It has a stack of layers similar to that of bayerite (figure I.13), but the hydroxyls of the two resulting double layers are located in positions intermediate between those of gibbsite and nordstrandite [41].

I.2.2.5 Boehmite

Precipitates during the neutralisation of aluminate solutions at high temperature, in which 2 AlOOH-based chains are arranged in a cubic stack (figure I.13) [41].

I.2.2.6 The diaspore

In the diaspore, the 2 AlOOH-based chains are arranged in a hexagonal stack (figure I.13). This phase is generally found to be the product of weathering or high-temperature transformations. The dehydration reaction of alumina trihydrate ($Al(OH)_3$) is highly endothermic, with a specific enthalpy of 1155 kJ - kg-1. The trihydrate loses ~34.6% of its mass by weight between 200 and 1200°C. The greatest weight loss occurs between 250 and 400°C, and the fastest rate of dehydration occurs around 350°C. The thermal decomposition of alumina hydrates during firing leads, depending on the intensity of firing, to the formation of four types of alumina: calcined alumina, tabular alumina, fused alumina and transition alumina [41].

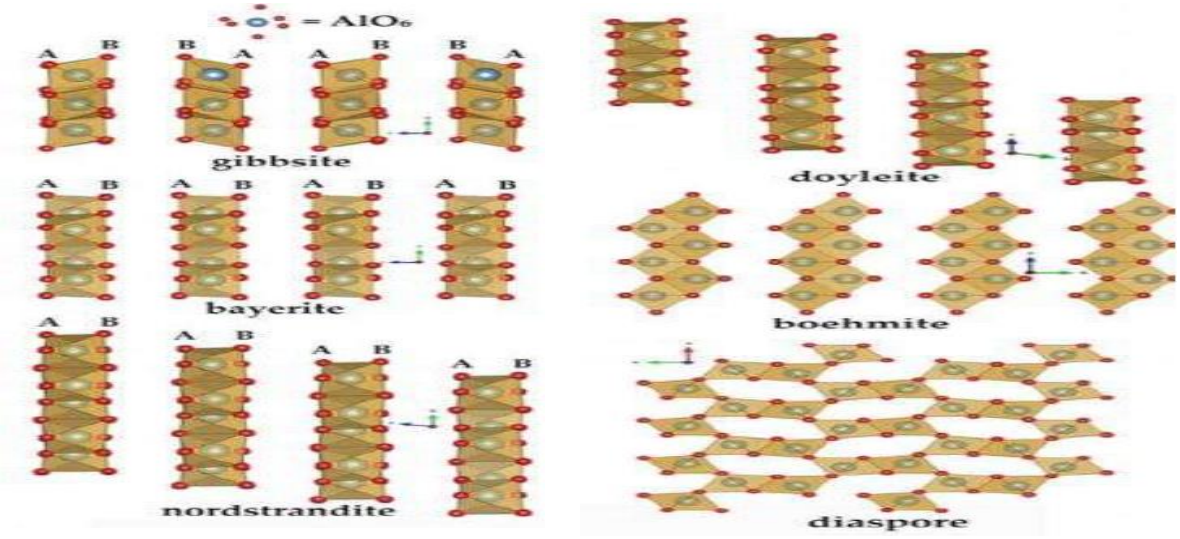

Figure I.13 Structures of aluminium trihydroxide and oxyhydroxide phases in octahedral representations.

Table I.2 Alumina hydrates (aluminium hydroxides and oxyhydroxides).

Phases	Chemical formula	Crystalline system	Density (g/cm^{-3})
Gibbsite (hydrargilite)	α-$Al(OH)_3$	Monoclinic	2,42
Bayerite	β-$Al(OH)_3$	Monoclinic	2,53
Nordstrandite	ɣ-$Al(OH)_3$	Triclinic	2,45
Doyleite	ɣ-$Al(OH)_3$	Triclinic	2,48
Boehmite	ɣ-AlO(OH)	Orthorhombic	3,01
Diaspore	α-AlO(OH)	Orthorhombic	3,44

I.2.3 Transformation of metastable aluminas

The transformation of transition aluminas is a subject of research that has already given rise to a large body of literature. Under the action of heat, γ-Al_2O_3 undergoes a series of polymorphic transformations. The sequence of phase transformations can vary depending on the method used to produce the polymorph and the presence of impurities and dopants.

The temperature ranges given for the stability of the crystalline phase are approximate and depend on several factors: degree of crystallinity, presence of impurities in the starting material, and the heat treatment applied.

Gibbsite → 280°C → χ → 800°C → κ → 1000°C→ α-Al_2O_3 ……... Eq(I-7)
Bayerite→280°→ η→830°C→θ→1000°C→ α-Al_2O_3 ……. Eq (I-8)
Boehmite→450°C → γ → 800°C → δ→ 920°C → θ →1050°C → α-Al_2O_3 ……. Eq (I-9)
Diaspore→ 500°C→ α-Al_2O_3 ……. Eq (I-10)

The equations show the transition alumina filiations as a function of the starting hydroxide and temperature. The transition temperatures are given for information only and may vary with the operating conditions.

The crystal structures of the compounds are similar, with the anions arranged in a face-centred cubic system. It is the location of the cations between the octahedral and tetrahedral sites that varies by changing the c/a parameter. There are simple relationships between the crystallographic axes of the structures.

The transformation sequence of polymorphic phases (Eq. I11):

$\gamma\text{-}Al_2O_3 \rightarrow \delta\text{-}Al_2O_3 \rightarrow \theta\text{-}Al_2O_3$ …….. Eq (I-11)

The evolution from $\gamma\text{-}Al_2O_3$ to $\delta\text{-}Al_2O_3$ is explained by the migration of cations from tetrahedral to octahedral sites. The transition from one structure to the other can take place without any significant disruption of the structure and requires considerable energy.

Transformations:

$\gamma\text{-}Al_2O_3 \rightarrow \delta\text{-}Al_2O_3$ …… Eq (I-12)

And of

$\delta\text{-}Al_2O_3 \rightarrow \theta\text{-}Al_2O_3$ ……. Eq (I-13)

Are then displacive with a relatively low activation energy. In this case, the transformation can take place at low temperature. The transformation of different polymorphic forms then represents a so-called topotactic deformation of the network.

Phase transformation:

$\theta\text{-}Al_2O_3 \rightarrow \alpha\text{-}Al_2O_3$ …….. Eq (I-14)

Is different from those carried out on transition aluminas. This transformation occurs by changing the positions of the oxygen anions da the CFC structure to a compact hexagonal structure. The $\theta \rightarrow \alpha$ transformation is then reconstructive.

The inter-reticular distances of some crystallographic planes in the aluminas ($\gamma\text{-}Al_2O_3$, $\delta\text{-}Al_2O_3$, $\theta\text{-}Al_2O_3$ and $\alpha\text{-}Al_2O_3$) are similar. Because of this close similarity between the lattice distances of the different polymorphs, phase indentification during the transformation of a polycrystalline can be equivocal. Furthermore, most of these polymorphs coexist during the transformation.

The transformation of $\theta\text{-}Al_2O_3 \rightarrow \alpha\text{-}Al_2O_3$ is systematically accompanied by the transformation of a vermicular microstructure characterised by the presence of large porosities. A drastic

change in crystallite size, density, pore size and porosity distribution after this transformation has been observed. This makes this step critical in controlling microstructural evolution [42].

I.2.4 Specific characteristics of alumina

I.2.4.1 General properties of alumina

Table I.3 Some properties of alumina: mechanical, physical, thermal, electrical and resistances.

Properties	Values	Symbols
Physical properties		
- Density (g/cm^3)	3,9	ρ
- Molecular weight (g/mol)	102	M
-Maximum operating temperature in air (°C)	1700-1800	-
Mechanical properties		
- Hardness (Mohs)	9	
- Young's modulus (GPa)	300-400	E
- Poisson's ratio	0,25	v
- Flexural strength (MPa)	380	σf
- Toughness (Mpa.m1/2)	2-3	K1C
Electrical properties		
-Dielectric constant	9-10	εr
-Electrical resistivity at 20°C (Ohm.cm)	> 1014	σ
-Dielectric strength (kV/mm)	10-20	
Thermal properties		
- Specific heat (J/K/kg)	900	Cp
-Thermal conductivity (W/m/K)		
- at 20°C	26-35	λ
- at 500°C	10-15	
- Linear expansion (x10-6) from 20 to 1000°C	8-9	α
- Melting point (°C)	2050	

Chemical resistance	Good	
- Acids - concentrated	Good	
- Acids - diluted	Good	
- Alkalis	Good	
- Halogens- Métaux	Good	

Its good mechanical strength at high temperatures, high hardness, excellent wear resistance, high electrical resistivity and high chemical inertia make alumina a material used in a wide variety of fields. Table I.1 shows its main mechanical, physical, thermal, electrical and chemical resistance properties [42].

I.2.5 Industrial applications

Alumina is a very hard compound, with only diamond and a few synthetic products being harder. At room temperature, it is unaffected by common chemical compounds. It melts at over 2000°C. Very pure alumina can be used up to 1700°C. It is gas-tight up to 1300°C. The combination of a high thermal coefficient, low thermal expansion and high compressive strength means it withstands thermal shock well.

It is therefore used as a refractory material, for example for lining furnaces or as crucibles, tubes and thermocouple sheaths subjected to thermal shocks.

Alumina also offers good electrical insulation at high temperatures and good wear resistance, making it suitable for use as a tooling material [42].

I.2.6 Defects in alumina

Point defects and surface defects are the most common defects affecting the physical properties of alumina. Intrinsic point defects are oxygen vacancies, aluminium vacancies and aluminium ions in interstitial positions. As in ionic solids, a distinction is made between Schottky defects and Frenkel defects in alumina. Schottky defects correspond to the simultaneous presence of aluminium and oxygen vacancies, and for electroneutrality to be verified, three oxygen vacancies are created for every two aluminium vacancies. Frenkel defects correspond to the simultaneous presence of an aluminium vacancy and an aluminium ion in an interstitial position.

Extrinsic point defects are impurities. A large number of foreign species are present in alumina. In order to control or improve the physical properties of ceramics, impurities such as Zr^{+4}. Mn^{+3} or Mn^{+2} and Ti^{+3} or Ti^{+4} are sometimes introduced in the form of ZrO_2. MnO_2, and TiO_2 oxide into the material voluntarily (doping). These elements replace the Al^{+3} cations in the lattice.

Surface defects are essentially made up of the many interfaces that the material contains. They are mainly located at grain boundaries, between intergranular phases (glass, spinel $MgAl_2O_4$. anorthite $CaAl_2Si_2Og$....) and alumina grains.

These various defects are manifested by the appearance of localised states in the band gap that can act as traps for charge carriers (holes, electrons). Depending on their energies, a distinction is made between shallow traps < 0.1 eV, which correspond to extended defects (grain boundaries), and deep traps of the order of 4 eV, which correspond to vacancies [43].

I.2.7 Areas of application

In view of its various extremely important properties, alumina has been used extensively in a wide variety of applications (see, for example, Figure I.14):

- Gas corrosion-resistant electrical insulators and laser components used in semiconductor processing equipment (Chuck, loading and unloading arm and sealing ring).
- Electron tubes, mass spectrometers.
- Insulating substrate for laser diodes.
- Mirror / diffusion cavity for semiconductor laser (YAG) and light therapy (pulsed light).
- Structural parts of high-vacuum and/or cryogenic equipment for high-temperature nuclear radiation devices.
- Wear-resistant parts for pistons.
- Abrasive particles, cutting tools, bearings.
- Bioceramics [44]

Abrasives Sanitary ceramics Bioceramics

Figure I.14 Applications for alumina.

I.2.8 Alumina coatings

Aluminium oxide coatings are used in many industrial fields, with different applications depending on the allotropic form. Amorphous films are mainly used for protection against chemical corrosion or electrical insulation. The κ and α phases are used in microelectronics, as hard coatings against wear, but also as an oxidation barrier on gas turbines. Because of its large specific surface area, the γ phase is widely used for catalytic applications, either as a catalyst or as a catalyst support. The various applications of alumina thin films concern the following fields:

- Chemical: used as an anti-diffusion barrier to protect the substrate against a hostile or corrosive environment;
- Mechanical: protection against wear and erosion by solid particles;
- Thermal: thermal protection layer;
- Corrosion and oxidation: protection of steel against high-temperature corrosion;
- Electronics: passivation layer, gate oxide, masking in photolithography;
- Optics: production of optical waveguides in the visible and infrared and
- Protection of solar collectors;
- Biomaterial: biocompatible films for orthopaedic applications.

A number of techniques can be used to produce coatings of varying thicknesses (from a single layer to several micrometres) of alumina. Alumina deposits can be made by:

- réaction électrochimique : anodisation de l'aluminium ;
- sol-gel : spincoating et dip-coating ;
- FSP (flame spray pyrolysis) ; LFS-liquid flame spraying ;
- projection thermique ;

- CVD (chemical vapour deposition) ;
- FACVD (flame-assisted chemical vapour deposition) ;
- PACVD (plasma assisted chemical vapour deposition) ;
- PVD (physical vapour deposition) ;
- IMS (ionized magneton sputtering) ;
- IBAD (ion beam assisted deposition), sur un substrat métallique, céramique ou polymère [45].

I.2.9 Synthesis process

I.2.9.1 Bayer process

There are many ways of obtaining alumina. The extraction of alumina from bauxite is based on a chemical method known as the BAYER process, invented by the Austrian Karl Joseph BAYER (Figure I.15). Bauxite essentially contains 30% to 60% alumina with oxides of iron, silicon, titanium and calcium. The process used includes separation and purification. Alumina is present in bauxite in the form of hydrates such as gibbsite (trihydrate, Al_2O_3-$(H_2O)_3$) or boehmite monohydrate (Al_2O_3-(H_2O)). Bauxite and soda ash (NaOH) dissolve in gaseous water under pressure and at high temperature (125 to 275°C). Soda is a strong base that supplies hydroxide ions. When hot, the soda dissolves the alumina, while the impurities (iron oxide, silica, various oxides) remain insoluble. The mixture of these solid impurities is colloquially known as red mud.

$NaOH \rightarrow Na^+ + OH^-$ ……(I-15)

$Al_2O_3 \cdot (H_2O) + 2OH^- \rightarrow 2\ AlO_2^- + 2\ H_2O$ ……..(I-16)

$Al_2O_3 \cdot (H_2O)_3 + 2\ OH^- \rightarrow 2\ AlO_2^- + 4\ H_2O$ ……(I-17)

$Al_2O_3 + 2\ NaOH + 3\ H_2O \rightarrow 2\ NaAl(OH)_4$ ……... (I-18)

The hydroxyl bath is then cooled, allowing the aluminium trihydroxide $Al(OH)_3$ to precipitate as a white solid, a phase known as precipitation.

$Al(OH)_3 + OH^- \rightarrow [Al(OH)_4]^-$ ……(I-19)

The filtrate is then washed and filtered to remove as much sodium as possible. After calcining the filtrate at 1050°C, the trihydroxide is converted to anhydrous alumina Al_2O_3 [44].

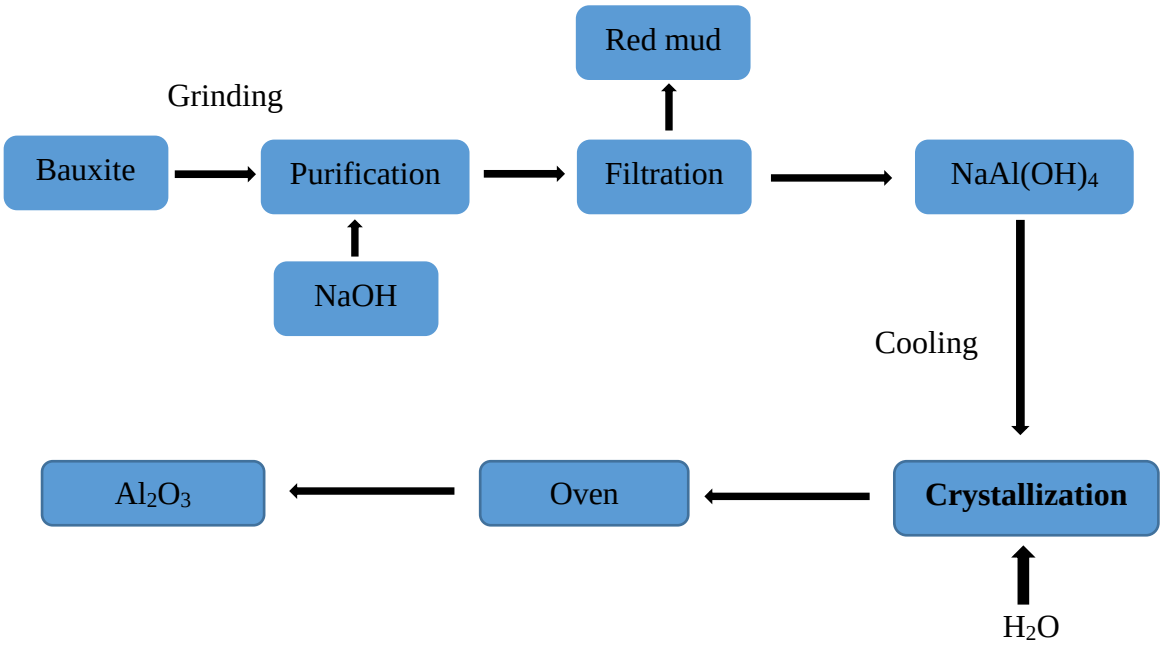

Figure I.15 Principle of the Bayer process

I.2.9.2 Ex-Alun extraction process

In order to increase the purity of the alumina synthesised, another method called Ex-Alun has been developed by BAIKOWSKI SAS. A mixture (called alum) is obtained by dissolving/crystallising two raw materials: ammonium sulphate $(NH_4)_2SO_4$ and aluminium sulphate $Al_2(SO_4)_3$ (Figure I.16). Impurities are removed by washing the crystals. The alum is then calcined at around 1000 to 1200°C to obtain γ-alumina. The latter can undergo a 2nd calcination at 1400°C to obtain α-alumina. This method is best for obtaining alumina with good chemical purity [44].

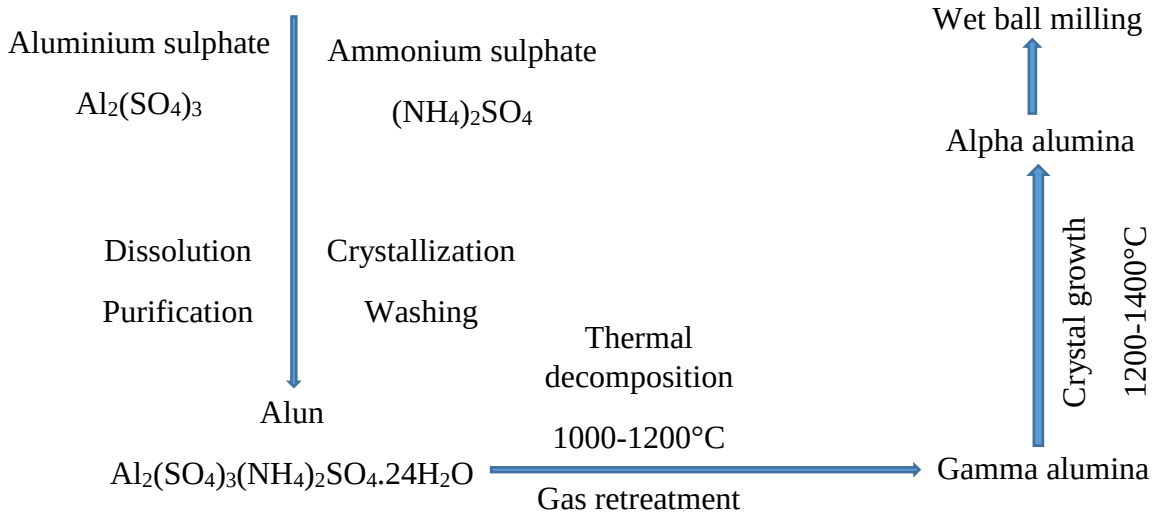

Figure I.16 Principle of the Ex-Alun extraction process.

I.3 Doping of alumina α

Dopants are sometimes used to obtain transparent ceramics, to promote densification or to inhibit grain growth, leading to materials with very different microstructures and therefore different properties [46, 47].

I.3.1 The main principles of doping

I.3.1.1 Implementation of doping

Doping of α-alumina can be carried out in various ways. The main methods are dry doping (mixing Al_2O_3 oxide and MxOy doping metal oxide powders) and wet doping methods. The latter are generally preferred as they allow a more homogeneous distribution of the dopant within the alumina matrix. In this case, the starting alumina powder is dispersed in an alcoholic ethanol, isopropanol or aqueous solution into which the doping elements are added in the form of nitrate or acetate salts or directly in the form of oxides. This solution is then mixed with a jar-turner to homogenise the distribution of the dopant. However, some studies have shown the limitations of this doping method, which could lead to slight agglomeration within the matrix as well as pollution from the beads introduced into the suspension before the jar-turner stage. This is why new wet doping methods are currently being developed. One example is the infiltration method, which involves manufacturing a porous alumina preform that is then immersed in a solution containing doping salts. The dopant is then infiltrated and precipitated in situ. A second method would be precipitation. The dopant salts are introduced into a suspension containing alumina particles. Ammonia is added to achieve the pH required for precipitation of the dopant ions in the alumina matrix. These two methods have been shown to have a beneficial effect on the homogeneity of the dopant distribution within the alumina matrix compared with the traditional powder mixing method using a jar-turner [46].

I.3.1.2 Location of dopants

Dopants can form a solid solution in the grain or at grain boundaries or form a precipitate.

- Dopants in solid solution in the grain by volume.

Atoms foreign to the matrix enter the crystal lattice during sintering. They can occupy two types of sites: normal sites in substitution of aluminium and interstitial sites. These point defects in the volume of the grain will influence the volume diffusion coefficients.

- Dopants segregated at grain boundaries when volume solubility is reached

The dopant segregated at the grain boundaries is in solid solution. Defects are created and lead to changes in the diffusion coefficients at the grain boundaries.

- Dopants in precipitate form

When the grain and grain boundaries can no longer accept foreign atoms, a second phase can form at the grain boundaries or triple points of the ceramic. The presence of these precipitates then modifies the sintering mechanism. The second phase can inhibit grain boundary migration and limit grain growth. The precipitates can also form a liquid phase. In this case, the speed of diffusion is increased and short circuits are created between the diffusion paths [47].

I.3.2 Examples of dopants

The foreign cations that integrate the alumina lattice generally replace the aluminium. Depending on their size, these cations can give rise to deformation of the crystal lattice to a greater or lesser extent. Table I.4 compares the ionic radii of the various dopants with that of aluminum. All the doping cations are larger than Al^{3+}, particularly thorium, calcium and cerium [48].

Table.I.4 Ion radii of aluminium and dopants in coordinance 6

Cation dopants	Rayon ionique (nm)
Al^{+3}	0.054
Ca^{+2}	0.1
Zr^{+4}	0.072
Th^{+4}	0.094
Ce^{+3}	0.101
Ce^{+4}	0.087

- **The case of magnesium Mg**

Magnesium Mg is an alkaline earth metal with atomic number 12. Its atomic mass of 24.3 $g.mol^{-1}$ is equivalent to that of aluminium Al (27 g.mol-1). Its cation Mg^{2+} is divalent. Mg doping will therefore lead to the formation of oxygen vacancies within the alumina lattice in order to maintain charge neutrality. Its ionic radius of around 0.72 Å in coordination VI is greater than that of aluminium (0.53 Å in coordination VI). This is why it tends to segregate at grain boundaries. Its solubility limit within the grains is nevertheless greater than that of the rare earths.

The MgO - Al_2O_3 phase diagram (figure I.17) indicates the formation of a $MgAl_2O_4$ spinel phase as soon as MgO is present [46].

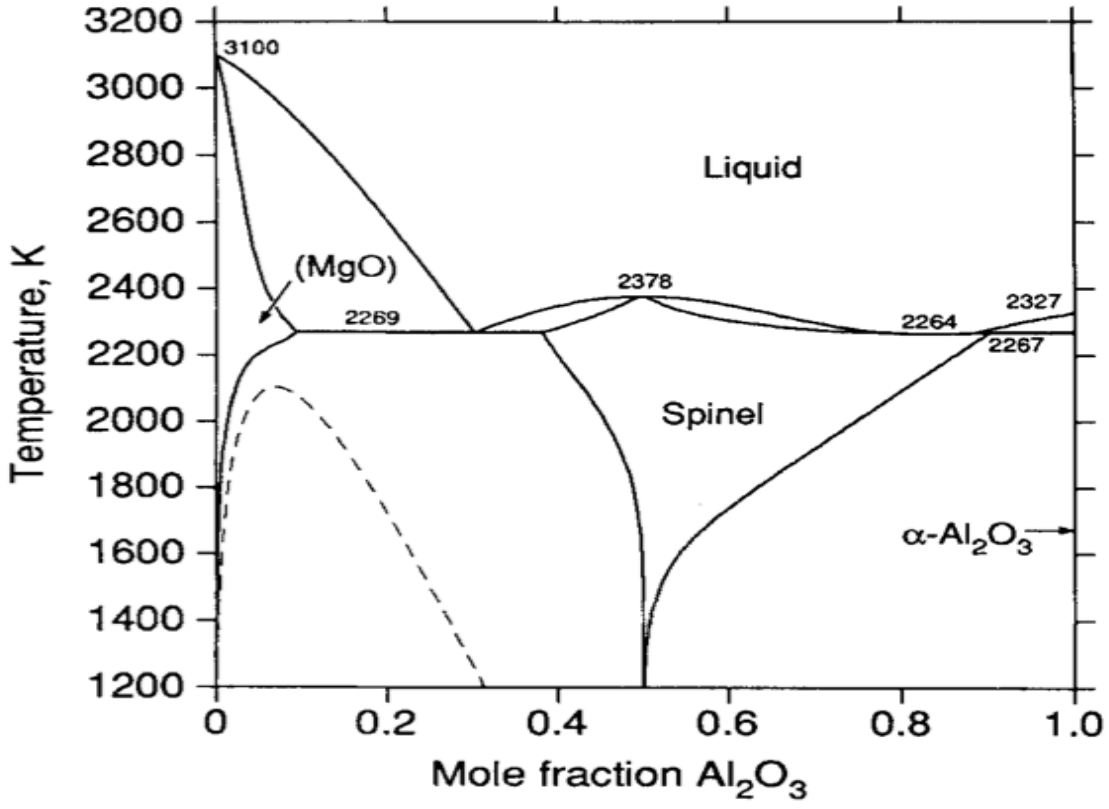

Figure.I.17 Phase diagram of the MgO-Al_2O_3 system

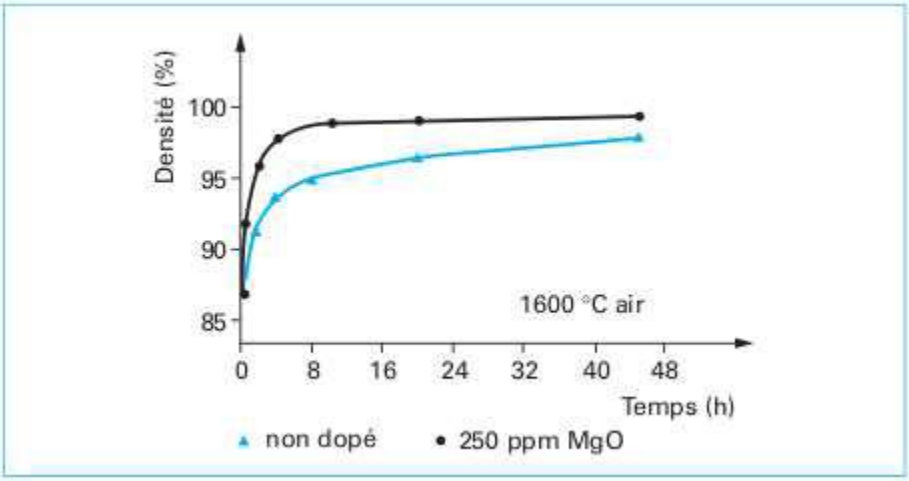

Figure I.18 Influence of MgO addition on alumina sintering [49].

Zeng et al [50] studied the influence of magnesium doping (Mg) in alpha alumina crystals (α-Al_2O_3) using ab initio calculations, based on formation energies, electronic density of states, and calculated absorption spectra. Three models of doped structures were built, in which Mg^{2+} ions replace Al^{3+} ions, as well as models of spinel structures with different aluminum/magnesium ratios. The formation energy calculations have confirmed the validity of the MgAlVo model, that is to say, the structure in which an Mg^{2+} ion substitutes an Al^{3+} ion and is accompanied by an oxygen vacancy. This model is most likely to form naturally in crystals because it is energetically more favorable. The joint presence of magnesium and oxygen vacancies introduces new defect energy levels into the band gap, modifying the electronic properties of the material.

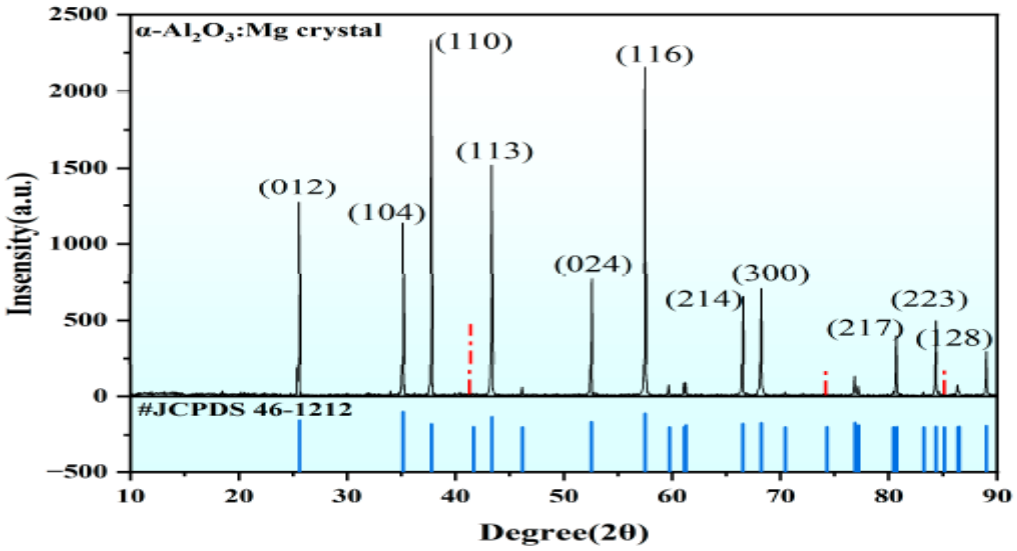

Figure I. 19 X-ray diffraction of α-$A1_2O_3$:Mg.

- **The case of lanthanum La**

Lanthanum La belongs to the rare earth family and has atomic number 57. Its atomic mass of 138.9 g.mol-1 is about five times greater than that of aluminium Al (27 g.mol-1). Its La^{3+} cation is trivalent, so La doping will not change the neutrality of alumina. On the other hand, its ionic radius of 1.03 Å in VI coordination is about twice that of Al^{3+} in similar coordination. This would result in a very low solubility within the grains (80 cat ppm). According to Galmarini's [51] simulations, this solubility would be zero. Also, lanthanum will have a strong tendency to segregate at alumina grain boundaries. The La_2O_3-Al_2O_3 phase diagram (figure I.21) indicates that a $LaAl_{11}O_{18}$ β-alumina phase or a $LaAlO_3$ perovskite phase could be formed during La doping [46].

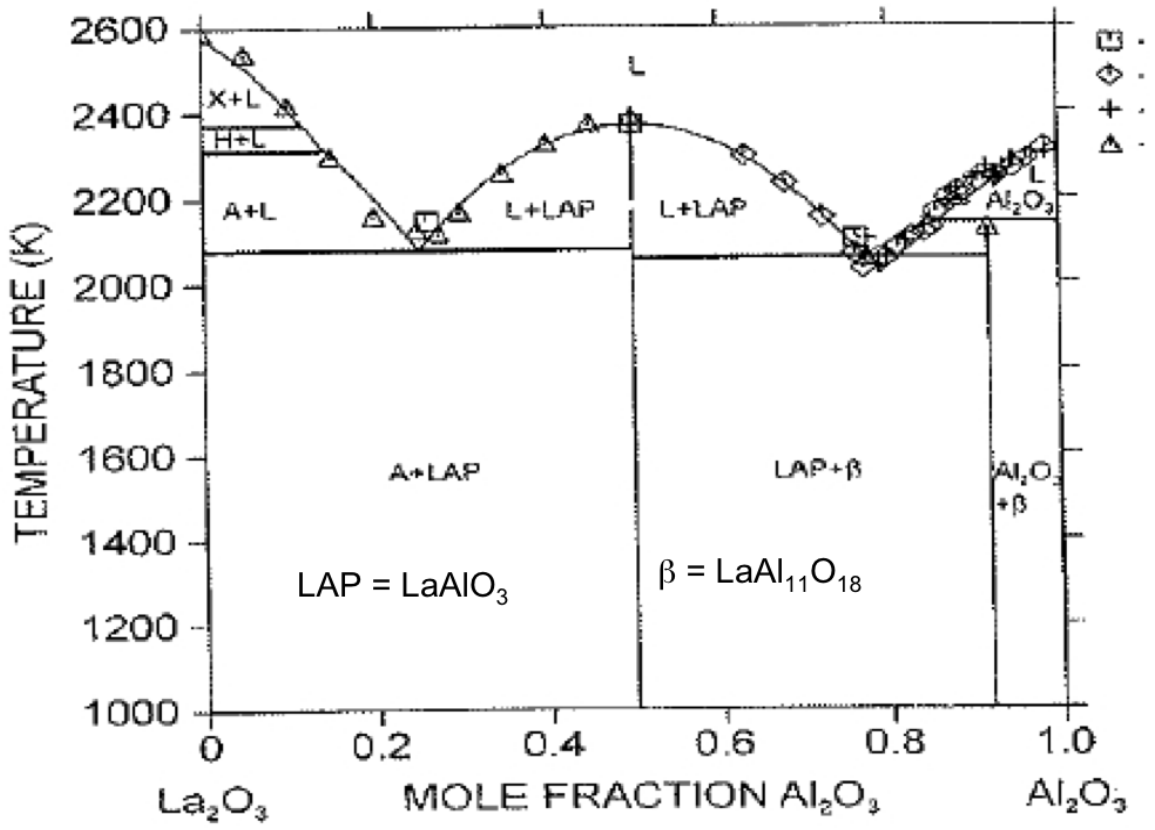

Figure. I. 20 Phase diagram of the La_2O_3-Al_2O_3 system.

- **The case of zirconium Zr**

Zirconium Zr is a transition metal with atomic number 40. Its atomic mass of 91.2 g.mol-1 is approximately three times greater than that of aluminium Al (27 g.mol-1). Its Zr^{4+} cation is tetravalent, so zirconium doping could encourage the presence of aluminium vacancies in the

alumina lattice. Its atomic radius of 0.72 Å in coordination VI, equivalent to that of magnesium, is greater than that of aluminium. However, the effects of Mg and Zr on alumina densification are opposite, with Mg favouring diffusion at grain boundaries, unlike Zr. Zirconium is known to be virtually insoluble within α-alumina grains [46].

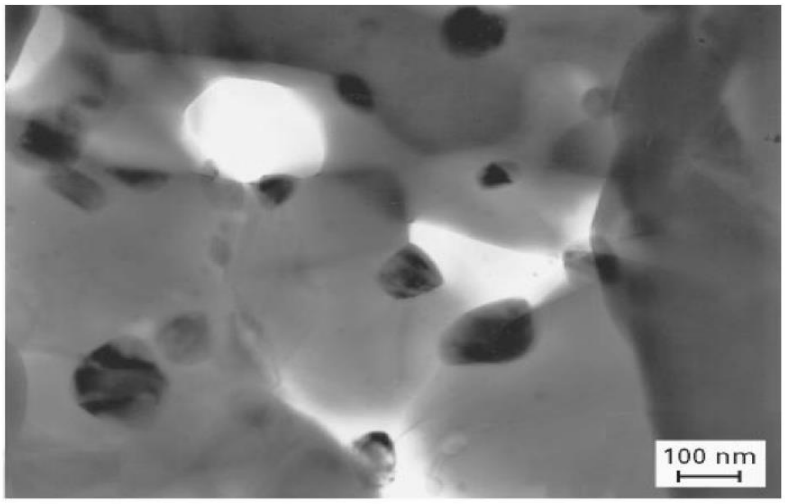

Figure I.21 Tetragonal zirconia particles (in black) at the α-alumina grain boundaries when doped with 1 mol% zirconia.

Ramazani et al [52] studied the effects of three sintering aids—magnesia (MgO), lanthanum oxide (La_2O_3), and zircon (ZrO_2) —on the optical and mechanical properties of transparent alumina ceramics. They found that the sample 100m100L300z (Z), containing 100 ppm of MgO, 100 ppm La_2O_3, and 300 ppm of ZrO_2, presented the highest infrared transmittance (71.4% to 5 µm) and visible transmittance (32% at 750 nm). This sample has also demonstrated higher mechanical properties, in particular a hardness of 19.34 GPa, a fracture toughness of 5.24 $MPa.m^{0.5}$, and a flexural strength of 356.83 MPa. These improvements are attributed to the synergistic effects of triple sintering aids, which reduce grain size, minimize porosity, and increase densification.

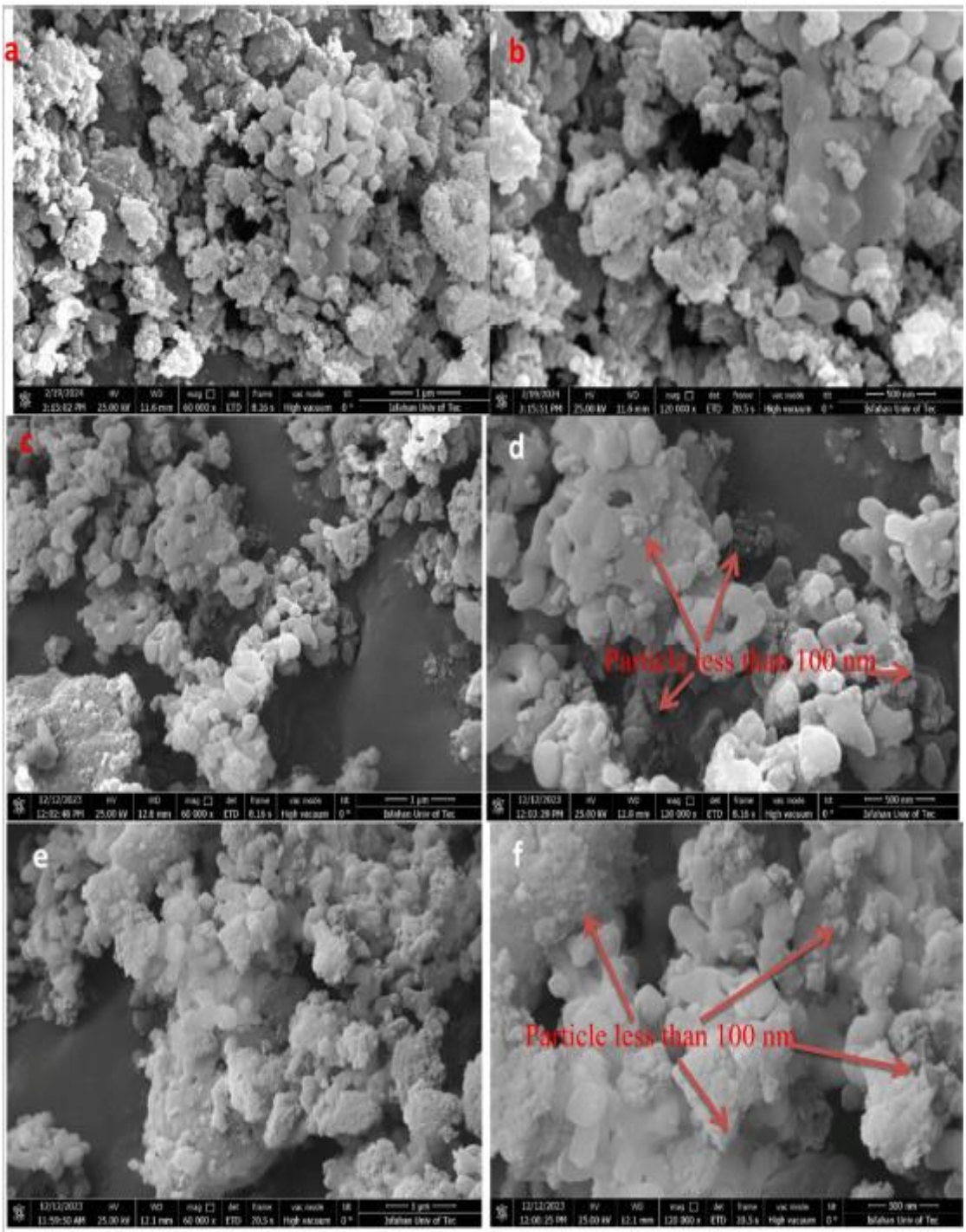

Figure I.22 Scanning electron microscopy (SEM) images of the powders: (a, b) pure alumina; (c, d) G sample(50Z100L-100M); (e, f) Z sample (300Z100L-100M).

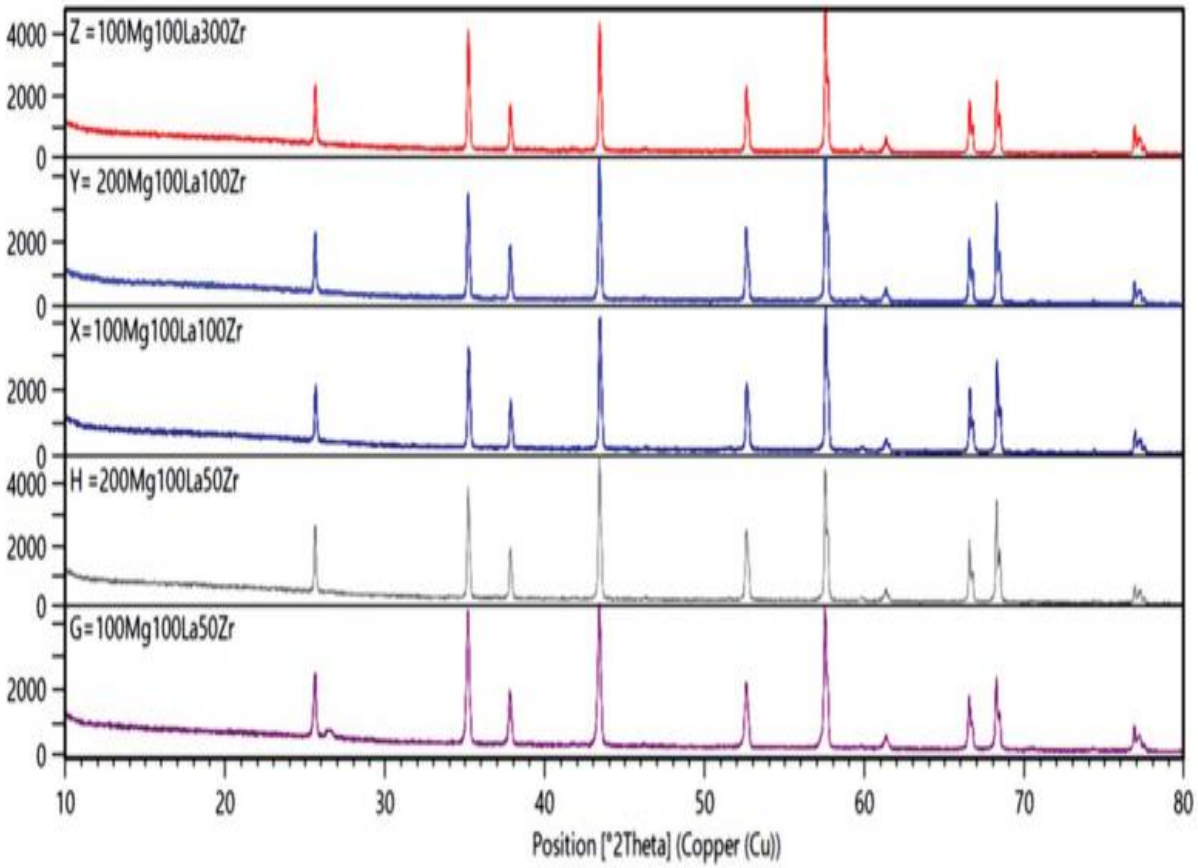

Figure I. 23 X-ray diffraction (XRD) patterns of consolidated alumina powders with different amounts of sintering aids.

- **The case of cobalt Co**

Results confirmed by Marinovi´c et al [20].The incorporation of cobalt ions into the alumina matrix promotes the apparition of spinel structures such as Co_3O_4 and CO_2AlO_4 and $CoAl_2O_4$. These phases all crystallize in the spinel structure, have very similar elementary mesh parameters, and have similar XRD diagrams, with the possibility of having phases like alpha alumina and gamma alumina.

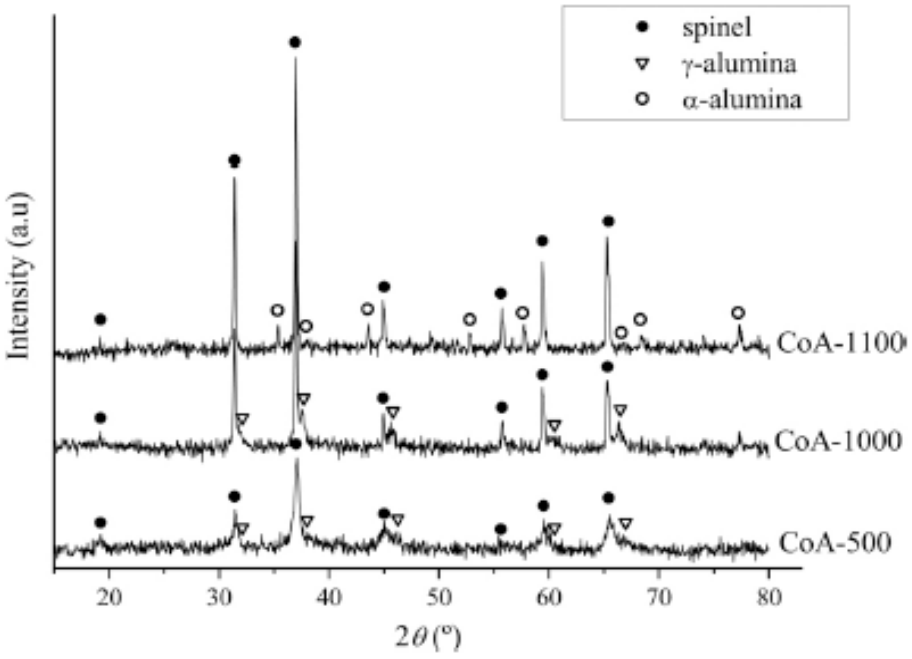

Figure I.24 XRD patterns of Co-doped alumina samples annealed at 500 ◦C, 1000 ◦C and 1100 ◦C and their phase compositions.

- **The case of manganese Mn**

Dhuban et al. [14] the incorporation of manganese ions into the alumina network promotes the appearance of pores, leading to a low-density material compared to pure alumina. The manganese promotes the decrease in the size of alumina particles. A concentration of manganese promotes the growth of grains at higher concentrations, and this effect appears to be significant at higher temperatures.

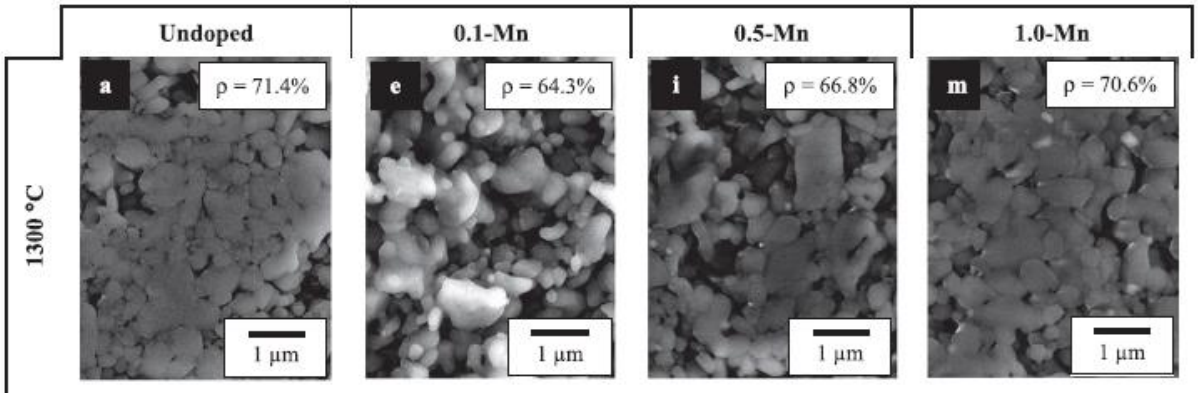

Figure I.25 Microstructural evolution of undoped and manganese-doped samples.

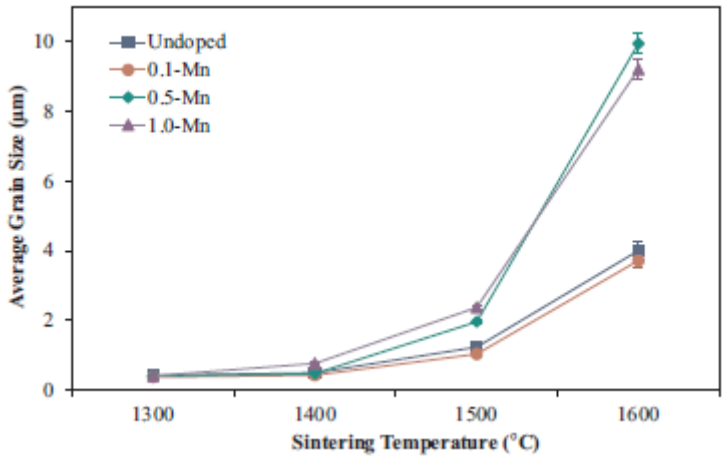

Figure I.26 Effect of sintering temperature on the average grain size of alumina ceramics.

Characterization methods and techniques

II. Introduction

In this chapter, we will present the synthetic protocol, heat treatment, as well as the different characterization techniques used.

II.1 Heat treatment

Heat treatments aim to modify the nature and distribution of the constituents of a material. Depending on the field of application of the material, treatments can improve or deteriorate its mechanical properties. In general, the thermal treatments used for ceramic powders are sintering and calcination [53].

II.1.1 Sintering

Sintering is a heat treatment technique used to produce controlled density materials of ceramic powders by application of thermal energy. Sintering is, in fact, one of the oldest human technologies, from the prehistoric era with the cooking of pottery. However, it was only after the 1940s that sintering was fundamentally and scientifically studied. Since then, remarkable progress in the science of sintering has been made. Unlike other processing techniques, various stages of treatment and variables must be taken into consideration for the production of dense ceramic parts. Sintering is a process by which the porosity of a raw ceramic body is eliminated, giving a completely dense ceramic piece. The flow of material necessary to eliminate pores can occur by different methods, from dissemination to viscous flow. Each of these processes is accelerated by increasing temperature. Once fired, ceramic wares are densified, which leads to a narrowing and a reduction in volume.

During sintering, the material will be brought to a temperature below its own melting temperature. However, the merging of certain constituents or minority phases is possible. If such processes occur, we will speak of liquid wetting, and in the opposite case, of streaming in solid phase. [54].

- **Solid sintering**

Solid-phase sintering is a process used for the development of ceramic or metallic parts from powders. It makes it possible to obtain parts with controlled microstructural properties, such as the density or the size of the final grain. After synthesis of the powders, formatting the building- often by compaction and under the effect of a heat treatment, the creep in the solid phase makes it possible to obtain, from a powdered building, a mass with higher compactness.

The heating is carried out below the melting temperature of the elements. Thermal energy is converted and induced both a creation and bond growth, called grains joint, where there is atomic or molecular diffusion between the grains of porous material. The dissemination and other physical phenomena involved lead to consolidation and densification of the environment. Several detailed mechanisms then are at the origin of the evolution of the properties of the material [55].

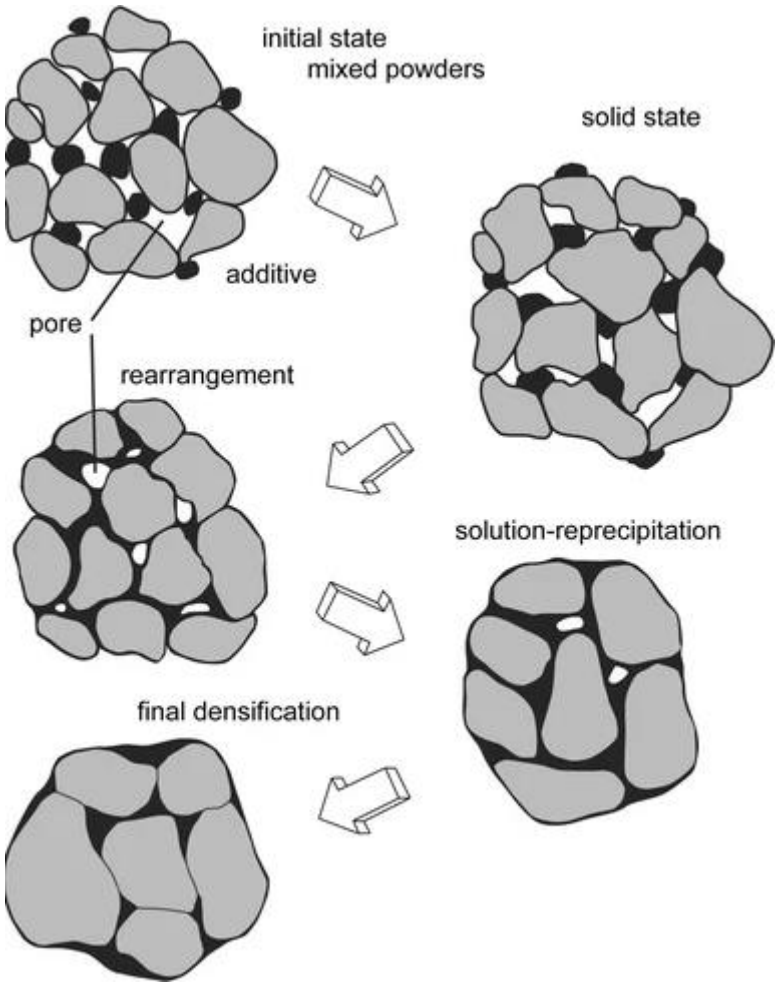

Figure II.1 Steps of sintering, called solid-state sintering [54].

- **Liquid sintering**

The sintering carried out thanks to the action of a liquid is called liquid phase sintering. This may appear by non-congruent fusion of a pure product or thanks to the introduction of an addition. The latter can consist of a compound at a low melting point or in a constituent capable

of reacting with the primary compound (for example: formation of a eutectic). From its formation, if the wetting of the particles by the liquid is sufficient, it is distributed evenly in the material and allows the rearrangement of the particles by capillarity. The compactness of the whole is thus increased. This step will be all the faster since the viscosity of the secondary phase is low and that its wetting is important. Following this phenomenon, a transport mechanism by dissolution-precipitation can take place: part of the solid dissolves in the liquid phase and preferentially precipitates at the level of the solid-liquid-gas interfaces (Figure II.2 point A). We then modify the shape of the grains in the direction of their rapprochement and therefore of a densification [54].

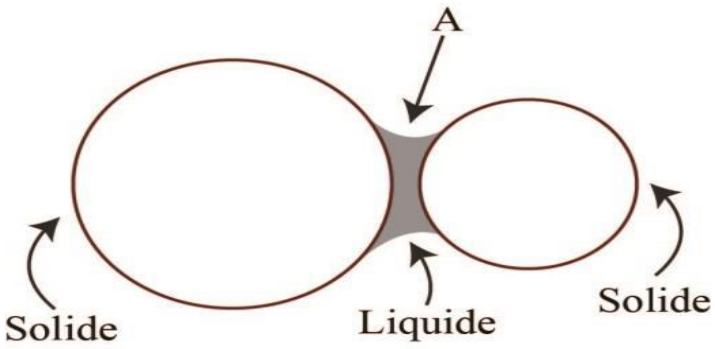

Figure II.2 Schematic representation of a liquid meniscus formed between two grains.

II.1.2 Calcination

The calcination used in this work is a method of heat treatment, which consists of eliminating humidity (H_2O), forcing the decomposition and pyrolysis of organic species, in order to obtain high-purity final products.

II.2 Synthetic protocol

As shown in Figure II.3, aluminum gels have been synthesized using a modified version of a sol-gel route, which involves modifying the precursor concentration and gelification conditions in order to optimize the structural properties of the final material. With a precursor recipe, an adapted approach to Baumann [56].

For the preparation of alumina xerogels, aluminum nitrate hexahydrate (Analytical Fluka, 99%) was dissolved in 100 ml of reagent grade ethanol (denatured ethyl alcohol, Fisher Scientific). Then, citric acid was added with magnetic stirring at a temperature of 80 °C to catalyze the gelation process.

Gelification occurred after about two hours. The frost was allowed to age for 24 hours in ambient conditions.

For cobalt-doped aluminum, cobalt nitrate was added to aluminum nitrate before adding citric acid. Likewise, for alumina that has been doped with manganese, manganese nitrate was combined with aluminum nitrate, and identical procedures were carried out until three gels were produced.

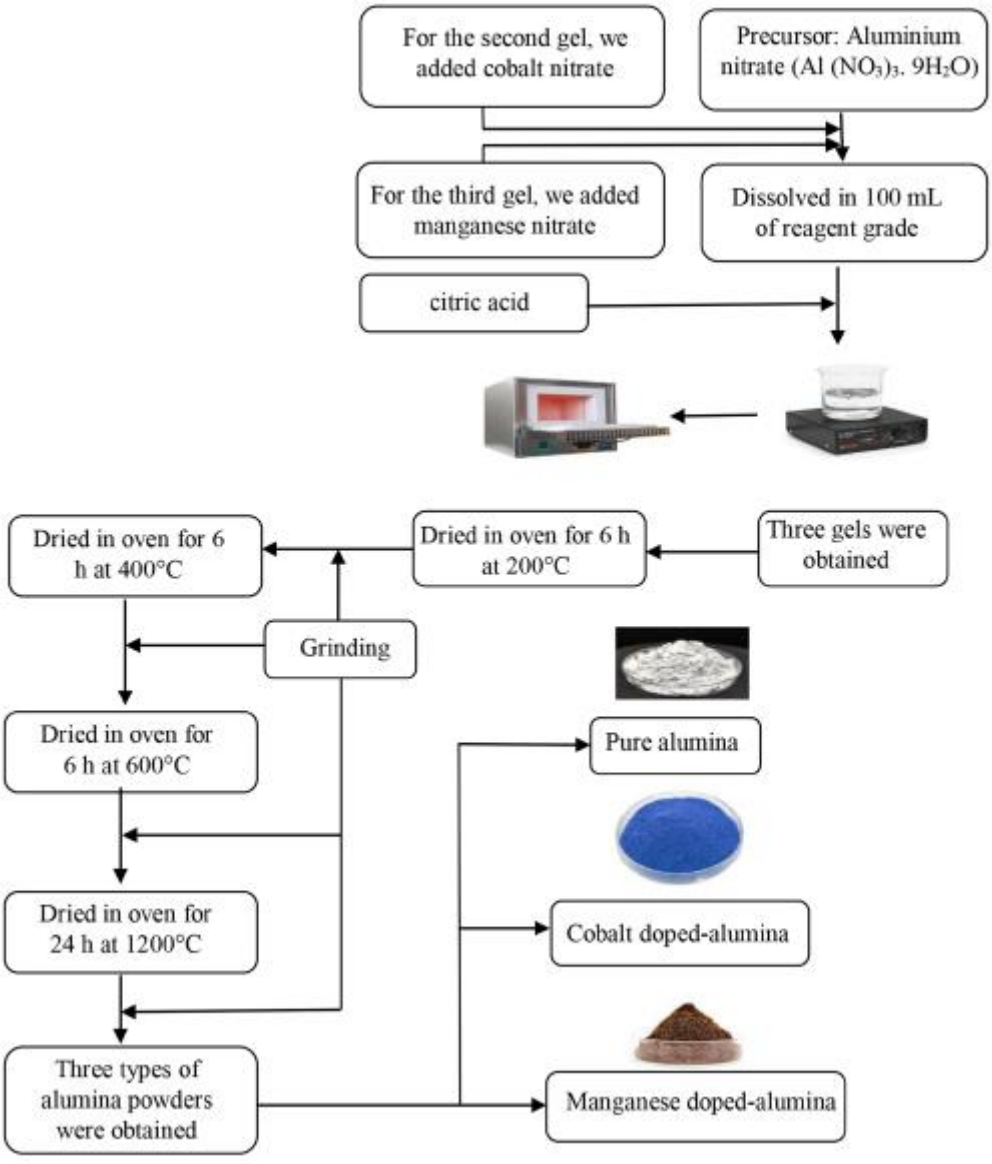

Figure II.3 Illustrative diagram of the stages of the synthetic process.

Subsequently, the samples were placed in ceramic crucibles, which were then introduced into the oven. As shown in Figure II.4, the samples were kept at temperatures of 200, 400, and 600 °C for 6 hours and underwent final treatment at 1200 °C for 24 hours, with more grinding at

the end of each treatment. After which, they were removed from the oven and transferred for a more in-depth analysis.

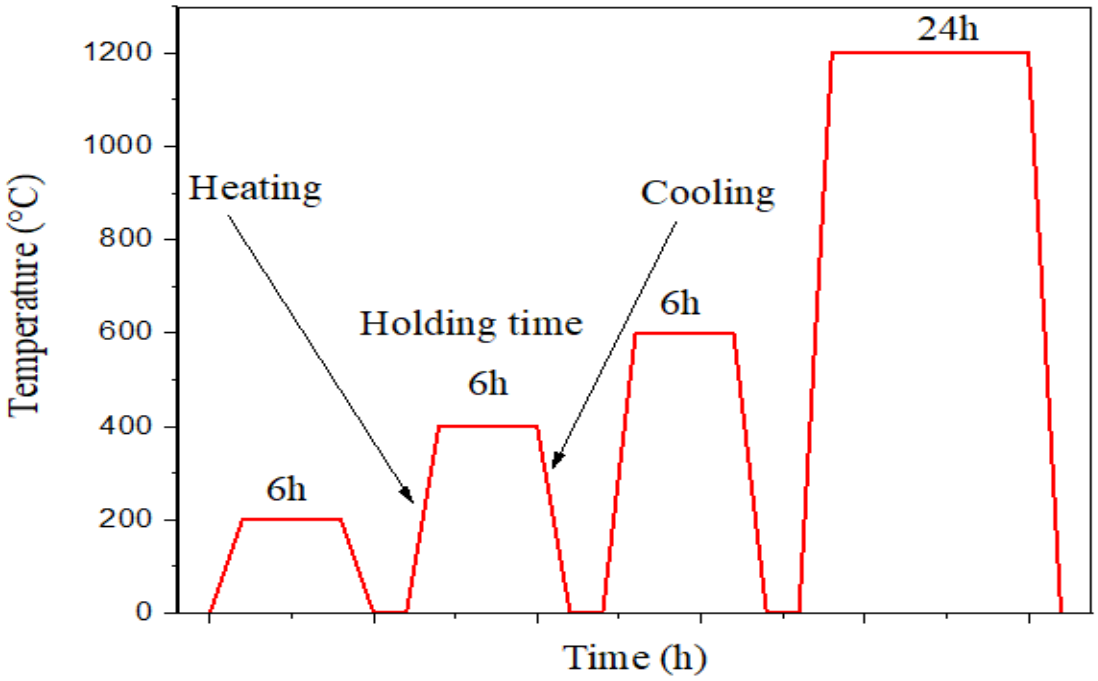

Figure II.4 Thermal cycle

II.3 Characterization techniques

II.3.1 Thermal analysis

Thermal analysis makes it possible to study, as a function of time or temperature, the thermal behavior of any material, mineral, or organic, undergoing modifications of composition or structure when it is subject to a temperature program under a controlled atmosphere. [57].

II.3.1.1 Thermogravimetric analysis (TGA)

Measures the mass of a sample using a high-sensitivity microbalance when the sample is heated under vacuum in an oxidizing, reducing, or inert atmosphere. The recorded curves, known as thermograms, were obtained under nitrogen [58].

It therefore allows the variation in mass of a sample to be measured as a function of the heat treatment temperature. This variation in mass may be a loss of mass, such as the emission of vapors, or a gain in mass, for example, when a gas is fixed [59].

II.3.1.2 Differential thermal analysis (DTA)

Differential thermal analysis (DTA) involves characterizing the thermal properties of the physical and chemical transformations of a sample by measuring the temperature difference between the sample and a thermally inert reference. The technique provides information on the energy transformations of matter: evaporation, melting, crystallization, oxidation, phase transitions, etc [57].
It allows the exothermic and endothermic phenomena that occur during the reaction to be monitored [60].

To study the evolution of mass as a function of temperature and understand the phenomena occurring during calcination at different temperatures, simultaneous differential thermal analysis (DTA) and thermogravimetric analysis (TGA) were performed using a simultaneous thermal analysis calorimeter (STA409, Netzsch, Selb, Germany) as shown in Figure II.5, in which approximately 20 mg of gel was used. The sample was heated to 1200 ◦C at a rate of 10 ◦C/min.

Figure II.5 Simultaneous thermal analysis calorimeter

II.3.2 Fourier Transform Infrared Spectroscopy (FTIR)

Infrared spectroscopy is a structural analysis method that reveals the nature of the bonds between atoms in a molecule. The principle of this method consists of measuring the amount of light absorbed by a material as a function of wavelength during an interaction between the material and electromagnetic radiation.

In the field of materials science, infrared spectroscopy is used, in addition to characterization analyses, to determine the bonds between atoms or to identify any substitutions that have occurred. Infrared spectroscopy also makes it possible to deduce how these materials evolve in relation to their environment, i.e., it allows the characterization of compounds that have been introduced into the material, such as water bound to the molecule; in this case, it is in the form of -OH, and its peak appears around 3000 cm^{-1}. Hence, the fundamental vibrations of the molecules studied are located in the mid-IR range (4000 cm^{-1} – 400 cm^{-1}) [61].

Spectroscopic methods are non-destructive and can be used alongside other conventional techniques (microscopy, DSC, XRD) for quantitative powder analysis [62].

The powders were studied by Fourier transform infrared spectroscopy (FTIR) using a Nicolet iS50 FT-IR series Thermo Scientific spectrophotometer (Figure II.6). Sample preparation consisted of mixing 1 mg of the sample with 300 mg of potassium bromide (KBr). FTIR spectra were then acquired in the wavenumber range of 4,000 to 400 cm^{-1}, with a spectral resolution of 4 cm^{-1}. This analytical approach allowed for detailed examination of molecular vibrations and provided valuable information on the chemical composition and structural characteristics of the samples.

Figure II.6 FTIR spectrophotometer.

II.3.3 UV-Visible Spectroscopy

Ultraviolet-visible spectroscopy or ultraviolet-visible spectrometry is a spectroscopic technique involving photons with wavelengths in the ultraviolet (200 nm – 400 nm), visible (400 nm – 750 nm), or near-infrared (750 nm – 1,400 nm) range. When exposed to radiation in this wavelength range, molecules, ions, or complexes are likely to undergo one or more electronic transitions. The substrates analyzed are most often in solution, but can also be in the gas phase and, more rarely, in the solid state. The electronic spectrum is the function that relates the light intensity absorbed by the sample analyzed to the wavelength.

The spectrum is most often presented as a function of absorbance as a function of wavelength. It can also be presented as the molar extinction coefficient as a function of wavelength, in which case the spectrum is independent of the concentration of the absorbing solute. This technique complements fluorescence spectroscopy, which measures the light intensity emitted by a sample when illuminated at a wavelength at which it absorbs. Fluorescence involves transitions from the excited state to the ground state, whereas absorption spectroscopy deals with transitions between the ground state and the excited state [63].

- **Beer-Lambert Law**

Consider monochromatic light passing through an absorbing solution of concentration C contained in a cuvette of thickness l. Part of this radiation will be absorbed by the sample, and part will be transmitted. Bouguer, Lambert, and Beer studied the relationships between I0 and I: the intensity of monochromatic light passing through a medium where it is absorbed decreases exponentially:

This gives us the relationship known as Beer–Lambert's law:

$$A = - \log T = \varepsilon \, l \, C.$$

* % T is the transmittance.

* ε is the molar extinction coefficient; it is a characteristic of the substance studied at a given wavelength. C : la molarity, ε: in $L.mol^{-1}.cm^{-1}$ [64].

UV-Visible analysis was performed using a Thermo Scientific Evolution 220 UV-Visible spectrophotometer (Figure II.7), and spectra were recorded between 200 and 800 nm.

Figure II.7 UV-Visible spectrophotometer.

II.3.4 Photoluminescence (PL)

The light emission of any process other than the radiation of a black body is called luminescence. Luminescence is a non-equilibrium process that needs a source of excitation, such as a laser or a lamp. According to the sources of excitation, we distinguish between photoluminescence (PL), which requires optical excitation, electroluminescence (EL), where the source of excitation is electric current, and cathodoluminescence (CL), which results from electron bombardment [65].

A photoluminescent material has the property of absorbing incident radiation and returning it in the form of a light emission. At the molecular level, the absorption of a photon allows an electron to pass to an excited state. Energy can be returned in the form of:

- Radiative phenomena, that is to say, phenomena giving rise to the emission of light. Two radiative phenomena are to be distinguished:
  - The fluorescence that results from the direct re-emission of an absorbed photon between two states of the same multiplicity of spin.
  - The phosphorescence occurs when the excited electron returns to its fundamental state from a different multiplicity state.
- Non-radiative phenomena, that is to say, phenomena where energy is dissipated without any emission of photons being observed [66].

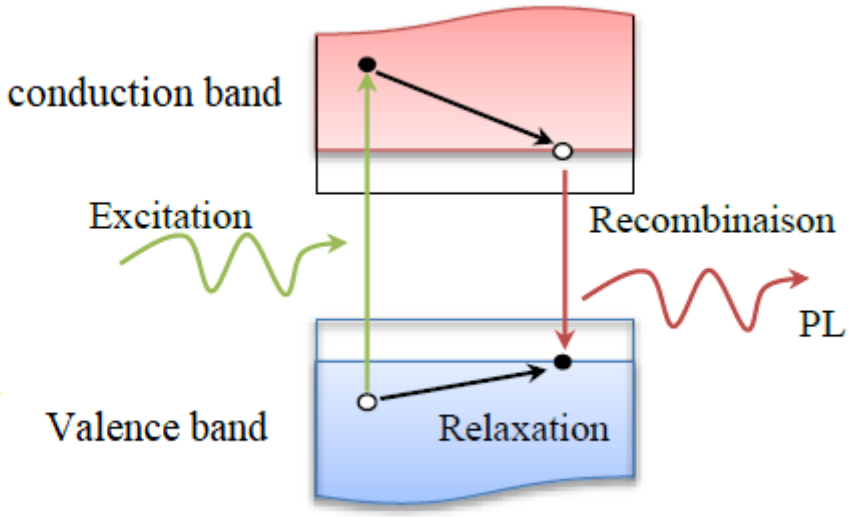

Figure II.8 The principle of photoluminescence [65].

The principle of PL is to excite electrons from the valence band with a photon of superior energy, so that they are found in the conduction band. The excitation therefore makes the electrons pass towards a higher energy state before they return to a lower energy level with emission of a photon. After a very short time (of the order of 10 nanoseconds, which can however be extended to minutes or even hours), the electron recombines and returns to the valence band by emitting a phonon (when the material is in an indirect gap), a photon, or in some cases an Auger electron. PL is only interested in the case that a photon is emitted.

During a PL measurement, the excitation energy is maintained fixed while the detection energy is swept. The luminescence emitted by the material is thus collected, and the intensity recorded according to the energy emitted from the photons, in the form of a spectrum. From this spectrum obtained, we can deduce: the size of the band gap, the impurity levels, the properties of the interface and the surface, as well as the density of states and the excitonic states. We can also collect information concerning the electronic structure by applying magnetic and electric fields in a controlled manner, or studying the effect of mechanical pressure on a material by exerting external mechanical forces, for example. Also, PL is particularly useful in the analysis of defects and discrete impurities.

PL is considered one of the experimental methods intensively used in the physics of semiconductors, particularly in materials with a large band gap, for the following reasons:

- It is not destructive, since it is based on pure optical processes.
- It requires no preparation of the samples.

- It is highly sensitive. The information collected on the electronic structure in the semiconductor can be deduced experimentally.

The inconvenience of PL is that it is connected to radiative recombination, so it is very difficult to investigate non-radiative processes, and to characterize materials with mediocre quality [65].

Photoluminescence analysis was performed using a FLS 1000 Photoluminescence Spectrometer (Figure II.9), with a 385 nm extinguishing wavelength and spectra were recorded between 600 and 750 nm.

Figure II. 9 Photoluminescence Spectrometer

II.3.5 X-ray diffraction

X-ray diffraction is a non-destructive structural investigation technique widely used to characterize solid materials in powder form. It allows the identification of different crystalline phases and the determination of the average size of crystallites [67, 68].

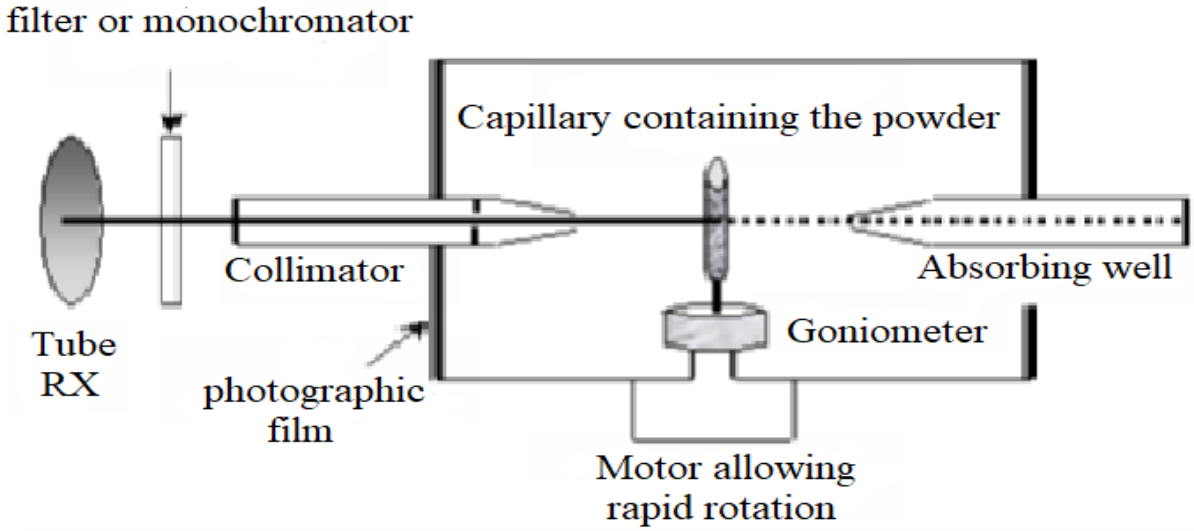

Figure II. 10 Schematic diagram of X-ray diffraction on powders

II.3.5.1 Principle of X-ray diffraction

The crystalline state is characterized by the tri-periodic distribution of an atomic pattern in space. This orderly distribution forms parallel and equidistant planes called lattice planes (h, k, l). The inter-lattice distances are in the range of 0.15 to 15 Å and depend on the arrangement and diameter of the atoms in the crystal lattice. These distances are characteristic constants of the crystal and can be calculated using X-ray diffraction. The wavelength of X-rays (0.2 Å < λ < 2 Å) is of the same order of magnitude as the interatomic distances (a few Å).

The phenomenon of diffraction is based on the interaction between X-rays and crystalline matter. It is a reflection on a series of planes in the crystal. When an X-ray beam is directed at a crystallised product, part of it (the largest part) is absorbed, while another part is reflected by the lattice planes (Figure II.11). In fact, this radiation causes a displacement of the electron cloud around the nucleus, which induces the re-emission of an electromagnetic wave of the same nature through Rayleigh scattering. These re-emitted waves will interfere with each other in a destructive or constructive manner. Depending on the direction given in space, a greater or lesser flux of X-photons will be collected: these variations, depending on the direction, constitute the phenomenon of X-ray diffraction. [69].

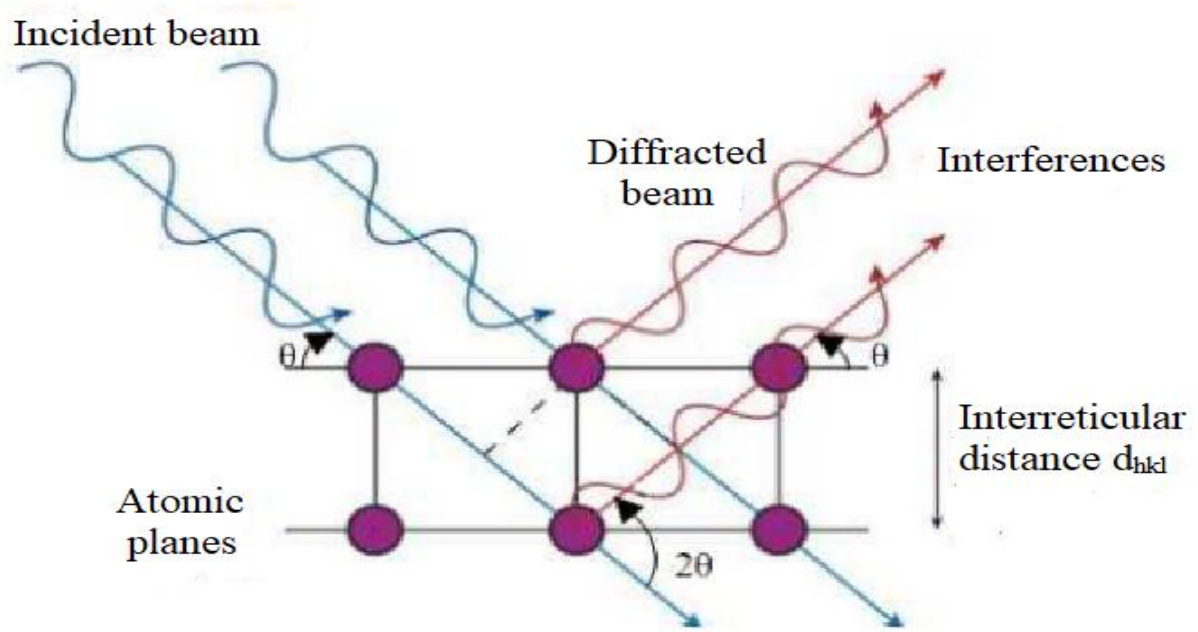

Figure II.11 X -ray diffraction by reticular plans.

II.3.5.2 Bragg law

When the difference in walking between the incident rays and the rays diffracted by the atoms is a whole number of times the wavelength, there is constructive interference. Or 2θ the angle between the direction of the incident rays and that of the diffracted rays.

There is constructive interference when Bragg's law is satisfied:

$$n\lambda = 2d_{hkl}.\sin(\theta)$$

Where dhkl is the interreticular distance of the family (h k l), θ is the angle between the incident beam of the X-rays and the diffracting planes, λ is the corresponding wavelength, and n is the order of diffraction.

Bragg's condition is more generally reflected in the following vector equality:

$$\vec{Q} = \vec{R} = \overrightarrow{kd} - \overrightarrow{ko}$$

Where $\overrightarrow{k0}$ and $\overrightarrow{kd}$ are respectively the incident and diffracted beam vectors, $\vec{Q}$ the diffusion vector and $\vec{R}$he vector of the reciprocal network, which is expressed by the following relation:

$$\vec{R} = \overrightarrow{ha*} + \overrightarrow{kb*} + \overrightarrow{lc*}$$

Where h, k, l are the signs of Miller and $\overrightarrow{a*}$, $\overrightarrow{b*}$ et $\overrightarrow{c*}$ are the basic vectors of the reciprocal network [70].

The composition of the phase was determined by X-ray diffraction (X-ray Diffractometer Panalytical® Empyrean Series 3) (Figure II.10). For this analysis, the diagrams were acquired in a range of 20° ≤ 2θ ≤ 140° using the Cu-Kα radiation (wavelength: 1.540598 Å) from a conventional source operating at 40 kV, 40 mA, a step size of 0.017° and a counting time of 120 s/step.

The average size of crystallites has been calculated according to the Scherrer formula, which is as follows:

$$D = \frac{0.98\lambda}{\beta \cos\theta}$$

With 0.89 representing the shape factor, λ is the wavelength of X-rays, β is the width at half maximum of the diffraction peak (FWHM), and θ is the diffraction angle [71].

Figure II.12 X -ray diffractometer.

II.3.6 Microstructure morphology

II.3.6.1 Optical microscope

The appearance of the first optical microscopes at the beginning of the 17th century marks the beginning of the history of microscopy. Bright-field optical microscopy is the very first microscopy technique developed. An ocular, an objective, and a precision position compared to a sample make it possible to directly observe with the eye an enlarged image of it. The sample is lit from behind so that the light crosses it before being collected by the objective. The mechanisms of absorption and diffusion of light in the sample make it possible to obtain a contrast in the image. The theoretical resolution limit that such a system can reach is around 200 nm [72].

Microstructural observations of the powder were made using the ZEISS optical microscope (Figure II.13) of the University of Bejaia.

Figure II.13 Optical microscope.

II.3.6.2 Distribution of particles sizes (DPS)

The particles of a system rarely have a single size. The variation in the size of the particles is represented in the form of a distribution. DPS is a function that represents the variation in relative frequencies of a quantity, typically the number, surface, or volume, of particles present in the sample according to their sizes. The DPS is the representation of the experimental results

of the particle size analysis. The sample of particles on which the measurement is performed is supposed to be representative of the whole of the particulate matter.

The DPS can be weighted in number, surface, volume, or mass, or in intensity, depending on the property measured by the technique used for particle size. The number DPS represents the relative number of particles as a function of their sizes, and the DPS in intensity represents the relative intensity of the light diffused by the particles. A DPS with a certain weighting can be converted into a DPS with another weighting under certain hypotheses, on the shape of the particles, for example. The mass DPS and that in volume are equal if all the particles of the sample have the same density [73].

II.3.6.3 Scanning electron microscope (SEM)

The scanning electron microscope makes it possible to obtain images of surfaces of almost all solid materials (massive, powder, etc.), to scales ranging from X30 to X10000 or more. The SEM consists of an electronic column, an ordinary vacuum chamber, a vacuum system (10-5 to 10-6 Mbar), the electronic part, and a piloting system of the SEM as well as a workstation. The SEM allows you to make different types of images, in secondary electrons (SE) or in backscattered electrons (BSE). The SE images present a relief effect, while the BSE images have a contrast linked to the sample chemistry. The EDS detector can be used to analyze the chemical composition of the sample, producing an X-ray spectrum, where the position of the peaks characterizes each chemical element. Certain SEMs do not obtain information on the lightest elements [74].

The powder microstructures were observed using a scanning electron microscope (SEM) (ILOL JSM6360LV) (Figure II.14).

Figure II.14 Scanning electron microscope (SEM)

Results and discussions

III. Introduction

In this chapter, we will present the different results of qualitative and quantitative analysis such as, DTA/TGA, FTIR, Uv-Visible, Photoluminescence (PL), XRD and morphology of the structure using optical microscope and scanning electron microscope.

III.1 Thermogravimetric analysis

III.1.1 Pure alumina

Thermogravimetric analysis results obtained for the pure alumina are shown in **Figure III.1**

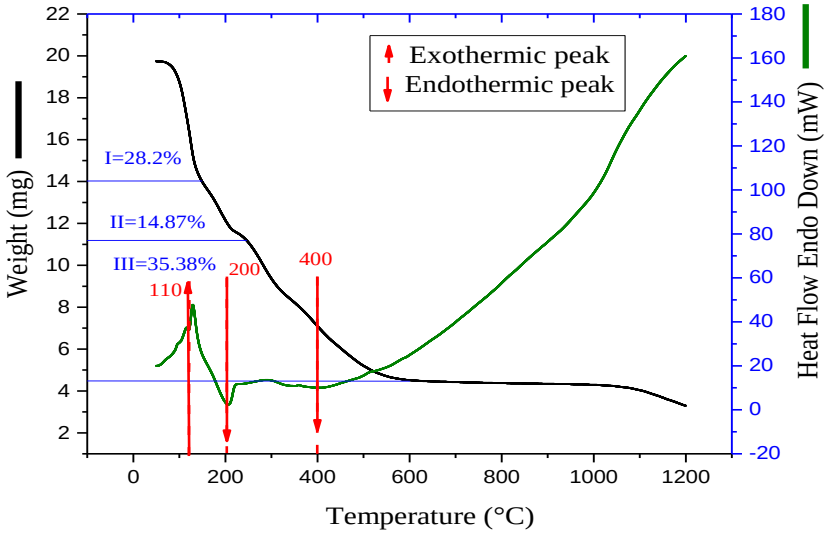

Figure III.1 Thermogravimetric analysis of Al_2O_3

Thermogravimetric analysis highlights a first mass loss of 28.2% between 50 and 150 °C and is accompanied by an endothermic peak around 110 °C, attributed to the dehydration of precursors. A second mass loss of 14.87% is observed between 150 and 220 °C. It is attributed to the decomposition of precursors as well as the pyrolysis of organic species and is accompanied by an endothermic peak located around 200 °C marking this step. A third mass loss of 35.38 % is recorded in the range of 250 to 600 °C, accompanied by a slight endothermic peak around 400 °C, corresponding to the decomposition of organic residues. Beyond 600 °C, up to 1200 ° C, no significant mass variation is detected, indicating the absence of by-products or major transformations, which suggests the progressive crystallization of alumina [75, 76].

III.1.2 Cobalt-doped alumina

Thermogravimetric analysis results obtained for the cobalt-doped alumina are shown in **Figure III.2**

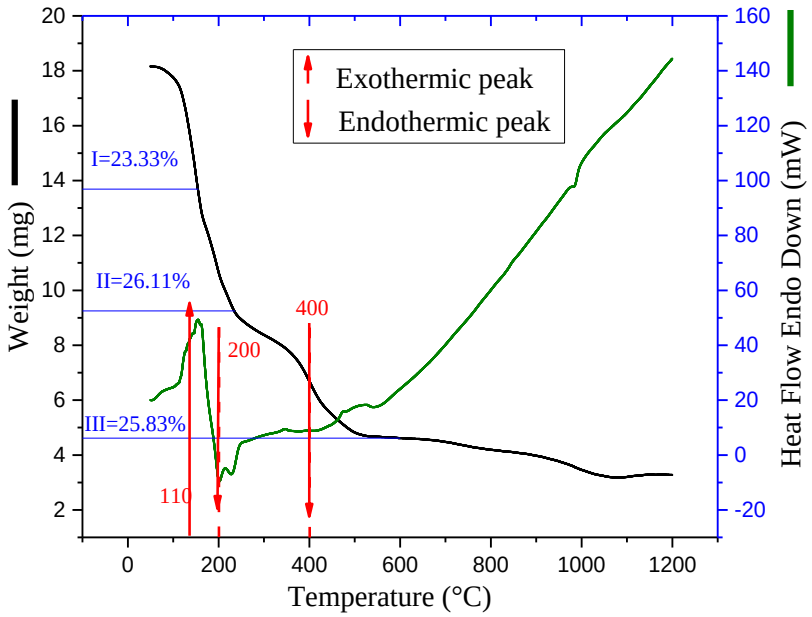

Figure III.2 Thermogravimetric analysis of cobalt-doped alumina.

Thermogravimetric analysis showed us three mass loss ranges.

-A first mass loss of 23.33% between 50 and 150 °C and is accompanied by an endothermic peak around 110 °C, attributed to the dehydration of precursors.

-A second mass loss of 26.11% between 150 and 220 °C. It is attributed to the decomposition of precursors as well as the pyrolysis of organic species and is accompanied by an endothermic peak located around 200 °C marking this step.

- A third mass loss of 28.83 % between 250 to 600 °C, accompanied by a slight endothermic peak around 400 °C, corresponding to the decomposition of organic residues. Beyond 600 °C, up to 1200 ° C, no significant mass variation is detected, indicating the absence of by-products or major transformations, which suggests the progressive crystallization of alumina. [76, 77]

III.1.3 Manganese-doped alumina

Thermogravimetric analysis results obtained for the cobalt-doped alumina are shown in **Figure III.3**

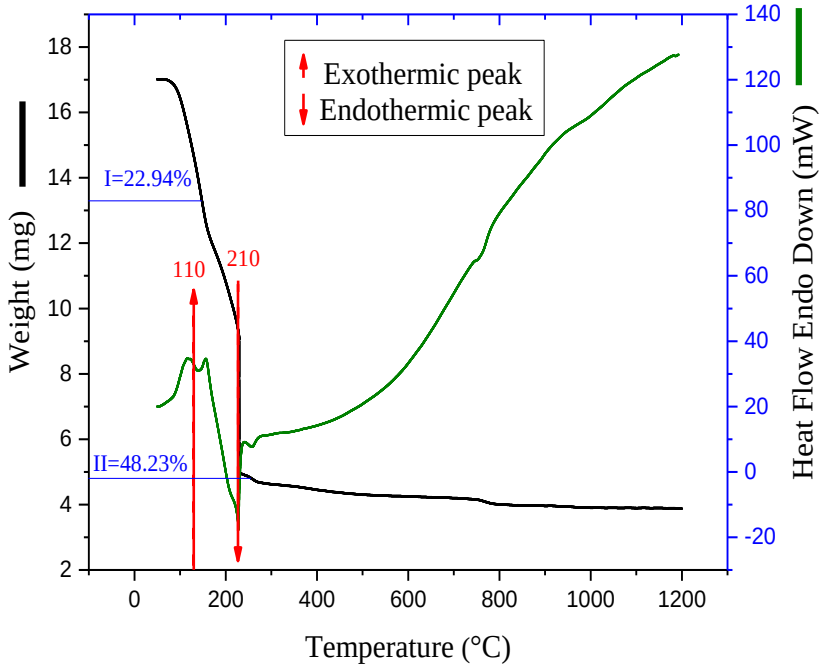

Figure III.3 Thermogravimetric analysis of manganese-doped alumina.

Thermogravimetric analysis showed us two mass loss ranges.

- A first mass loss of 22.94% between 50 and 150 °C and is accompanied by an endothermic peak around 110 °C, attributed to the dehydration of precursors.

- A second mass loss of 48.23% between 150 and 220 °C. It is attributed to the decomposition of precursors as well as the pyrolysis of organic species and is accompanied by an endothermic peak located around 210 °C marking this step.

Beyond these temperatures up to 1200°C, no significant mass variation is detected, indicating the absence of by-products or major transformations, which suggests the progressive crystallization of alumina. [75, 78]

III.2 Thermodynamics and diagram phases

The study of thermodynamics and phase diagrams provides a fundamental framework for understanding the stability, transformations, and equilibria of materials under varying temperature and compositional conditions.

In ceramic systems such as Al_2O_3–CoO and Al_2O_3–MnO, thermodynamic modelling allows the identification of stable and metastable phases, the prediction of phase boundaries, and the evaluation of Gibbs free energy variations that govern solid–liquid equilibria and compound formation.

By combining experimental observations with CALPHAD-based calculations (e.g. using Thermo-Calc software), it becomes possible to rationalize the phase evolution during synthesis and heat treatment, and to correlate theoretical stability domains with the microstructural and crystallographic changes observed in doped alumina powders [79].

III.2.1 Pure alumina

Understanding the aluminum–oxygen (Al–O) phase diagram is essential for interpreting the thermodynamic stability and formation mechanisms of alumina (Al_2O_3). This binary system defines the phase equilibria, melting behavior, and chemical interactions between metallic aluminum and its oxide, and thus provides a fundamental thermodynamic framework for analyzing oxidation, sintering, and high-temperature reactions in alumina-based materials.

In particular, the formation of α-Al_2O_3 (corundum) represents a critical stage, as this phase is the most stable and refractory form of alumina.

The following figures (III.4-III.6) summarize the key thermodynamic characteristics of the Al–O system, including its phase equilibria, Gibbs energy relationships, and temperature-dependent phase evolution [79].

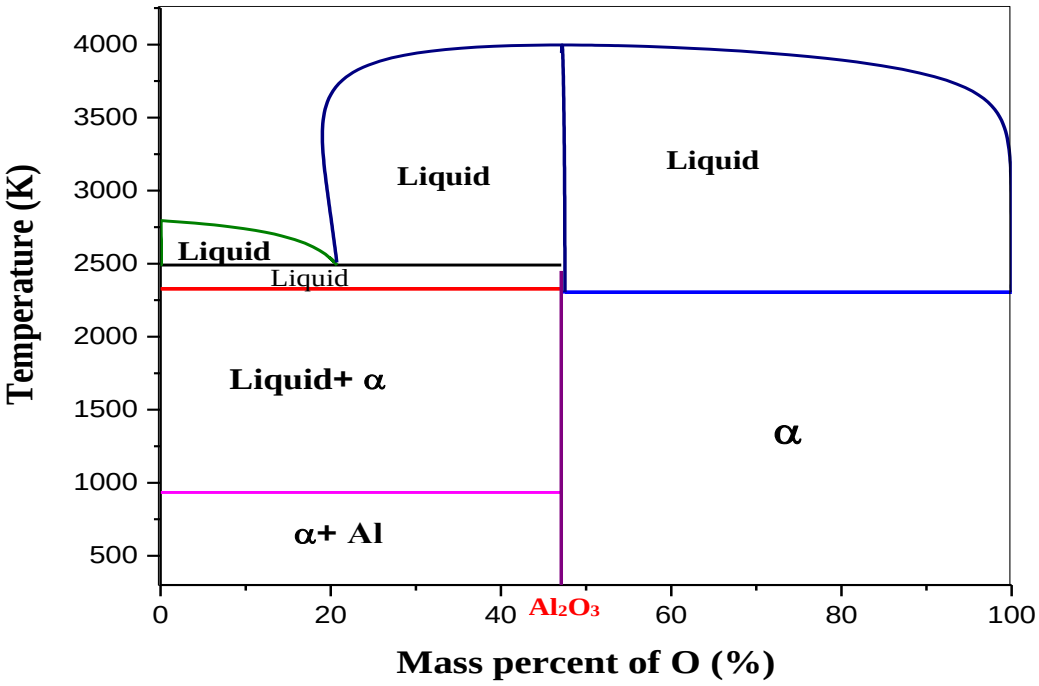

Figure III.4 Binary phase diagram of Al-O.

Figure III.4 shows the binary phase diagram of the aluminum–oxygen (Al–O) system. For alloys containing 0–47 mass % oxygen, the mixture remains fully liquid at very high temperatures. Upon cooling below approximately 2400 K, solidification begins through the formation of the α-alumina (α-Al_2O_3) phase, accompanied by a small amount of residual liquid. As cooling continues to below 900 K, this system transforms into a two-phase solid mixture of metallic aluminum and α-alumina.

For alloys containing more than 47 mass % oxygen, the system is likewise liquid at high temperatures, but solidifies directly into a single α-alumina phase upon cooling below 2400 K, without the formation of secondary phases.

The vertical line at 47 mass % O corresponds to the stoichiometric compound Al_2O_3, which melts at a fixed temperature, confirming the formation of a chemically well-defined oxide with congruent melting behavior.

In other words, this composition represents the thermodynamic boundary between metallic aluminum and its stable oxide, corundum, which dominates the solid domain of the Al–O system [79].

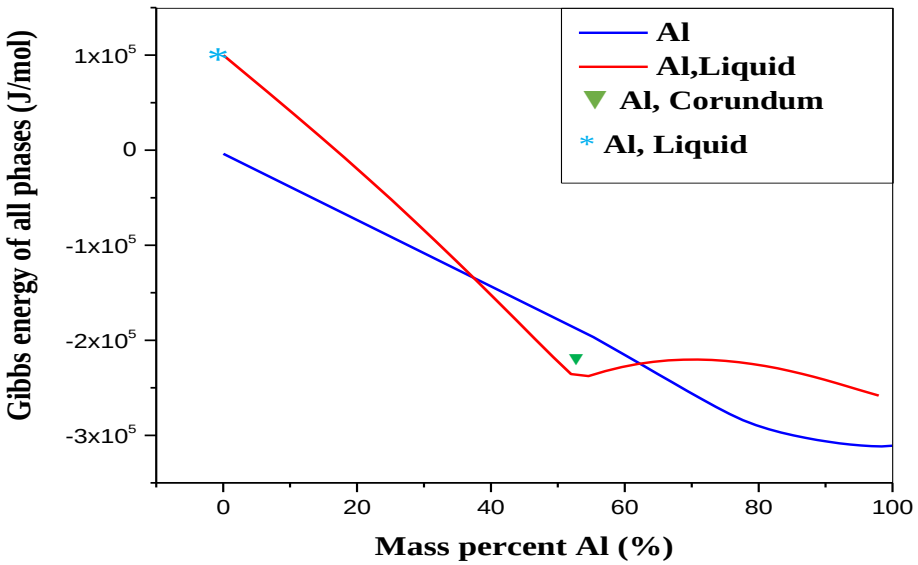

Figure III.5 Gibbs energy of Al-O system.

Figure III.5 illustrates the variation of Gibbs free energy (G) as a function of aluminum content for the different phase states within the binary Al–O system.

In Thermo-Calc, the molar Gibbs free energy (G^m) of a phase is described as:

$$G^m = \sum_i X_i G_i^0 + RT \sum_i X_i \ln X_i + G_{excess}$$

Where:

- x_i= mole fraction of component *i*
- G_i^0= standard molar Gibbs energy of pure component *i* in the phase
- R = universal gas constant
- T = absolute temperature (K)
- G_{excess} = excess Gibbs energy (accounts for interactions between species)

Two main decreasing trends are observed — one for solid aluminum and one for the liquid mixture. The progressive reduction in Gibbs energy with increasing Al content signifies an increase in the thermodynamic stability of these phases.

At low (< 40 %) and high (> 60 %) aluminum contents, the solid aluminum phase has the lowest Gibbs energy, making it thermodynamically the most stable in these regions. Conversely, near 50 % aluminum, corresponding to Al_2O_3 stoichiometry, the corundum phase (α-Al_2O_3) exhibits the minimum Gibbs energy, indicating that it is the most stable compound under equilibrium conditions.

This sharp energy minimum reflects the strong Al–O ionic–covalent bonding characteristic of corundum, which greatly reduces the system's Gibbs free energy and ensures the exceptional chemical stability of Al_2O_3 [80].

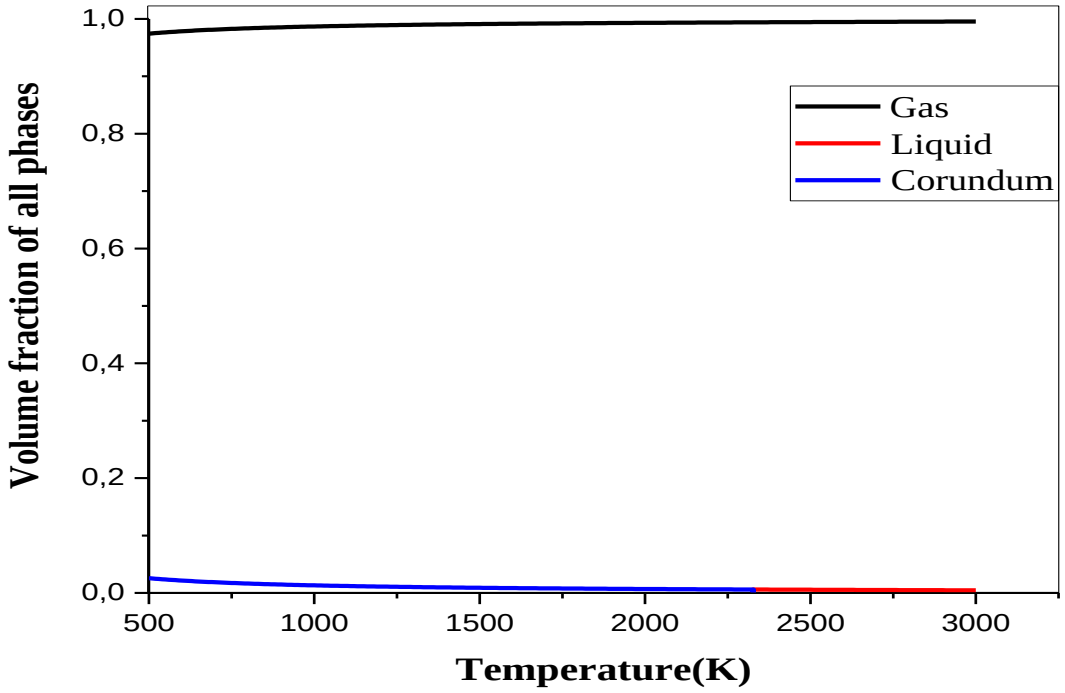

Figure III.6 Volume fraction of all phases in the Al-O system.

Figure III.6 presents the temperature dependence of the volume fraction of the phases present.

At temperatures below 2350 K, the corundum phase dominates, confirming its thermodynamic stability in this temperature range.

As temperature increases above 2350 K, the volume fraction of corundum decreases while a liquid phase gradually appears, marking the onset of melting.

This transition indicates that above this temperature, the Gibbs energy of the liquid phase becomes lower than that of the solid α-alumina, initiating partial fusion and progressive destabilisation of the solid lattice [80].

III.2.2 Cobalt-doped alumina

Figure III.7 represents the binary phase diagram resulting for the system containing Al_2O_3 and Co_2.

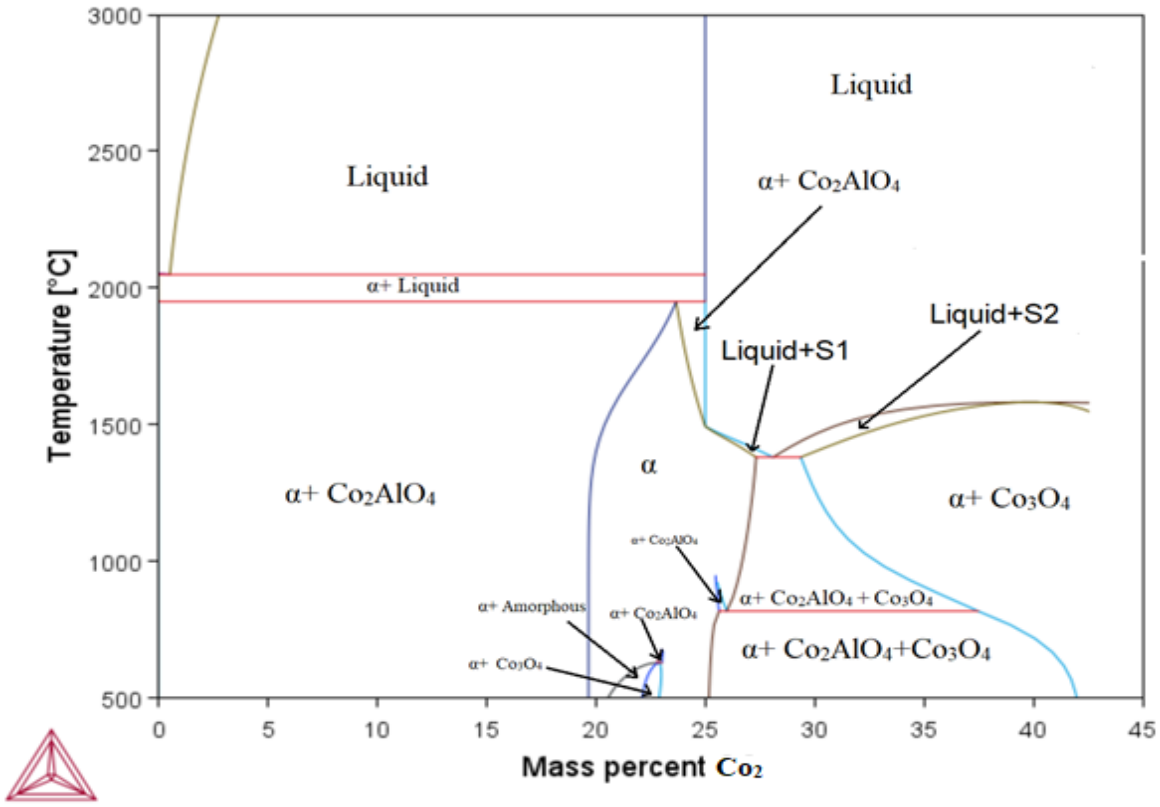

Figure III.7 Binary phase diagram of Al_2O_3-Co_2

The Al_2O_3–Co_2 binary system represents a fundamental thermodynamic framework for understanding the formation, stability, and phase evolution of cobalt-doped alumina materials. The introduction of cobalt ions into the alumina matrix profoundly modifies its structural, optical, and magnetic properties, making it a key system for the design of advanced functional ceramics and catalytic oxides. From a thermodynamic standpoint, the Al_2O_3–Co_2 phase equilibria reveal the conditions under which cobalt ions are incorporated

into the alumina lattice and the limits of solubility beyond which secondary cobalt oxide phases (e.g., Co_3O_4 or CoO) precipitate.

In the context of the present work, which involves sol–gel synthesis and thermal treatment of cobalt-doped alumina powders**,** the Al_2O_3–Co_2 system provides valuable predictive insight into the phase transformations observed experimentally**.** By combining CALPHAD-based modelling (using Thermo-Calc) with the experimental results obtained from XRD, FTIR, and other characterization techniques, it becomes possible to rationalize the phase formation mechanisms and correlate them with the observed structural evolution**.** Therefore, examining this thermodynamic system not only clarifies the stability domains of α-Al_2O_3, Co_2AlO_4, and Co_3O_4**,** but also supports the interpretation of doping behavior and the optimization of synthesis conditions for achieving uniform and stable cobalt incorporation within the alumina network.

At very high temperatures, the mixture is entirely liquid, and solidification begins below approximately 2000 K. At low cobalt concentrations (< 20 %), cobalt aluminate ($CoAl_2O_4$) appears as the primary solid phase. As the cobalt content increases between 20–25 %, α-alumina (α-Al_2O_3) remains dominant, while small amounts of cobalt oxide (CoO/Co_3O_4) coexist.
Beyond 25 % Co, the cobalt oxide phase becomes predominant, indicating a shift in phase stability toward Co-rich compositions.

This evolution can be interpreted in terms of cation substitution and solubility limits within the spinel lattice:

At low Co concentrations, Co^{+2} ions readily substitute for Al^{+3} in the spinel framework, forming a solid solution with strong Al–O–Co bonding and good miscibility in the spinel structure. However, as the cobalt content increases beyond the solubility limit, excess Co^{+2} ions cannot be stabilized within the Co_2AlO_4 lattice. They therefore segregate and precipitate as Co_3O_4, a secondary oxide phase.

This behavior reflects the limited substitutional capacity of the spinel network and the competition between the formation enthalpies of Co_2AlO_4 and Co_3O_4, both of which are stable under oxidizing conditions but in distinct compositional domains [81].

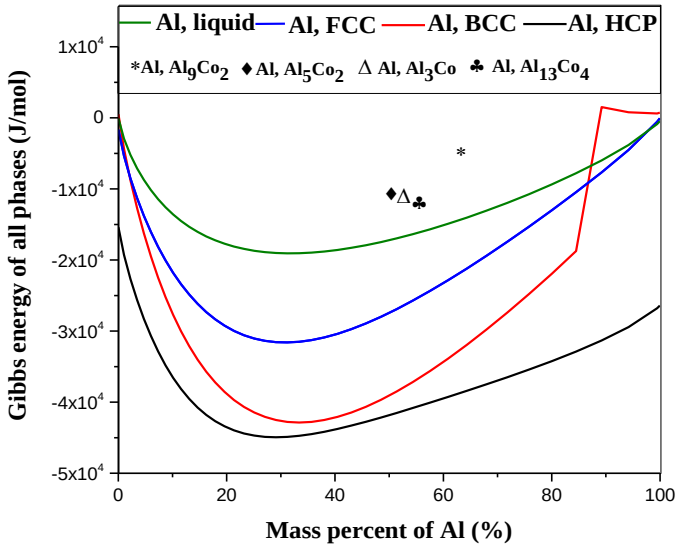

Figure III.8 Gibbs energy of Al-Co system.

Figure III.8 presents the Gibbs free energy (G) as a function of aluminium mass fraction for various phases within the binary Al–Co system.

At low aluminium contents (< 30 %), the Gibbs energy curves exhibit a downward trend, indicating increasing thermodynamic stability of the corresponding Co-rich phases. Among these, the hexagonal close-packed (HCP) cobalt phase shows the lowest Gibbs energy, confirming it as the most stable phase in this range.

In contrast, the liquid phase displays the highest Gibbs energy, and is thus thermodynamically less stable at these compositions.

Beyond approximately 30 % aluminum, the Gibbs energy of all phases begins to rise, signifying a progressive destabilization of Co-rich structures as aluminum becomes dominant.

This trend implies that the stability domain of Co-based metallic or oxide phases lies predominantly below 30 % Al, whereas the alumina-rich region becomes increasingly stable at higher aluminum concentrations.

The intersection points between the Gibbs energy curves of different phases correspond to phase boundaries, and these determine the equilibrium tie lines in the Al–Co phase diagram [82].

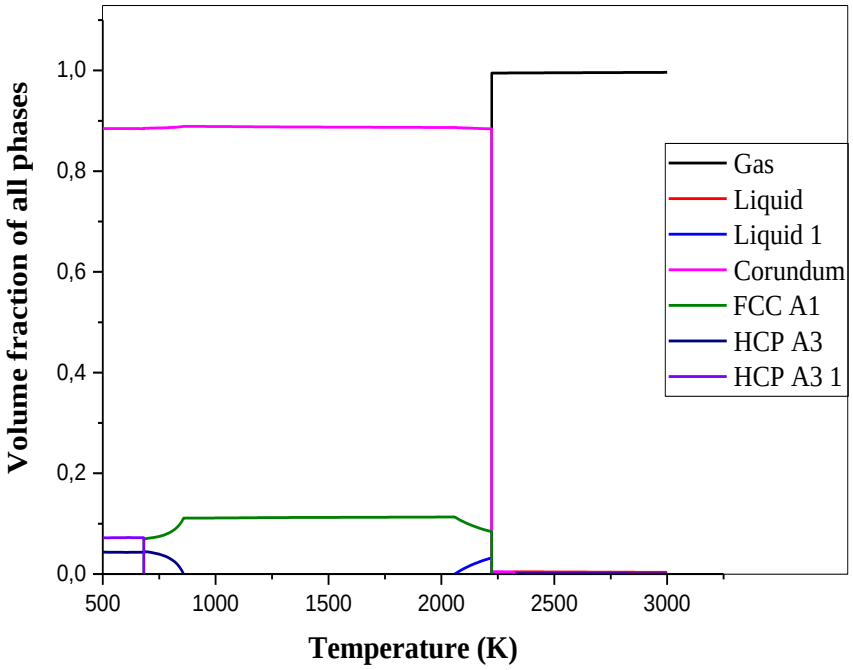

Figure III.9 Volume fraction of all phases in the Al-Co system.

Figure III.9 depicts the temperature dependence of the volume fraction of phases within the Al–Co system.

At temperatures below approximately 700 K, the system consists predominantly of two corundum-type alumina phases coexisting with the hexagonal close-packed (HCP) cobalt phase. As temperature increases, the HCP cobalt progressively transforms into the face-centred cubic (FCC) cobalt phase, reflecting the allotropic transformation characteristic of metallic cobalt, which occurs above 700 K.

At temperatures exceeding 2000 K, the volume fractions of both corundum and FCC cobalt decrease, while the liquid fraction steadily increases, marking the onset of melting. This behaviour indicates that, at high temperature, the Gibbs free energy of the liquid phase becomes lower than that of the solid phases, driving the phase transition from solid to liquid. Such thermodynamic transitions are crucial for understanding high-temperature processing of Co–Al–O materials, including sintering and thermal spray deposition, where partial melting or phase segregation may influence microstructure and properties [81, 82].

III.2.3 Manganese-doped alumina

The Al_2O_3–Mn binary system is of considerable importance for understanding the thermodynamic stability, solid–liquid equilibria, and phase transformation mechanisms of manganese-doped alumina materials synthesized via the sol–gel route. Manganese incorporation into the alumina matrix has been shown to modify the crystallization pathway, enhance optical and catalytic properties, and influence thermal stability through the formation of mixed oxides such as $MnAl_2O_4$ spinel. From a thermodynamic perspective, this system exhibits a complex succession of solid–state reactions and invariant equilibria, determined by the relative stabilities of α- and γ-alumina, manganese oxides (Mn_3O_4, MnO), and intermetallic or spinel phases such as Al_8Mn_5 and $MnAl_2O_4$.

Consequently, examining the phase diagram, Gibbs energy curves, and temperature-dependent phase fractions provides crucial insight into the stability domains of these phases and their transformation mechanisms during synthesis and heat treatment [83].

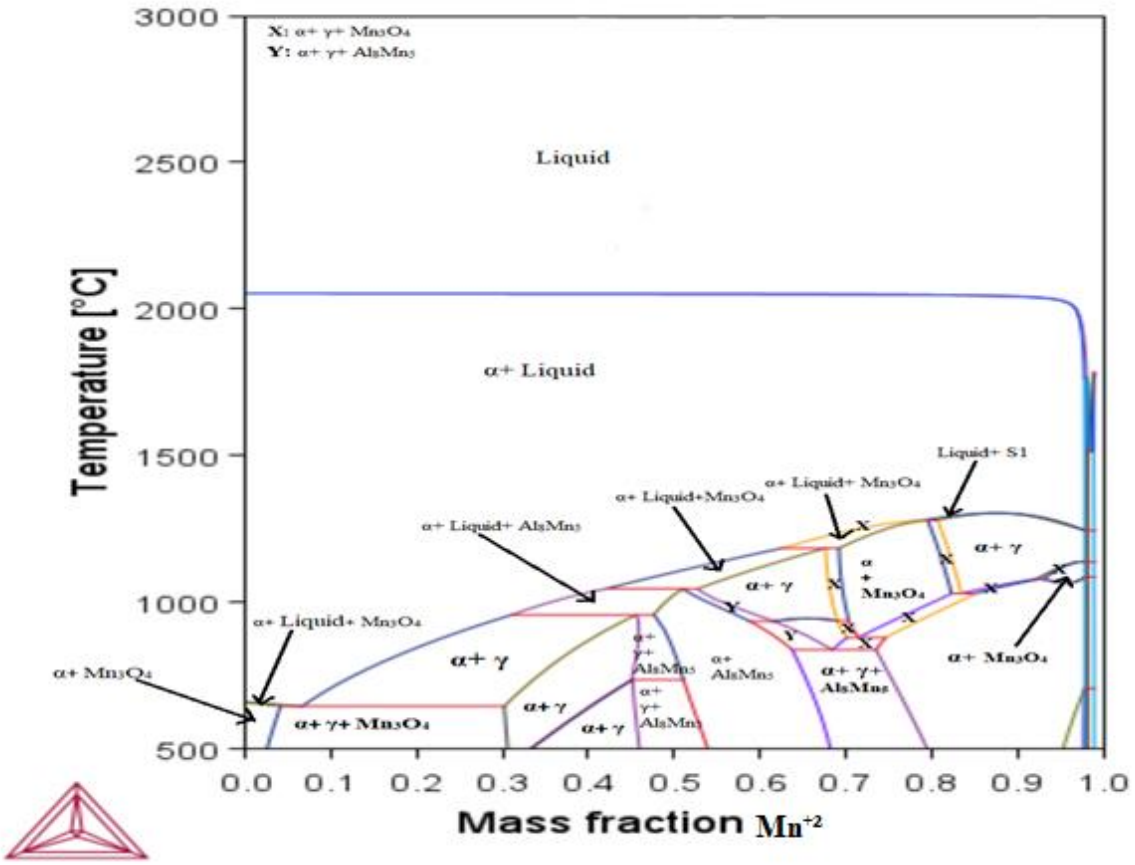

Figure III.10 Binary phase diagram of Al_2O_3-Mn^{+2}.

Figure III.10 presents the binary phase diagram of the Al_2O_3–Mn^{+2} system. At very high temperatures, the mixture remains liquid, with solidification commencing below approximately 2000 K.

At low manganese contents (< 10 %), the system comprises two solid phases: α-Al_2O_3 and Mn_3O_4, indicating limited solubility of Mn^{+2} in the corundum structure. For intermediate compositions (10–30 % Mn^{2+}), three solid phases coexist — α-Al_2O_3, γ-Al_2O_3, and Mn_3O_4 — reflecting partial substitution of Al^{3+} by Mn^{+2} in both alumina polymorphs and the thermodynamic coexistence of corundum, transition alumina, and manganese oxide.

In the 30–80 % Al range, the diagram shows α- and γ-alumina along with the intermetallic compound Al_8Mn_5, which indicates that at these intermediate compositions, metallic interactions become significant and manganese begins to form ordered metallic substructures with aluminum.

At very high aluminum contents (> 80 %), the system again stabilizes into a two-phase domain of α-Al_2O_3 and Mn_3O_4, marking a return to oxide-dominated equilibria. (These equilibria highlight the limited mutual solubility between MnO_x and Al_2O_3 phases and demonstrate the thermodynamic propensity of manganese to segregate into oxide or metallic phases rather than form extended solid solutions in corundum.) [83, 84]

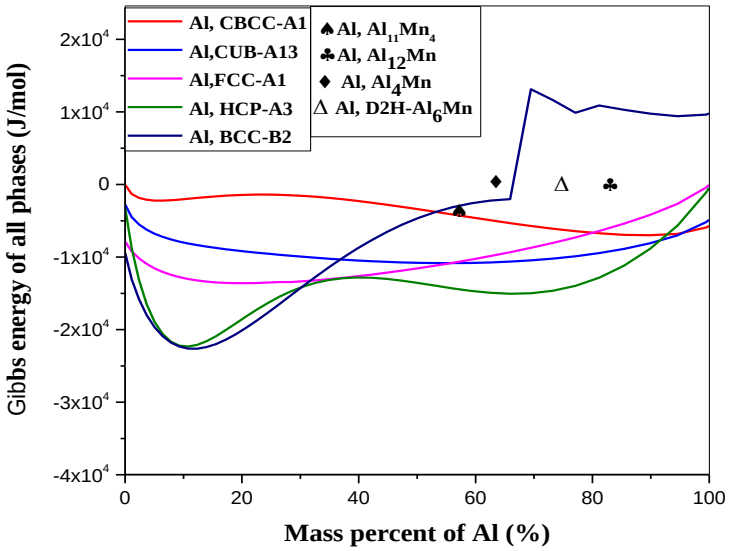

Figure III.11 Gibbs energy of Al-Mn system.

Figure III.11 illustrates the variation of Gibbs free energy (G) as a function of aluminum mass fraction for the different phase states in the binary Al–Mn system. At low aluminum contents (< 30 %), the body-centred cubic (BCC) Mn phase exhibits the lowest Gibbs energy, confirming its status as the most thermodynamically stable phase in the Mn-rich region.

Between 30 % and 90 % Al, the hexagonal close-packed (HCP) aluminum phase becomes dominant, possessing the lowest Gibbs energy in this intermediate range. At very high aluminum contents (> 90 %), the cubic-body-centred (CBCC) aluminum phase shows the lowest Gibbs energy, establishing it as the most stable structure at aluminum-rich compositions.

(The sequential stabilization of BCC, HCP, and CBCC structures reflects the progressive transition from Mn-dominated metallic bonding to Al-rich ordering, in accordance with the reduction of Gibbs energy via alloy formation and electron redistribution between the transition metal and main-group elements.)[83]

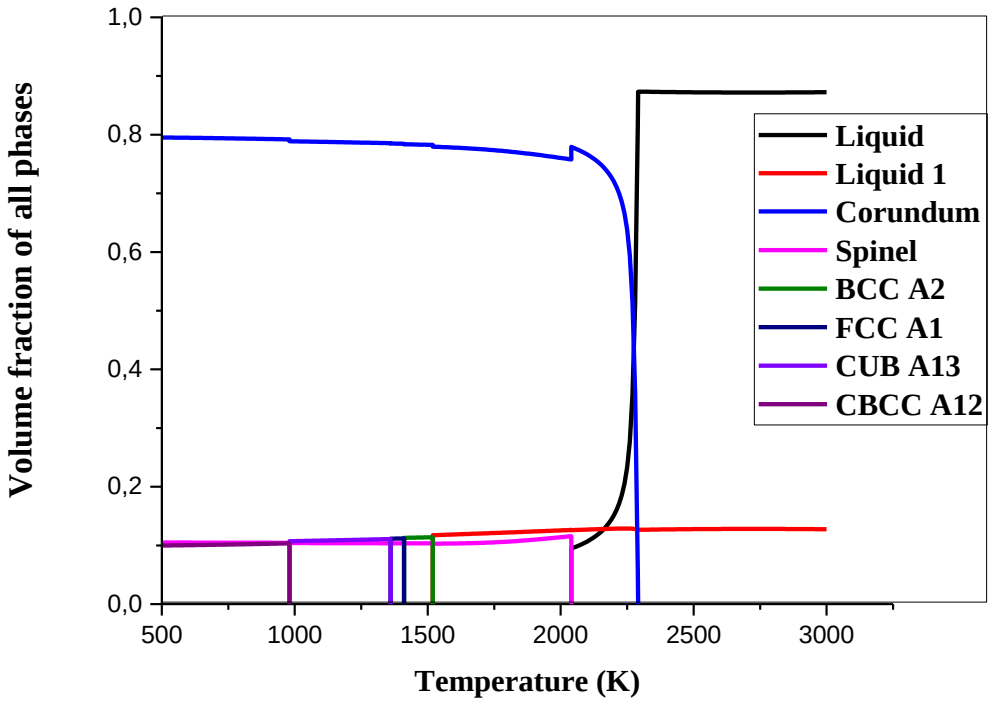

Figure III.12 Volume fraction of all phases in the Al-Mn system.

Figure III.12 depicts the temperature-dependent evolution of phase volume fractions for the Al–Mn system.

At temperatures below 1000 K, the system contains three coexisting solid phases: α-Al_2O_3 (corundum), a spinel phase (likely $MnAl_2O_4$), and a body-centred cubic (BCC) Mn phase. Upon heating to around 1000 K, the BCC phase transforms into a simple cubic phase, which remains stable until approximately 1300 K before converting into a face-centred cubic (FCC) structure.

At ~1400 K, the FCC phase disappears, giving rise again to a simple cubic phase, which persists up to ~1500 K, the approximate onset of manganese melting. This sequence of transformations represents the successive allotropic transitions of metallic manganese — BCC → simple cubic → FCC → simple cubic — as temperature increases. Beyond 2000 K, the volume fractions of corundum and spinel phases decrease sharply, marking the melting of manganese oxide and alumina, and the continuous rise of the liquid fraction indicates complete liquefaction at very high temperatures.

(These transitions reflect the strong temperature dependence of the Gibbs energies of metallic and oxide phases, where thermal excitation progressively destabilises ordered lattices in favour of disordered liquid structures.)[85]

III.3 Fourier transform infrared (FTIR) spectroscopy Analysis

II.3.1 Pure alumina

Fourier transform infrared spectroscopy analysis results obtained for the pure alumina are depicted in **Figure III. 13**

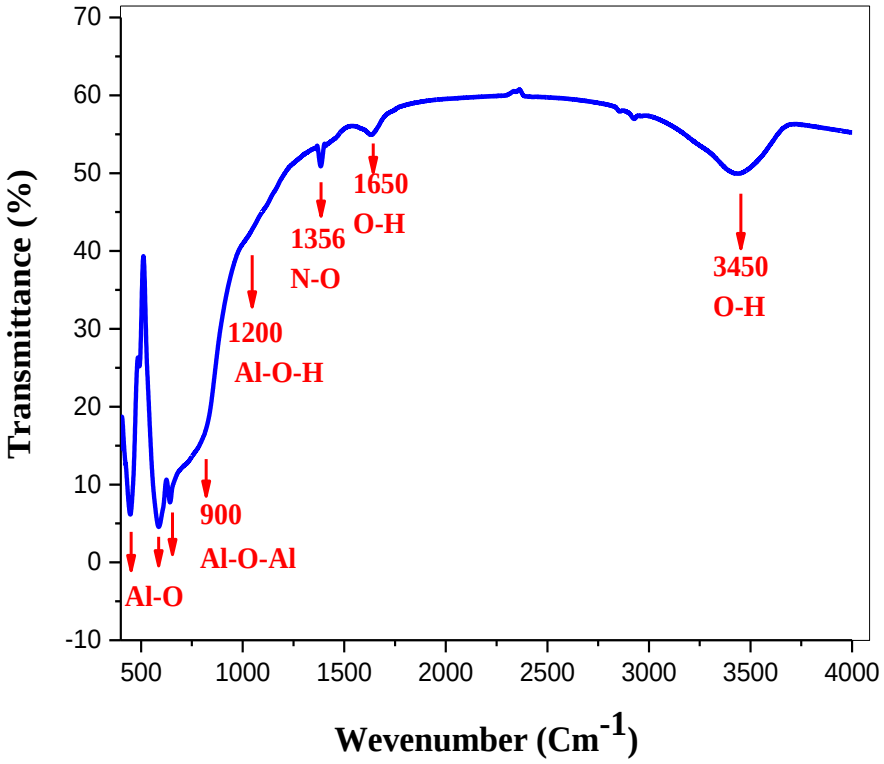

Figure III. 13 Fourier transform infrared (FTIR) spectroscopy Analysis of Al_2O_3.

FTIR analysis results revealed the presence of:

-The bands near 3450 cm^{-1} and 1650 cm^{-1} are attributed to the vibration of the O-H bond [86], which indicates the presence of the hydroxyl ion (OH) in the powders.

-A peak at 1356 cm^{-1} attributed to the nitrate ions.

-A peak around 900 cm^{-1} corresponds to the elongation vibration of Al-O-Al

-Another peak around 1200 cm^{-1} could be the fingerprint of Al-O-H.

-Three peaks between 450 and 700 cm^{-1} is attributed to the vibration of Al-O [87]

III.3.2 Cobalt doped-alumina

Fourier transform infrared spectroscopy analysis results obtained for the cobalt-doped alumina are depicted in **Figure III.14**

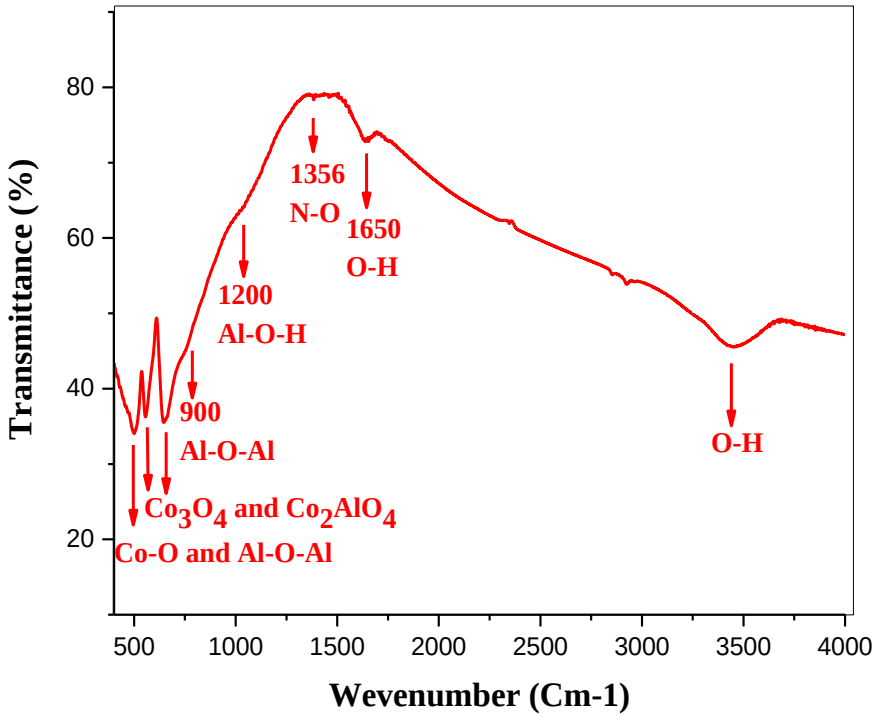

Figure III.14 Fourier transform infrared (FTIR) spectroscopy Analysis of cobalt-doped alumina.

FTIR analysis results revealed the presence of:

-The bands near 3450 cm^{-1} and 1650 cm^{-1} are attributed to the vibration of the O-H bond [86], which indicates the presence of the hydroxyl ion (OH) in the powders.

-A peak at 1356 cm^{-1} attributed to the nitrate ions.

-A peak around 900 cm^{-1} corresponds to the elongation vibration of Al-O-Al

-Another peak around 1200 cm^{-1} could be the fingerprint of Al-O-H.

- Three peaks between 500 and 700 cm^{-1} which corresponds to the vibration of Co-O and the dominance of Co_3O_4 and Co_2AlO_4 [88-90].

III.3.3 Manganese doped-alumina

Fourier transform infrared spectroscopy analysis results obtained for the manganese-doped alumina are depicted in **Figure III.15**

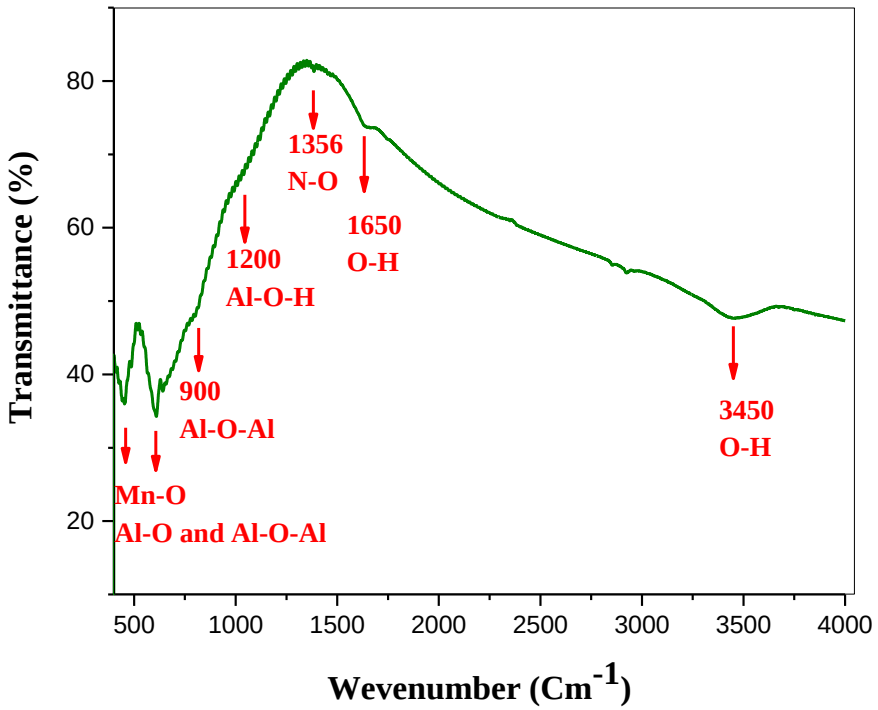

Figure III.15 Fourier transform infrared (FTIR) spectroscopy Analysis of manganese-doped alumina.

-The bands near 3450 cm^{-1} and 1650 cm^{-1} are attributed to the vibration of the O-H bond [86], which indicates the presence of the hydroxyl ion (OH) in the powders.

-A peak at 1356 cm^{-1} attributed to the nitrate ions.

-A peak around 900 cm^{-1} corresponds to the elongation vibration of Al-O-Al

-Another peak around 1200 cm^{-1} could be the fingerprint of Al-O-H.

- Two peaks between 450 and 650 cm-1 corresponds to the vibration of Mn-O [91].

III.4 UV-Visible spectroscopy

III.4.1 Pure alumina

UV-Visible spectroscopy analysis results obtained for the pure alumina are depicted in **Figure III.16**

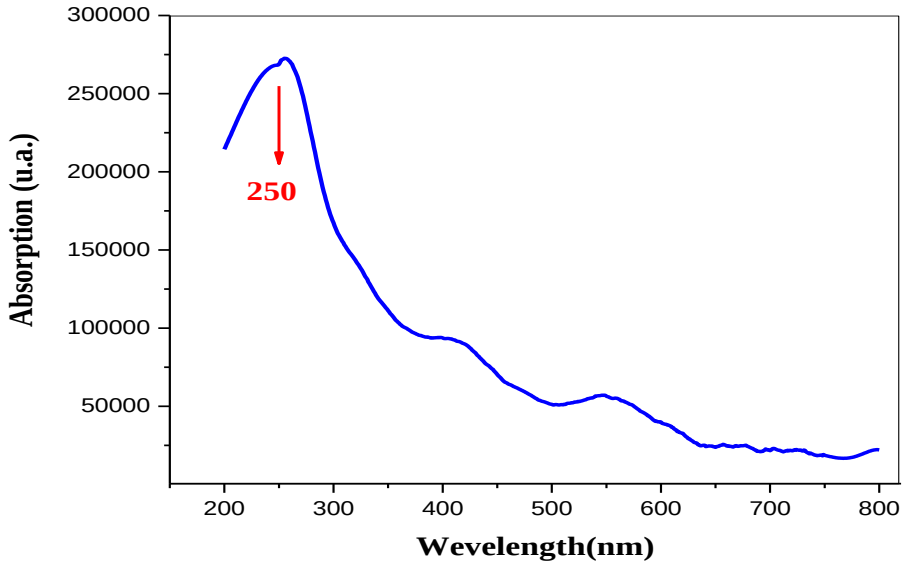

Figure III.16 UV-Vis absorption spectra of Al_2O_3.

We observe the presence of a band in the UV region around 250 nm, This phenomenon can be attributed to the photoexcitation of an electron, initially located in the valence strip, which is transferred to the conduction strip under the effect of the absorption of photons[92, 93].

III.4.2 Cobalt doped-alumina

UV-Visible spectroscopy analysis results obtained for the cobalt-doped alumina are depicted in **Figure III.17**

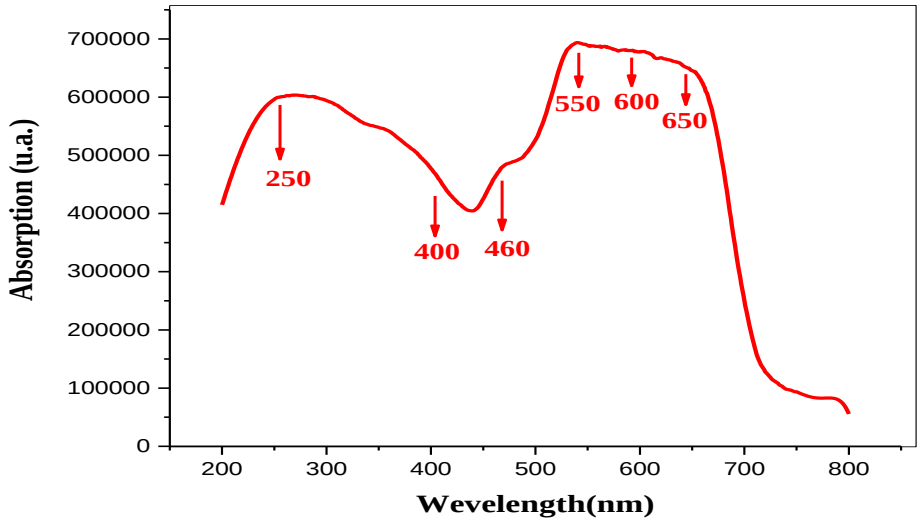

Figure III.17 UV-Vis absorption spectra of cobalt-doped alumina.

The presence of a band in the UV region around 250 nm, and three bands are observed at 550, 600 and 650 nm, attributed to the presence of Co^{+2}. Another band located around 460 nm confirms the presence of Co_2AlO_4, another band at 400 nm attributed to spinel Co_3O_4 [93-95].

III.4.3 Manganese doped-alumina

UV-Visible spectroscopy analysis results obtained for the manganese-doped alumina are depicted in **Figure III.18**

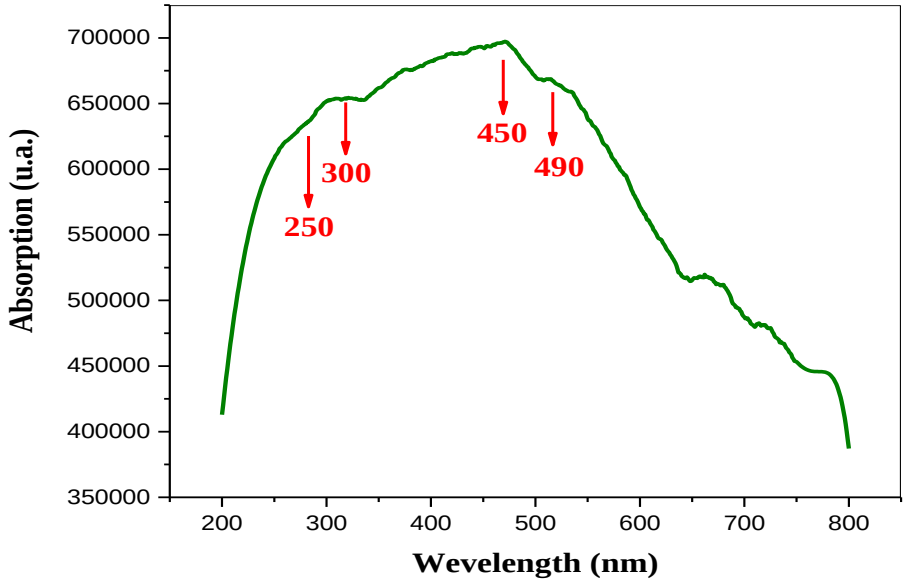

Figure III.18 UV-Vis absorption spectra of manganese-doped alumina.

The presence of a band in the UV region around 250 nm, and another band is observed at 490 nm attributed to the d-d crystal field transition of octahedrally coordinated Mn^{+3} ions in Mn_2O_3, another band at 300 nm is attributed to tetrahedrally coordinated Mn^{+2} ions (typical of Mn_3O_4 spinel). Another band at 450 nm is attributed to Mn^{+4} ions [96].

III.5 Photoluminescence (PL)

III.5.1 Pure alumina

Photoluminescence spectroscopy analysis results obtained for the Pure alumina are depicted in Figure III.19

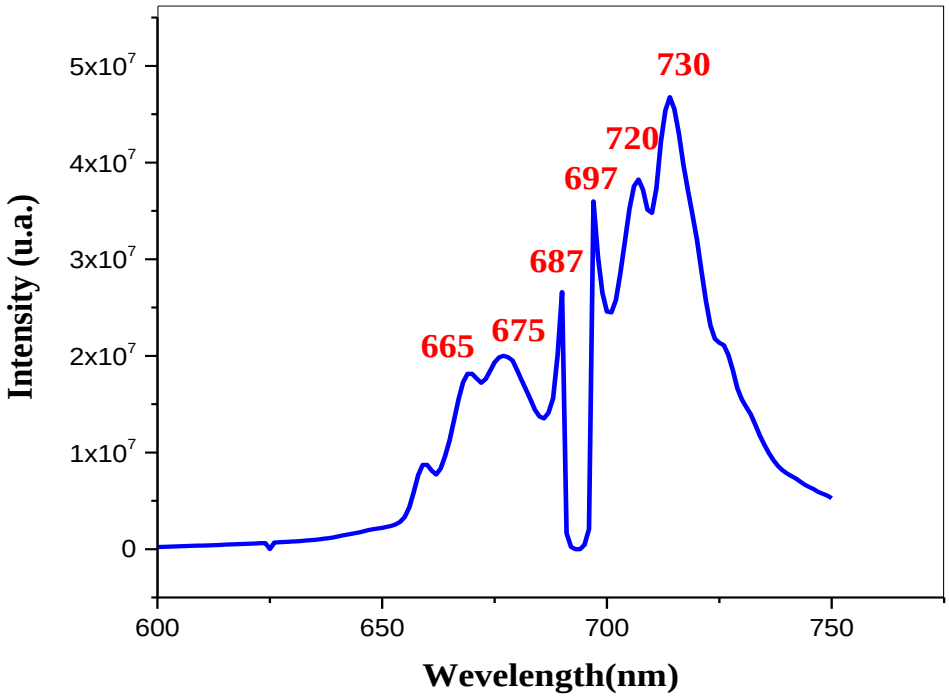

Figure III. 19 Photoluminescence spectrum of Al_2O_3.

The photoluminescence spectrum showed us two peaks at 687 and 697 nm, attributed essentially to the alpha-alumina phase caused by oxygen vacancies and calcination at a very high temperature of 1200 °C.

Other peaks at 720 and 730 nm can be attributed to uncontrollable impurities, which can be incorporated into the alumina network, and other less intense peaks at 665 and 675 nm [97, 98].

III.5.2 Cobalt doped-alumina

Photoluminescence spectroscopy analysis results obtained for the cobalt-doped alumina are depicted in Figure III.20

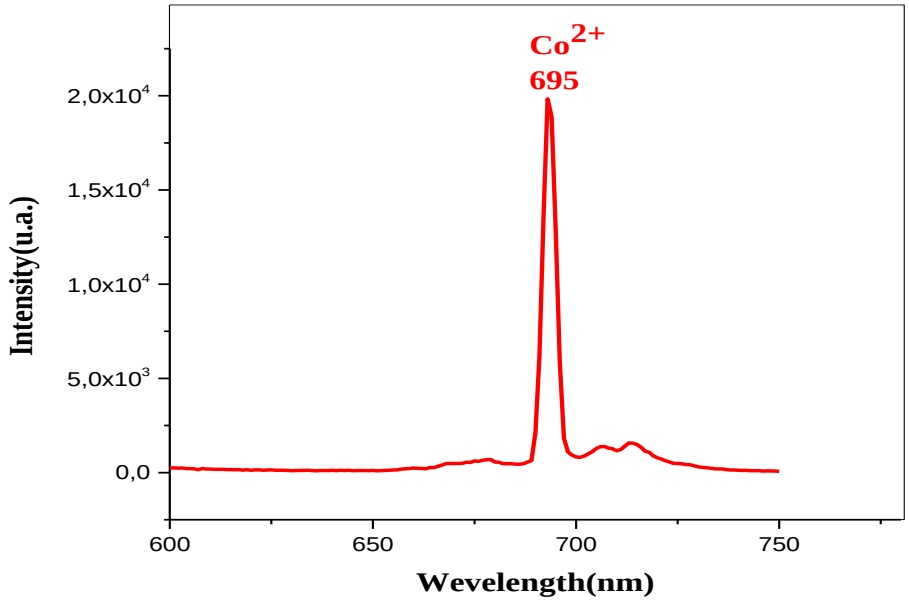

Figure III.20 Photoluminescence spectrum of cobalt-doped alumina.

The photoluminescence spectrum showed us a very intense peak around 695 attributed to the allowed electronic transition of Co^{2+} ions, which go from a fundamental level to an excited level, by emission of photon [99].

III.5.3 Manganese doped-alumina

Photoluminescence spectroscopy analysis results obtained for the cobalt-doped alumina are depicted in Figure III.21

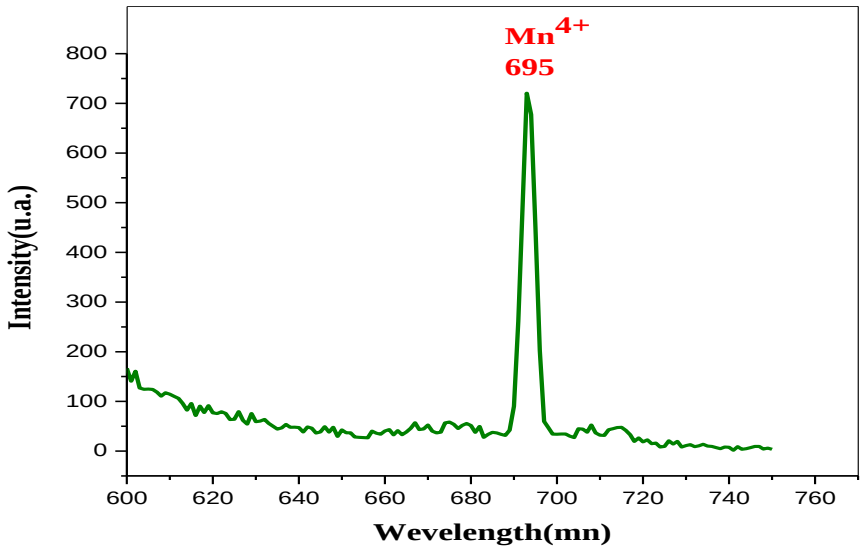

Figure III.21 Photoluminescence spectrum of manganese-doped alumina.

The photoluminescence spectrum showed us An intense peak around 695 nm corresponds to the electronic transition of Mn^{4+} ions, which goes from a fundamental level to an excited level under emission of a photon [100].

III.6 XRD Analysis

III.6.1 Pure alumina

The XRD results obtained for the pure alumina are shown in **figure III.22**

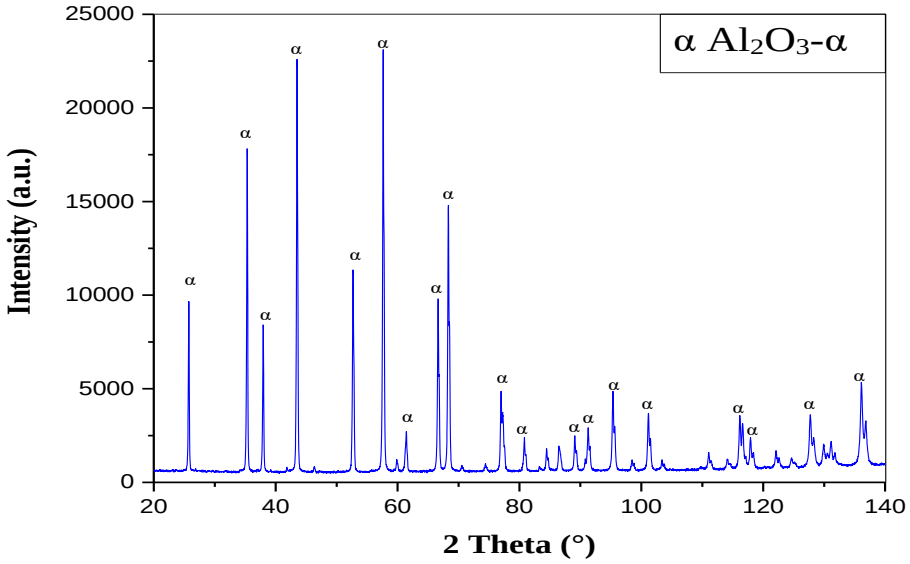

Figure III. 22 X-ray diffraction spectra of Al_2O_3.

The presence of a single α-Al_2O_3 phase with high crystallinity, which crystallizes in a rhombohedral system and space group R-3C, with a crystallite size of 42.34 nm, is noted. The presence of a single alpha phase is due to the calcination of the final product at 1200°C, since the phase appears from 1000°C [101- 103].

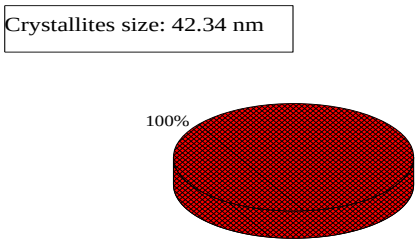

Figure III. 23 Quantification and crystallites size of Al_2O_3

III.6.2 Cobalt doped-alumina

The XRD results obtained for the cobalt-doped alumina are shown in **figure III.24**

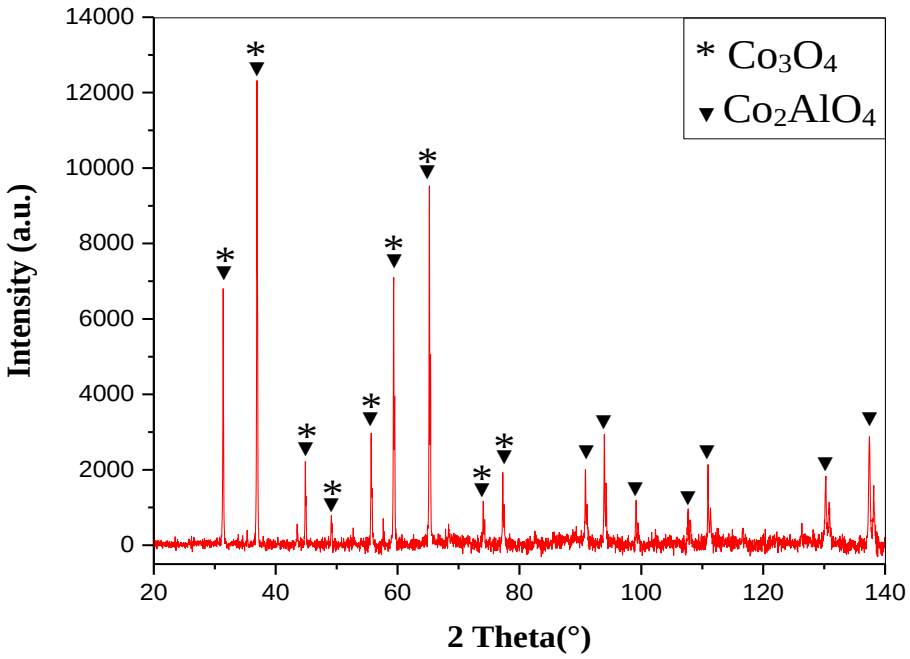

Figure III.24 X-ray diffraction spectra of cobalt-doped alumina.

The XRD spectrum reveals the presence of two spinel phases: Co_2AlO_4 with a percentage of 62% and Co_3O_4 with a percentage of 38%, which crystallize in a cubic system and a space group Fd-3m. The peaks corresponding to Co_3O_4 and Co_2AlO_4 are difficult to differentiate from each other using XRD spectra due to their significant peak overlap, and calcination at high temperatures above 1000°C promotes the appearance of the Co_2AlO_4 spinel structure. [104, 105]. The formation of the porous structure of Co_3O_4 is due to exhaust gases, which come from the precursor cobalt nitrate [24].

The crystallite size of 48.33 nm is wide; this increase in crystallite size is due to calcination at high temperature (1200°C) and cobalt, which promotes grain growth and the formation of new crystals (Co_3O_4 and Co_2AlO_4) [20].

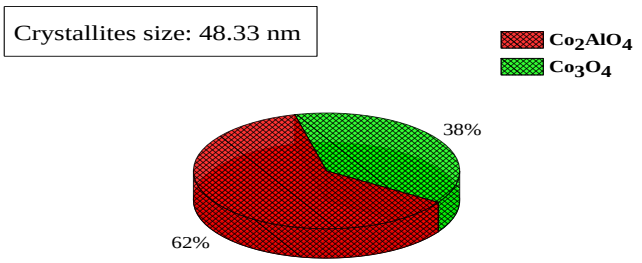

Figure III. 25 Quantification and crystallites size of cobalt-doped alumina.

III.6.3 Manganese doped-alumina

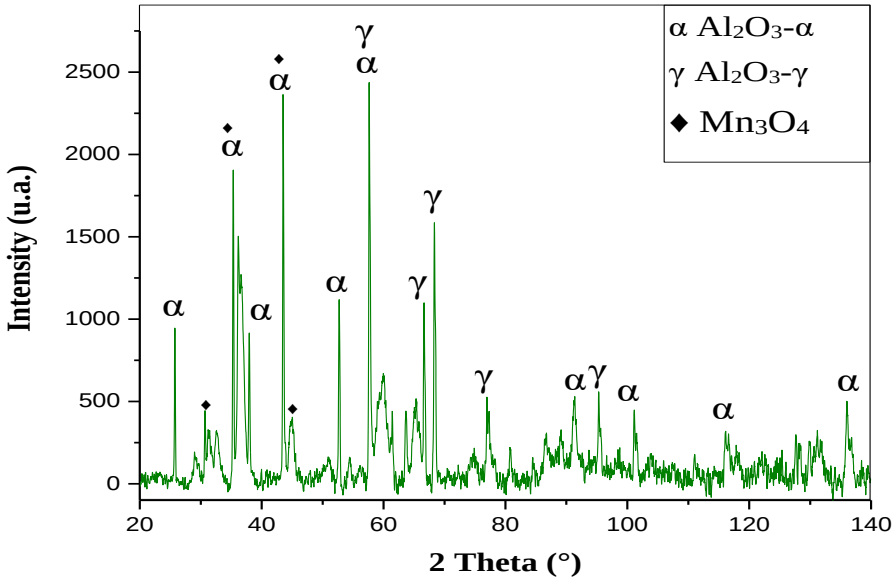

Figure III.26 X-ray diffraction spectra of manganese-doped alumina.

The XRD results obtained for the manganese-doped alumina are shown in **figure III.26**

The XRD spectrum reveals the presence of the α-Al_2O_3 phase as a matrix with a percentage of 81%, a Mn_3O_4 spinel structure, which crystallizes in a tetragonal system and space group I41/amd in second position with a percentage of 15%, and some traces of the γ-Al_2O_3 phase. Previous research carried out on alumina doped with manganese has always noted the presence of the α-Al_2O_3 phase, which is due to the presence of manganese, promoting the appearance of this phase even at a temperature below 1000°C. [104, 106].

The 24 nm crystallite size is very small; therefore, manganese promotes a finer and more homogeneous structure [104].

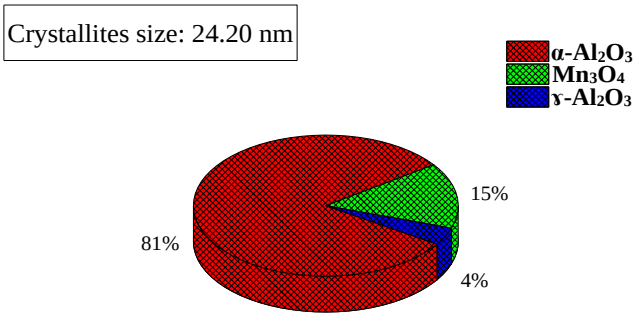

Figure III. 27 Quantification and crystallites size of manganese-doped alumina.

III.7 Microstructure morphology

III.7.1 Optical and distribution of particles size

III.7.1.1 Pure alumina

Figure III.28 represents optical images of Al_2O_3 powder. The images represents the morphology of powder on the image with defects and microstructure (cracks, lines, etc.).

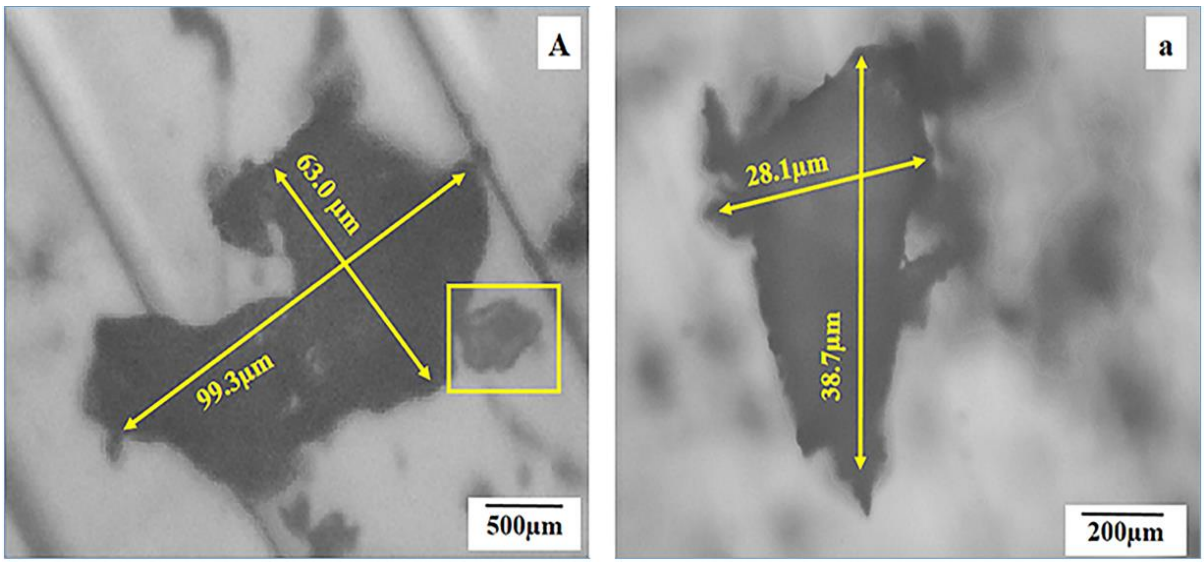

Figure III.28 Optical microscopy image of Al_2O_3

The optical micrograph of alumina (Al_2O_3) powder shown in Figure III.28.A and III.28.a reveals critical aspects of its microstructure, including grain size, shape, and distribution. Typically, alumina particles exhibit irregular shapes, with grain size and morphology playing a significant role in determining the material's mechanical properties [107]. A uniform distribution of particles across the micrograph indicates good powder homogeneity, Khan et al found that the amount of aluminum nitrate in the reaction mixture plays an important role in particle size and uniformity. The lower concentration of aluminum produced larger irregular spheres [108].

The micrograph can also highlight no porosity, which affects the material's density, and reveal some inclusions onto agglomeration that may compromise the purity of the alumina. The arrangement of the particles and their contact points are important indicators of the potential for sintering the powder, the finest particles tend to agglomerate [109, 110].

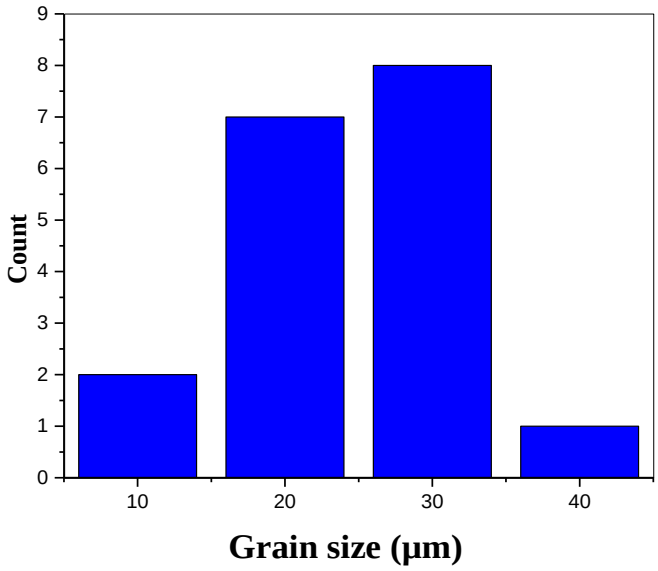

Figure III.29 Particle size distribution of Al_2O_3.

III.7.1.2 Cobalt-doped alumina

Figure III.30 represents optical images of cobalt-doped alumina powder. The images represents the morphology of powder on the image with defects and microstructure (cracks, lines, etc.).

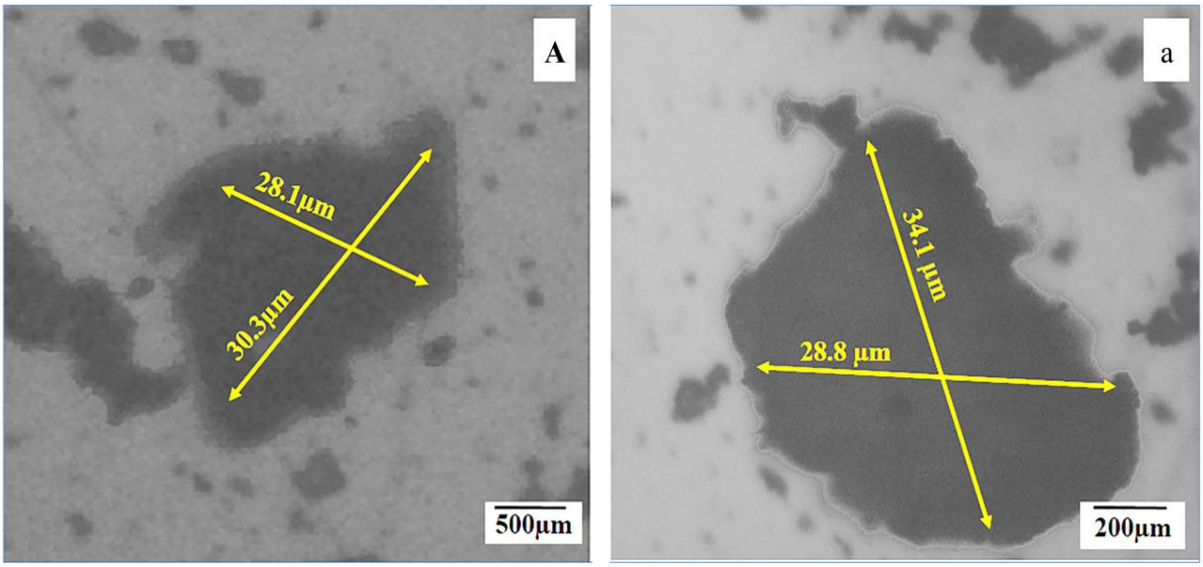

Figure III.30 Optical microscopy image of cobalt-doped alumina.

We notice an enlargement of the grains with absence of agglomeration [111] observed in figure III.30.A and III.30.a; ElJabbar et al [112] found that the synthesis of alumina doped with cobalt with citric acid as a complexing agent and obtained at temperatures above 900 °C promotes grain enlargement and powder densification. Parveen et al [21] found that incorporation of cobalt into alumina improves densification and promotes grain growth.

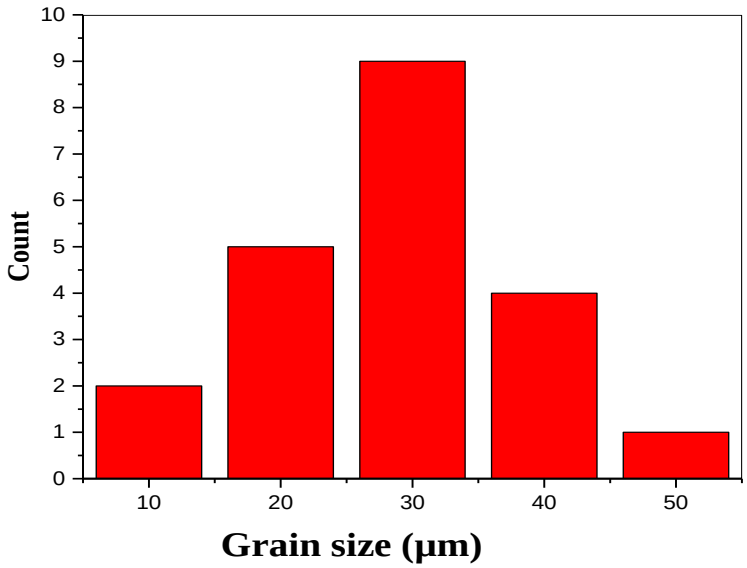

Figure III.31 Particle size distribution of cobalt-doped alumina.

III.7.1.3 Manganese-doped alumina

Figure III.32 represents optical images of manganese-doped alumina powder. The images represents the morphology of powder on the image with defects and microstructure (cracks, lines, etc.).

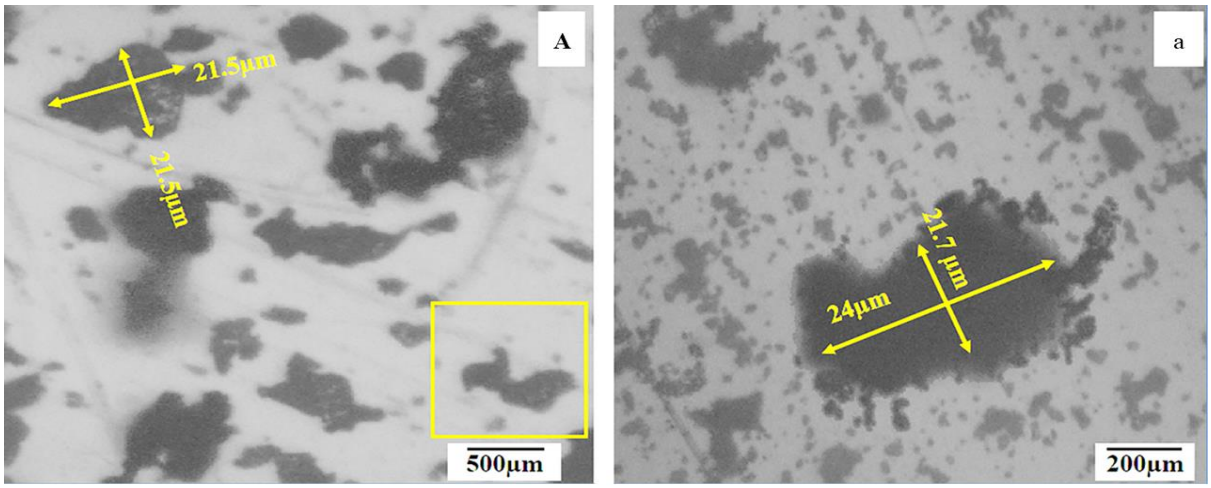

Figure III.32 Optical microscopy image of manganese-doped alumina.

We notice finer particles and more agglomeration are observed in Figures III.32.A and III.32.a, which is confirmed by the histogram presented in Figure III.24. NAGASHIMA et al [113] studied the doping of alumina with MnO and they found that the percentage of the dopant influences the size of the grains; more dopant favors the coarsening of the grains, and doping at lower percentages leads to finer grains, with strong agglomeration, which gives them good resistance to bending.

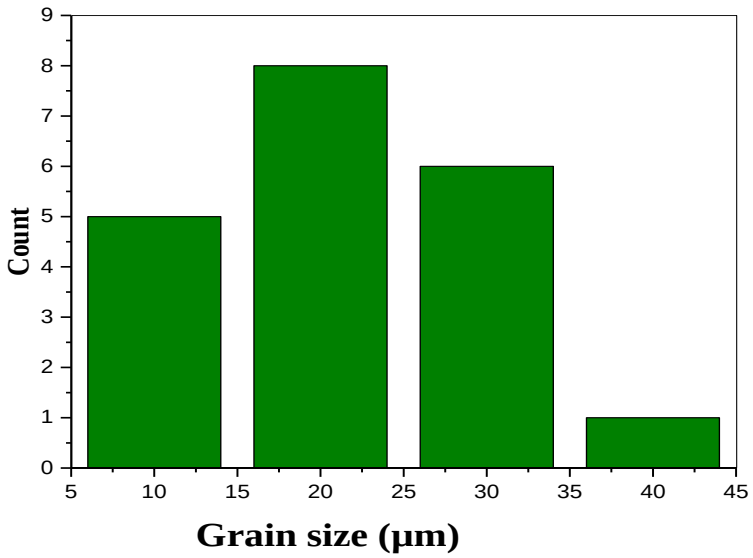

Figure III.33 Particle size distribution of manganese-doped alumina.

III.7.2 SEM analysis

III.7.2.1 Pure alumina

Figure III.34 shows us the SEM micrograph of Al_2O_3 and Figure III.35 shows us the chemical composition of the powder prepared using EDSS energy dispersive spectroscopy connected to the SEM.

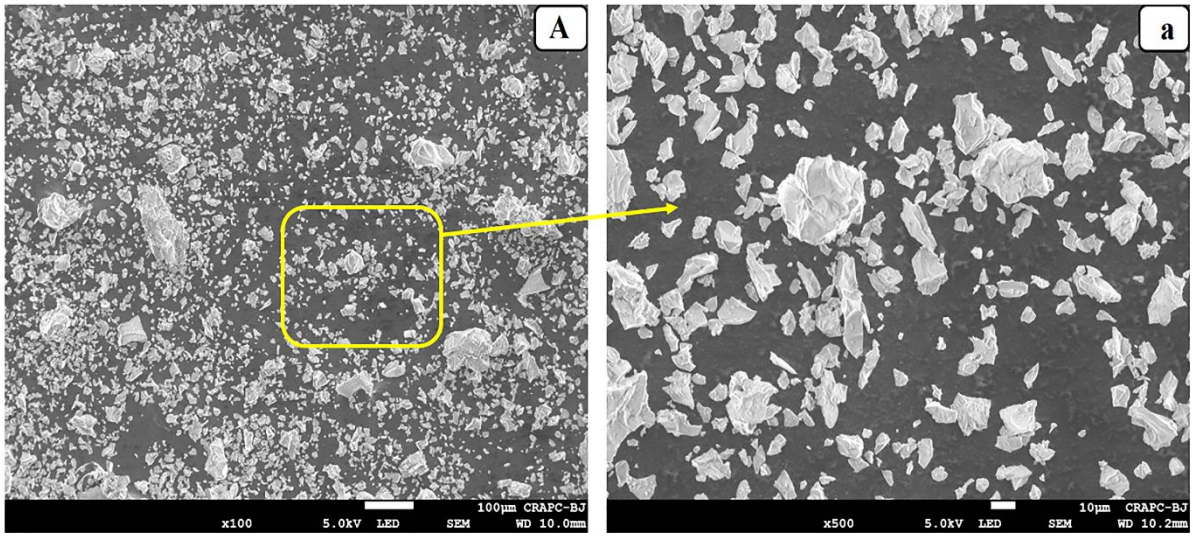

Figure III.34 SEM micrograph of Al_2O_3.

The results showed a homogeneous microstructure with ultrafine grains. Concerning the chemical composition shows us the presence of oxygen and aluminum in the powder, which we prove the high purity of pure alumina powder [114].

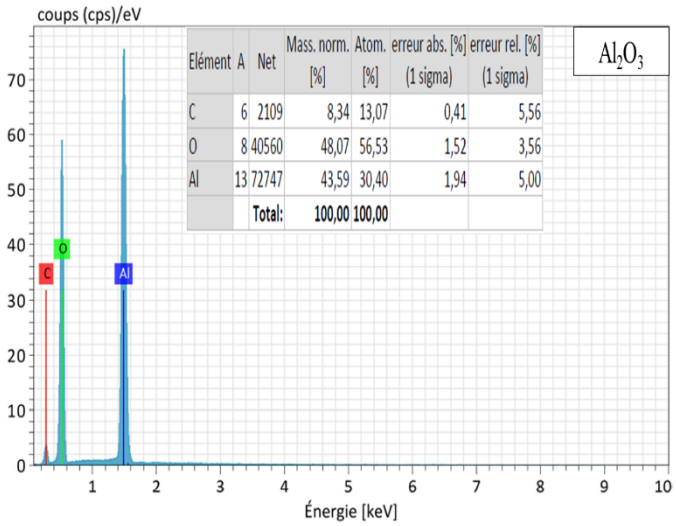

Figure III.35 EDS results of Al_2O_3.

III.7.1.2 Cobalt-doped alumina

Figure III.36 shows us the SEM micrograph of cobalt-doped alumina and Figure III.37 shows us the chemical composition of the powder prepared using EDSS energy dispersive spectroscopy connected to the SEM.

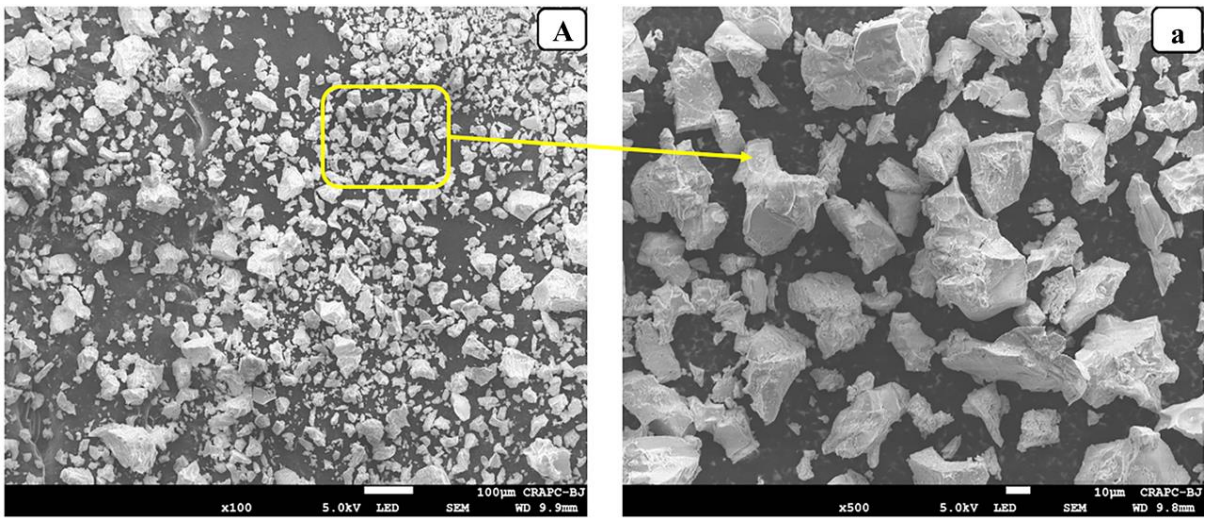

Figure III.36 SEM micrograph of cobalt-doped alumina.

The formation of the $CoAl_2O_4$ phase confirmed by the XRD results involved the growth of the grains; the high temperature and the duration of calcination influence this enlargement. Concerning the chemical composition shows us the presence of oxygen, aluminum and cobalt in the powder [115].

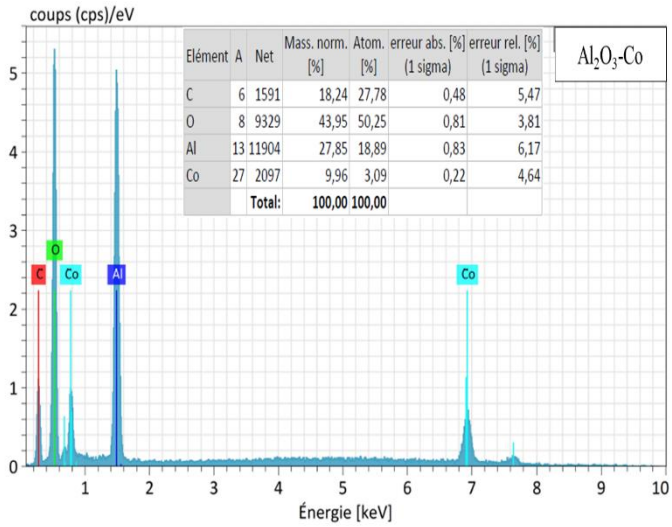

Elément	A	Net	Mass. norm. [%]	Atom. [%]	erreur abs. [%] (1 sigma)	erreur rel. [%] (1 sigma)
C	6	1591	18,24	27,78	0,48	5,47
O	8	9329	43,95	50,25	0,81	3,81
Al	13	11904	27,85	18,89	0,83	6,17
Co	27	2097	9,96	3,09	0,22	4,64
		Total:	100,00	100,00		

Figure III.37 EDS results of cobalt-doped alumina.

III.7.1.3 Manganese-doped alumina

Figure III.38 shows us the SEM micrograph of manganese-doped alumina and Figure III.39 shows us the chemical composition of the powder prepared using EDSS energy dispersive spectroscopy connected to the SEM.

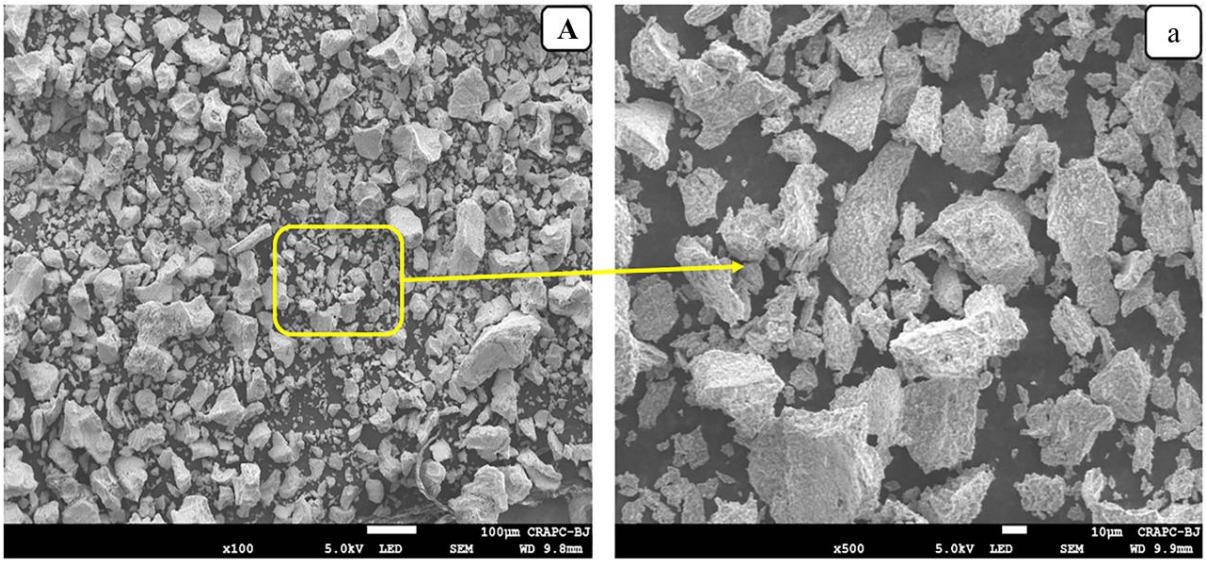

Figure III.38 SEM micrograph of manganese-doped alumina.

We notice a narrow distribution of grain size with the presence of ultrafine grains and other larger ones, which is due to the interaction of two phenomena: manganese doping promotes grain enlargement, and the presence of a second phase inhibits grain growth. Concerning the chemical composition, it shows us the presence of oxygen, aluminum, and manganese in the powder [116].

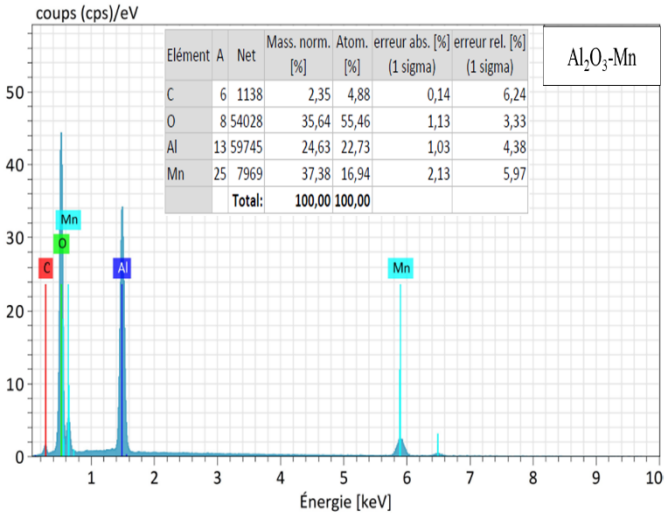

Figure III.39 EDS results of manganese-doped alumina.

General Conclusion

IV General conclusion

The present Phd investigation focused on the synthesis and characterization of alumina-based powders doped with manganese and cobalt using the sol–gel method. The main objective was to look on the influence of these dopants on the structural, morphological, and optical properties of alumina in order to better understand their potential for advanced functional materials.

Three types of powders were synthesized: pure alumina, alumina doped with cobalt, and alumina doped with manganese. Aluminum nitrate, cobalt nitrate, and manganese nitrate were used as precursors, with ethanol as the solvent and citric acid as the complexing agent. A comprehensive set of physicochemical and structural characterization techniques was employed, including DTA/TGA thermal analysis, Fourier Transform Infrared Spectroscopy (FTIR), UV–Visible spectroscopy, photoluminescence (PL) spectroscopy, X-ray diffraction (XRD), and both optical and scanning electron microscopy (SEM).

The main findings can be summarized as follows:

- Thermal Analysis (DTA/TGA):

  The thermogravimetric behavior revealed two distinct mass loss stages between 50–150 °C and 150–220 °C for all powders**,** corresponding respectively to precursor dehydration and decomposition of organic species. A third stage, observed between 250–600 °C for pure and cobalt-doped alumina, was associated with the decomposition of residual organics. Above 600 °C and up to 1200 °C, the absence of significant mass variation indicates the completion of decomposition reactions and the progressive crystallization of alumina.

- **FTIR Spectroscopy:**

  The FTIR spectra of undoped alumina showed characteristic Al–O and Al–O–Al vibration bands corresponding to Al_2O_3. In cobalt-doped samples, additional bands assigned to Co–O confirmed the presence of Co_3O_4 and Co_2AlO_4 spinel phases. For manganese-doped alumina, characteristic Mn–O vibration modes were identified, consistent with Mn_3O_4 formation.

- UV–Visible Spectroscopy:

  All powders exhibited an absorption band around 250 nm, attributed to electronic transitions from the valence to conduction band upon photon absorption. In cobalt-doped alumina, additional absorption bands confirmed the presence of Co^{2+} species (Co_3O_4, Co_2AlO_4), while manganese-doped alumina showed absorption related to Mn^{2+}, Mn^{3+}, and Mn^{4+} ions.

- Photoluminescence Analysis:

  The photoluminescence spectra revealed two emission peaks for undoped alumina, attributed to oxygen vacancies and high-temperature (1200 °C) calcination effects leading to α-Al_2O_3 formation. A characteristic Co^{2+} electronic transition was detected in cobalt-doped alumina, whereas a Mn^{4+} transition peak appeared in manganese-doped alumina.

- X-ray Diffraction analysis (XRD):

  XRD analysis confirmed a single α-Al_2O_3 phase in undoped alumina with an average crystallite size of 42 nm. Cobalt-doped alumina contained two phases (≈62% Co_2AlO_4 and 38% Co_3O_4) with an average crystallite size of 48 nm. Manganese-doped alumina exhibited three phases (≈81% α-Al_2O_3, 15% Mn_3O_4, and 4% γ-Al_2O_3) with finer crystallites of about 24 nm.

- Microstructural and Morphological Analysis:

  Optical and SEM observations revealed a homogeneous distribution of ultrafine particles in undoped alumina. In cobalt-doped samples, grain coarsening was observed due to high-temperature calcination, while agglomeration remained minimal, suggesting good dispersion. Conversely, manganese doping led to finer particle formation accompanied by noticeable agglomeration.

Perspectives and Future Work

The findings of this thesis have confirmed the effectiveness of the sol–gel process for synthesizing high-purity alumina-based powders with controlled doping by cobalt and

manganese. These results open several scientific and technological perspectives for further development and application of such materials.

From a scientific standpoint, future work should focus on optimizing the sol–gel synthesis conditions—particularly precursor concentration, pH regulation, and calcination profile—to achieve precise control over particle size, morphology, and phase composition. Advanced characterization techniques such as Transmission Electron Microscopy (TEM), X-ray Photoelectron Spectroscopy (XPS), and Raman spectroscopy could be employed to better elucidate dopant incorporation mechanisms, defect chemistry, and local bonding environments within the alumina matrix.

A systematic study on the influence of dopant concentration is also recommended to establish correlations between chemical composition, crystallinity, and optical or electronic behavior. Extending the investigation to multiple dopants or co-doping strategies may lead to synergistic effects and new functional phases. In addition, the application of the sol–gel derived powders in thin film form via the dip-coating technique offers a promising direction for producing uniform, adherent coatings with tailored optical or protective properties. Optimization of coating parameters—such as withdrawal speed, viscosity, and thermal post-treatment—will be essential to ensure film homogeneity and mechanical integrity.

From a mechanical engineering perspective, it would be highly valuable to assess the mechanical properties of both the powders and the dip-coated layers. Detailed studies on hardness, elastic modulus, fracture toughness, and wear resistance could provide crucial insights into the effect of dopants and microstructure on the mechanical behavior of alumina. Furthermore, evaluating the thermal shock resistance and adhesion strength of the coated layers would help identify their suitability for high-temperature or tribological applications.

In terms of technological applications, the modified optical and luminescent behavior of the doped alumina suggests potential for use in optoelectronic components, photonic coatings, and thermally stable pigments. Moreover, integrating the sol–gel and dip-coating processes with advanced deposition or additive manufacturing techniques could enable the fabrication of graded or multifunctional surfaces for sensors, thermal barriers, or catalytic systems.

Finally, future studies should consider the scale-up and reproducibility of the sol–gel and dip-coating methods, ensuring consistent material quality and cost-effective production for industrial use. This would facilitate the transition from laboratory-scale synthesis to real-world applications, consolidating the scientific and technological value of doped alumina-based systems developed in this work.

Bibliographic references

V. Bibliographic references

[1] Abolhassan NAJAFI, Fahimeh SHARIFI, Saloumeh MESGARI-ABBASI, Gholamreza KHALAJ (2022), Influence of pH and temperature parameters on the sol-gel synthesis process of meso porous ZrC nanopowder, Ceramics International, https://doi.org/10.1016/j.ceramint.2022.05.367.

[2] Donghui GUO, Feifei ZHOU, Baosheng XU, Yiguang WANG, You WANG (2022) Synthesis and characterization of high-entropy (La0.2Nd0.2Sm0.2Gd0.2Yb0.2)2(Zr0.75Ce0.25)2O7 nanopowders, Ceramics International, https://doi.org/10.1016/j.ceramint.2022.07.207.

[3] Qiaoyang SUN, Tao LIU, Tianpeng WEN, Jingkun YU (2022) Optimization of particle size, dispersity, and conductivity of 8 mol% Y_2O_3 doped tetragonal zirconia polycrystalline nanopowder prepared by modified sol-gel method via activated carbon absorption. The European Ceramic Society. https://doi.org/10.1016/j.jeurceramsoc.2022.06.017.2022.

[4] Jui-Ting LIANG, Shao-Fu CHANG, Cheng-Han WU, Shih-Hsun CHEN, Che-Wei TSAI, Kuei-Chung CHENG, Kim HSU (2023) Influence of Feedstock in the Formation Mechanism of Cold-Sprayed Copper Coatings. Coatings. https://doi.org/10.3390/coatings13061065.

[5] Venkata NAGA Vamsi MUNAGALA, Valary AKINYI, Phuong VO, Richard R. CHROMIK (2018) Influence of Powder Morphology and Microstructure on the Cold Spray and Mechanical Properties of Ti6Al4V Coatings. Therm Spray Tech. https://doi.org/10.1007/s11666-018-0729-8.

[6] John HENAO, Fabio VARGAS, Astrid L. GIRALDO-BETANCUR, Jorge corona-castuera, Oscar SOTELO-MAZÓN (2021) Principles and Applications of Thermal Spray Coatings. Advanced Surface Coating Techniques for Modern Industrial Applications. https://doi.org/ 10.4018/978-1-7998-4870-7.ch002.

[7] Fatah HADJI, Rassim YOUNES, Mohand Amokrane BRADAI, Nedjemeddine BOUNAR, Mikhail ALYMOV (2025) Structural Analysis and Application in Dip Coating of Alumina Powder. Moscow University Chemistry Bulletin, https://doi.org/10.3103/S0027131424700536.

[8] Fatah HADJI, Rassim YOUNES, D. BELFENNACHE, R. YEKHLEF, Nedjemeddine BOUNAR, Mohand Amokrane BRADAI, Mohamed HEMDAN, Mohamed A. ALI (2025) Non-Isothermal Kinetics of Coats-Red Fern in the Critical Points: Formation of$Al_{2-x}Cr_xO_3$(x = 0.02) powders obtained by Sol-Gel Method. Egyptian Journal of Chemistry. DOI: 10.21608/EJCHEM.2024.283147.9600.

[9] Pallavi Suhasinee BEHERA, Sunipa BHATTACHARYYA (2021) Thermal decomposition, phase evolution and morphology study of combustion synthesized alumina powder – Influence of precursor Ph. Materials Chemistry and Physics. https://doi.org/10.1016/j.matchemphys.2020.124030.

[10] Alafara A. BABA, Veronica Y. OLOWO, Mustapha A. RAJI, Julius P. AKINRIBIDO (2020) Preparation of Industrial α-Alumina Powder from Ijero Ekiti (Nigeria) Kaolin ore by Acid Leaching Process. Chemistry Africa. https://doi.org/10.1007/s42250-020-00159-y.

[11] Katarina DRDLIKOVA, Daniel DRDLIK, Hynek HADRABA, Robert KLEMENT, Karel MACA (2020) Optical and mechanical properties of mn-doped transparent alumina and their comparison with

selected rare earth and transient metal-doped aluminas. The European Ceramic Society. https://doi.org/10.1016/j.jeurceramsoc.2020.01.041.

[12] S.V. ZVONAREV, V.Y. CHURKIN, V.A. PANKOV, A.V. ABRAMOV, S.V. NIKIFOROV (2020) The influence of synthesis modes of alumina ceramics doped with manganese on sensitivity to ionizing radiation. Radiation Measurements. https://doi.org/10.1016/j.radmeas.2020.106410.

[13] Nasr-Allah M. DERAZ (2008): Physicochemical, Surface, and Catalytic Properties of Pure and Ceria-Doped Manganese/Alumina Catalysts. Chinese journal of catalysis. https://doi.org/10.1016/S1872-2067(08)60066-2.

[14] S.B. DHUBAN, S. RAMESH, C.Y. Tan, Y.H. Wong, U. Johnson Alengaram, S. Ramesh, W.D. Teng, F. Tarlochan, U. Sutharsini (2019) Sintering behaviour and properties of manganese-doped alumina. Ceramics International. https://doi.org/10.1016/j.ceramint.2018.12.207.

[15] Ioana MINDRU, Dana GINGASU, Luminita PATRON, Adelina IANCULESCU, Vasile-Adrian SURDU, Daniela C. CULITA, Silviu PREDA, Constantin-Daniel NEGUT, Ovidiu OPREA (2019) A new approach: Synthesis of cobalt aluminate nanoparticles using tamarind fruit extract. Materials Science & Engineering. https://doi.org/10.1016/j.mseb.2019.05.031.

[16] C. RAGUPATHI, J. Judith VIJAYA, L. John KENNEDY, M. BOUOUDINA (2014) Combustion synthesis, structure, magnetic and optical properties of cobalt aluminate spinel nanocrystals. Ceramics International. http://dx.doi.org/10.1016/j.ceramint.2014.05.003.

[17] Yongping MA, Muling ZENG, Jiao HE, Lina DUAN, Jianfei WANG, Junjie LI, Jiaqiang WANG (2011) Syntheses and characterizations of cobalt doped mesoporous alumina prepared using natural rubber latex as template and its catalytic oxidation of tetralin to tetralone. Applied Catalysis A : General. doi:10.1016/j.apcata.2011.02.001.

[18] M. CRISAN, M. RILEANU, S. PREDA, M. ZAHARESCU, A. M. VALEAN, E. J. POPOVICI,V.S. TEODORESCU, V. MATEJEC, J. MRAZEK, Manganese Doped Sol-Gel Materials With Catalytic Properties (2006), Optoelectronics And Advanced Materials.

[19] E. Lopez-NAVARRETE, A. CABALLERO, A.R. Gonzalez-ELIPE, M. OCANA, Chemical State And Distribution Of Mn Ions In Mn-Doped A-Al_2O_3 Solid Solutions Prepared In The Absence And The Presence Of Fluxes (2004) the European Ceramic Society, doi:10.1016/j.jeurceramsoc.2003.11.018.

[20] Sanja MARINOVIC´ T, MUDRINIĆ B, DOJˇCINOVIC´ T, BARUDˇZIJA P, BANKOVIC´ T NOVAKOVIC (2021) Cobalt-doped alumina catalysts in catalytic oxidation of tartrazine induced by Oxone®. J Environ Chem Eng.https://doi.org/10.1016/j.jece.2021.106348.

[21] Kousar PARVEEN, Uzaira RAFIQUE (2018) Development of cobalt-doped alumina hybrids for adsorption of textile effluents. Adsorption Science & Technology. doi: 10.1177/0263617416687563.

[22] S. RAMACHANDRAN, Chandra SEKHAR DASH, A. THAMILSELVAN, S. KALPANA, M. SUNDARARAJAN (2020) Rapid Synthesis and Characterization of Pure and Cobalt Doped Zinc Aluminate Nanoparticles via Microwave Assisted Combustion Method. Nanoscience and Nanotechnology. doi:10.1166/jnn.2020.17314.

[23] Minori TAGUCHI, Takayuki NAKANE, Kenjiro HASHI, Shinobu OHKI, Tadashi SHIMIZU, Yoshio SAKKA, Akiyuki MATSUSHITA, Hiroya ABE, Toshitaka FUNAZUKURI, Takashi NAKA (2012) Reaction temperature variations on the crystallographic state of spinel cobalt aluminate. The Royal Society of Chemistry. doi: 10.1039/c3dt32828g.

[24] Ryan M. BOUCK, Ann M. ANDERSON, Chetna PRASAD, Michael E. HAGERMAN and Mary K. CARROLL, Cobalt-Alumina Sol Gels: Effects of Heat Treatment on Structure and Catalytic Ability (2016), Non crystalline solids, https://doi.org/10.1016/j.jnoncrysol.2016.09.013.

[25] A.MRAOUEFEL, Structural and optical properties Studies of solid nanometric solutions of inorganic materials YP1-X VX O4 ($1 \geq x \geq 0$) boosted to the ions of rare Trivalent TB^{3+}, PhD thesis, Badji Mokhtar-Annaba University, 2022.

[26] C.MORIN, Preparation of alumina with controlled porosity: study of the interaction of boehmite in solvents and the functional properties of the resulting materials, PhD thesis, PIERRE et MARIE CURIE University Paris, 2014.

[27] G.BRAHIM, Elaboration and characterisation of thin films of transparent conducting oxides (TCO), PhD thesis, Kasdi Merbah University - OUARGLA, 2022.

[28] H.GHERIB, Préparation, Caractérisation et Activité Catalytique de Nanoparticules de Rhodium, PhD thesis, Université 8 Mai 1945 Guelma, 2022.

[29] A. ZEGADI, Elaboration of $MgAl_2O_4$ spinel from synthesized nanopowders, PhD thesis, Université Ferhat Abbas - Sétif 1, 2019.

[30] S. CHKIRIDA, Nadia ZARI, Abou El Kacem QAISS, and Rachid BOUHFID (2019) Nanocomposite Materials Based on TiO2/Clay for Wastewater Treatment, DOI: 10.1007/978-3-030-02381-2_16

[31] B. AMAL, Study and preparation by soil-gel of nanomaterials based on semiconductor oxides and their applications, PhD thesis, Larbi ben M'hidi Oum el Bouaghi, 2020.

[32] R. AMARI, Study of the doping effect on the physical and chemical properties of semiconductors based on D9ide synthesized by the Sol- Gel Spin Coating technique, PhD thesis, Mohamed Boudiaf University- MSILA, 2020.

[33] M. BRELLA, Development and characterizations of transparent semiconductors in thin layers for technological applications, PhD thesis, Kasdi Merbah-Ouargla university, 2022.

[34] A. GOSSARD, Synthesis of oxides by colloidal sol-gel route: Application to nuclear fuel precursors, PhD thesis, Ecole Nationale Supérieure de Chimie de Montpellier, 2014.

[35] K. ATAMNIA, Synthesis by sol-gel route and characterization of Titanium oxide (TiO_2) Nanostructured: Photocatalysis Applications (2018) PhD thesis, university of 8 Mai 1945 Guelma.

[36] E.OMARI, Synthesis, redox and catalytic properties of polymetallic oxides La Fe1-xMx O_3(M : Cu, Zn, Co), PhD thesis, Mohamed Khider-Biskra University, 2021.

[37] G. SRAÏKI, Development by sol-gel of assembly methods of non-linear optical crystals for laser applications (2017) PhD thesis, Pierre and Marie Curie University.

[38] A.GUERRAM, Green synthesis and characterization of ZNO nanoparticles using extract from Phoenix Dactylifera L and their applications, PhD thesis, Mohamed Khider University - Biskra, 2022.

[39] M.L.BELLA, Elaboration and characterization of structural ceramics based on local materials intended for tap mixers, PhD thesis, Ferhat Abbas University - Sétif 1, 2022.

[40] N.KHALILE, Study of the microwave of zirconia and alumina/zirconia composites: Role of the composition and architecture of materials, PhD thesis, Saint-Etienne mines-A School of IMT, 2023.

[41] N.SALLES, Study of different polymorphs in alumina and transient phases appearing during the first stages of aluminum oxidation. Simulation on a atomic scale by a model with variable loads in strong links, PhD thesis, University of Burgundy, 2014.

[42] A. BOURBIA, Study of the mechanical hardening of metallic materials: al-Al_2O_3, PhD thesis, University of Badji Mokhtar-Annaba, 2010.

[43] F.TALBI, Study of conduction and dielectric rupture phenomena in high alumina ceramics, PhD thesis, Mouloud Mammeri, Tizi-Ozou University, 2010.

[44] A.BENKHELIF, Valorization of ceramics contained in aluminum slag, PhD thesis, Ferhat Abbas University - Sétif 1, 2023.

[45] M.M.ŞOVAR, From tri-isopropoxide to aluminum oxides by chemical deposit in the steam phase: process, composition and properties of the coatings obtained, PhD thesis, Polytechnic University of Bucharest, 2006.

[46] L. LALLEMANT, Obtaining aluminas has transparent polycrystalline dopeds by Spark Plasma Sintering, PhD thesis, University of Lyon, 2012.

[47] N. ROUSSEL, Optimization of nanometric alumina doping and sipper by SPS. Application to transparent ceramics, PhD thesis, Paul Sabatier University - Toulouse III, 2013.

[48] F. FEREY, Thermoluminescence and sintering of the ultra-pure α alumina doped by zirconium, thorium, calcium, or cerium, PhD thesis, National School of Mines of Saint-Etienne, 2002.

[49] H. TOSSOUKPE, Modeling and simulation of the sintering of doped materials and multimaterials at the microstructure scale, PhD thesis, National School of Mines of Saint-Etienne, 2013.

[50] Yan ZENG, Haijun FAN, Haibo GUO, Kaiyong TANG, Zungang WANG, Siyuan ZHANG, Mo ZHOU, Li FU and He FENG (2025) The Influence of Mg Doping in α-Al2O3 Crystals Investigated with First-Principles Calculations and Experiment, Materials, 2025, https://doi.org/10.3390/ma18020407.

[51] S. GALMARINI, U. ASCHAUER , A. TEWARI, Y. AMAN, C. Van GESTEL, P. BOWEN, Atomistic modeling of dopant segregation in α-alumina ceramics: Coverage dependent energy of segregation and nominal dopant solubility (2011) Journal of the European Ceramic Society, doi:10.1016/j.jeurceramsoc.2011.07.010

[52] Mazaher RAMAZANI, Amirhossein Karimi SHARGH, Hossein JAMALI, Fatemeh DAVAR(2025), Effect of Simultaneous Addition of Three SinteringAids: magnesium, lanthanum, and zirconium oxideon the Mechanical and optical properties of AluminaCeramics fabricated by SPS Method, researchsquare, https://doi.org/10.21203/rs.3.rs-6268009/v.

[53] M. BAYARASSOU, Effet des traitements de vieillissement sur l'évolution de la structure et les propriétés mécaniques des fils en alliages d'aluminium (AGS) tréfilés à L'ENICAB, thèse de doctorat, Université Mohamed Khider – Biskra, 2018.

[54] S.LAMOURI, Elaboration et caractérisation des céramiques à base d'alumine, thèse de doctorat, université Ferhat Abbas Sétif, 2018.

[55] M. RENAUX, Contribution à la modélisation du frittage de l'alumine par chauffage microondes, thèse de doctorat, l'universite polytechnique hauts-de-France et de l'insa hauts-de-France, 2021.

[56] Theodore F. BAUMANN, Alexander E. GASH, Sarah C. CHINN, April M. SAWVEL, Robert S. MAXWELL, Joe H. Satcher, Jr (2005) Synthèse d'aérogels d'alumine à grande surface sans utiliser de précurseurs d'alcoxyde. Chem. Mater. https://doi.org/10.1021/cm048800m.

[57] M. HALLASSI, Elaboration, caractérisation et mesure d'activité catalytique et/ou photo catalytique sur des matériaux oxydes binaires et/ou ternaire, thèse de doctorat, Université du 20 Août 1955-Skikda, 2023.

[58] M.BENSLIMANE, Synthèse, structure cristalline, analyse thermique et propriétés magnétiques de complexes à base de lanthanides trivalents et de métaux de transition, thèse de doctorat, université Mentouri de Constantine, 2011.

[59] L.DJOUDI, Synthèse et propriétés d'oxydes mixtes à base de Lanthane, Aluminium et Nickel, thèse de doctorat, université Mohamed Khider-Biskra, 2016.

[60] M.FOUDIA, Contribution à l'étude du rôle de l'eau de structure dans le mécanisme de formation de α-PbO2., thèse de doctorat, université Ferhat Abbas-Sétif, 2011.

[61] I.CHADLI, Synthèse et caractérisation des sels précurseurs Par la méthode sol gel, thèse de doctorat, université Mohamed Khider-Biskra, 2017.

[62] A.AZIZI, Etude par Spectroscopie Infrarouge et Raman de la transition de phase dans le Picrate de Pyridine, thèse de doctorat, université 8 mai 1945 de Guelma, 2016.

[63] S.HAMRI, Etude thermophysique de la diffusion de molécules de bas poids moléculaire dans des réseaux de polymères acryliques, thèse de doctorat, universite Abou Bekr BELKAÏD de Tlemcen, 2013.

[64] W.DERAFA, Synthèse et caractérisation de ligands bases de Schiff et leurs complexes de métaux de transition – Etude électrochimique, élaboration d'électrodes modifiées et tests d'efficacités électrocatalytiques, thèse de doctorat, université Ferhat Abbas –Setif-1 2016.

[65] S. AMARA, Optical and structural characterization of thin layers of complex oxides for photonic applications (2015) PhD thesis, Ferhat Abbas University Setif.

[66] Y. POINTEL, Coordination polymers based on dichlorophthalate: towards a new family of luminescent markers (2020) PhD thesis, Rennes university.

[67] T.MOKRANE, Nanoparticules de nickel supportées sur alumine préparées par le procédé polyol. Structure et propriété de surface, thèse de doctorat, l'Université 08 Mai 1945 Guelma, 2017.

[68] S.SABOUR, Préparation d'un matériau nanostructure de silice alumine fonctionnalises par un métal noble (Rh, Pd, …..), application en oxydation en phase liquide, thèse de doctorat, université Saad DAHLEB de Blida, 2017.

[69] R.BENREDOUANE, Influence des méthodes d'affinement cristallographique sur l'identification-optimisation- quantification- paramétrique des structures cristallines : application aux oxydes $A_3B_3O_7$ (A= R, Ba, Ca / B = Cu, Co, Zn), thèse de doctorat, université des frères MENTOURI de Constantine, 2018.

[70] F.HAIDARA, Étude des mécanismes de formation de phases dans des films minces du système ternaire Al-Cu-Fe, thèse de doctorat, université Paul CEZANNE AIX-Marseille III, 2011.

[71] Bahaa WATHOOK, Dhia A. HASSAN, Shiqing PANG, Xu JIAN (2023) Phase Transformation and Photoluminescence Properties of $MgTiO_3$: Mn^{4+} Synthesis by Modified Sol–Gel Method. Chemistry Africa. https://doi.org/10.1007/s42250-023-00845-7.

[72] M.RIVARD, Imagerie tissulaire par microscopie de seconde harmonique interférométrique, thèse de doctorat, université du Québec, 2016.

[73] A.BOUALEM, Estimation de distribution de tailles de particules par techniques d'inférence bayésienne, thèse de doctorat, université d'Orléans, 2016.

[74] M.DJAAFAR, Elaboration et caractérisation des nanocomposites alumine- SIC, thèse de doctorat, institut national des sciences appliquées Lyon, 2011.

[75] May Yam MOSHKOVITZ, Danielle PAZ, shloumo MAGDASSI (2023) 3D Printing transparent ɤ-Alumina porous structures Based on Photopolymerizable sol-gel lnks. Advanced Materials Technologies. Doi: 10.1002/admt.202300123.

[76] Sakeena H. ALSAIRAFI. N. ALNAJDI. H. ALSHEEHA. Mohan S. RANA (2019) Synthesis of alumina support and effect of its properties on thiophene hydrodesulfurization. Reaction Kinetics, Mechanisms and Catalysis. https://doi.org/10.1007/s11144-019-01706-6.

[77] Fangli YU, Jianfeng YANG, Jingyun MA, Jun DU, Yongqiang ZHOU (2009) Preparation of nanosized $CoAl_2O_4$ powders by sol–gel and sol–gel-hydrothermal methods. Journal of Alloys and Compounds. doi:10.1016/j.jallcom.2008.01.018.

[78] Andrea ROSATI, Michele FEDEL, Stefano ROSSI (2020) NIR reflective pigments to mitigate the urban heat islands effect (UHIE). EDP Sciences. http://doi.org/10.1051/e3sconf/202017203006.

[79] J.A.M. VANHOEK, F.J.J VAN LOO and R. METSELAAR (1991) Phase diagrams of alumina – alkali oxide – earth alkaline oxide systems in relation to alkali corrosion, doi:10.4028/www.scientific.net/KEM.53-55.111

[80] Y. YANG, S.-L. CHEN (2017) Thermodynamic and kinetic modeling of grain boundary equilibrium segregation of P in α-Fe, CALPHAD, http://dx.doi.org/10.1016/j.calphad.2017.04.002

[81] S.A. DECTEROV, I.-H. JUNG, E. JAK, Y.-B. KANG, P. HAYES, and A.D. PELTON (2004) Thermodynamic modelling of the Al_2O_3-CaO-CoO-$CrOCr_2O_3$- FeO-Fe_2O_3-MgO-MnO-NiO-SiO_2-S system and applications in ferrous process metallurgy.

[82] Kent J. WARRENA, Justin T. TRANA, and Alan W. WEIMER (2021) A Thermochemical Study of Iron Aluminate-Based Materials: A Preferred Class for Isothermal Water Splitting, Energy & Environmental Science.

[83] In-Ho JUNG, Youn-Bae KANG, Sergei A. DECTEROV and Arthur D. PELTON (2004) Thermodynamic Evaluation and Optimization of the MnO-Al_2O_3 and MnO-Al_2O_3-SiO_2 Systems and Applications to Inclusion Engineering.

[84] Karin FRISK (1991) A thermodynamic evaluation of the CR-N, FE-N, MO-N and CR-MO-N systems, Calphad, https://doi.org/10.1016/0364-5916(91)90028-I.

[85] Saikat CHATTERJEE, In-Ho JUNG (2014) Critical evaluation and thermodynamic modeling of the Al–Mn–O (Al_2O_3–MnO–Mn_2O_3) system, the European Ceramic Society, https://d1wqtxts1xzle7.cloudfront.net/40613737/dx.doi.org/10.1016/j.jeurceramsoc.2013.12.017.

[86] Bahaa Wathook, Dhia A. Hassan, Shiqing Pang, Xu Jian (2023) Phase Transformation and Photoluminescence Properties of $MgTiO_3$: Mn^{4+} Synthesis by Modified Sol–Gel Method. Chemistry Africa. https://doi.org/10.1007/s42250-023-00845-7.

[87] Shafi'u LAWAL , Yusuf Suleiman DAMBATTA , Laminu SHETTIMA KUBURI , Muhammad USMAN KAISAN (2024) Analysis of physicochemical and tribological properties of nano alumina-based gear oil developed from effluent of lube oil blending plant. Industrial Crops & Products. https://doi.org/10.1016/j.indcrop.2023.117936.

[88] Khadijah Mohammedsaleh KATUBI, Sobia JABEEN, Fatima TARIQ, Amna IRSHAD, Z.A. ALROWAILI , M.S. AL-BURIAHI , Muhammad Farooq WARSI (2024) Harnessing advanced nanomaterials: Wastewater treatment with sustainable approach using 2D g-C_3N_4 based Ho-doped $LaCoO_3$ nanocomposite. Ceramics International. https://doi.org/10.1016/j.ceramint.2024.01.148.

[89] Somia M. ABAD-ELWAHAD, Ali F. BUKHZAM, Gamal A. H. MEKHEMER (2015) A Study of the Precursor Variation on the Surface Characterization of Supported Cobalt Oxide Catalyst. American Journal of Materials Science. doi: 10.5923/s.materials.201501.01.

[90] Rached OUSJI, Mohamed Achraf BOUABDELLAH, Zouhaier KSIBI, Abdelhamid GHORBEL, Céline FONTAINE (2024) Enhancing Low-Temperature HCHO Oxidation: Investigation selectivity and Catalytic Activity of Ag, Co, Mo, and Cr Catalysts Supported on γ-Al_2O_3. Chemistry Africa. https://doi.org/10.1007/s42250-024-00967-6.

[91] Alaa IBRAHIM, Mustafa HAMMADI (2023) Green synthesis of Mn_3O_4 Nanoparticles using chia seeds extract, characterization, and cytotoxicity on the HL-60 cells. History of medicine. https://doi.org/10.17720/2409-5834.v9.1.2023.188.

[92] P.A. PRASHANTH, R.S. RAVEENDRA, R. Hari KRISHNA, S. ANANDA, N.P. BHAGYA,B.M. NAGABHUSHANA, K. LINGARAJU, H. Raja NAIKA (2015) Synthesis, characterizations,

antibacterial and photoluminescence studies of solution combustion-derived α-Al_2O_3 nanoparticles. Journal of Asian Ceramic Societies. http://dx.doi.org/10.1016/j.jascer.2015.07.001.

[93] Mustapha AAZZA, Hammou AHLAFI, Hamou MOUSSOUT, Chadia MOUNIR, Alexandre FADEL, Ahmed ADDAD (2020) Catalytic reduction of nitro-phenolic compounds over Ag, Ni and Co nanoparticles catalysts supported on γ-Al_2O_3. Journal of Environmental Chemical Engineering. https://doi.org/10.1016/j.jece.2020.103707.

[94] Siddhartha SENGUPTA, Koustuv RAY, Goutam DEO (2014) Effects of modifying Ni/Al_2O_3 catalyst with cobalt on the reforming of CH_4 with CO_2 and cracking of CH_4 reactions. international journal of hydrogen energy. http://dx.doi.org/10.1016/j.ijhydene.2014.05.058.

[95] Lingling ZHANG, Lihui DONG, Wujiang YU, Lianjun LIU, Yu DENG, Bin LIU, Haiqin WAN, Fei GAO, Keqin SUN, Lin DONG (2011) Effect of cobalt precursors on the dispersion, reduction, and CO oxidation of CoOx/ɤ-Al_2O_3 catalysts calcined in N_2. Journal of Colloid and Interface Science. doi:10.1016/j.jcis.2010.11.076.

[96] I. Spassova, T. Tsontcheva, N. Velichkova, M. Khristova, D. Nihtianova (2012) Catalytic reduction of NO with decomposed methanol on alumina supported Mn–Ce catalysts. Journal of Colloid and Interface Science. doi:10.1016/j.jcis.2012.01.042.

[97] Sergio Ruiz-MORENO, MaJosé SONEIRA, Rosanna Perez-PUEYO, Practical identification of cobalt-based blue pigments detecting the induced photoluminescence by a He-Ne laser using a Raman spectrometer (2023) journal of raman spectroscopy, DOI: 10.1002/jrs.6636.

[98] L. TRINKLER, B. BERZINA, Z. JEVSJUTINA, J. GRABIS, I. STEINS, C.J. BAILY, Photoluminescence of Al_2O_3 nanopowders of different phases (2012) Optical Materials, http://dx.doi.org/10.1016/j.optmat.2012.03.029.

[99] V.A.A. ESPINOZA, A. LOPEZ, R. NEUMANN, L.P. SOSMAN, S.S. PEDRO, Photoluminescence of divalent cobalt ions in tetrahedral sites of zinc orthotitanate (2017) Journal of Alloys and Compounds, http://dx.doi.org/10.1016/j.jallcom.2017.05.188

[100] Artur Majewski-NAPIERKOWSKI, Vitaliy GORBENKO, Tatiana ZORENKO, Sandra Witkiewicz-ŁUKASZEK and Yuriy ZORENKO, Regularities of Manganese Charge State Formation and Luminescent Properties of Mn-Doped Al_2O_3, $YAlO_3$, and $Y_3Al_5O_{12}$ Single Crystalline Films (2023) crystals, https://doi.org/10.3390/cryst13101481.

[101] Majid FARAHMANDJOU, Nazafarin GOLABIYAN (2015) New pore structure of nano-alumina (Al_2O_3) prepared by sol gel method. Ceramic Processing Research.

[102] Jiawei DU, Le ZHAO, Xinyi ZHANG, Jiangbo WU, Xiaoze DU, Hongwei WU (2024) Synthesis and characterization of absorption-enhanced alumina solid particle materials for direct irradiation solar-thermal conversion. Solar Energy Materials and Solar Cells. https://doi.org/10.1016/j.solmat.2024.112853.

[103] Danila Ferreira NIERO, Oscar Rubem Klegues MONTEDO, Adriano Michael BERNARDIN (2022) Synthesis and characterization of nano α-alumina by an inorganic sol–gel method. Materials Science and Engineering. https://doi.org/10.1016/j.mseb.2022.115690.

[104] Wafaa A. KADHIM, Ahmed L. KHALAF, Rana A. AZEEZ, M.H.Ab. RAHIMA, S.F. HASANY (2020) Effect of Doping Alumina by Nano Mn on the Sensing Applications. Materials Science. https://doi.org/10.4028/www.scientific.net/MSF.1002.273.

[105] Jiaorong YAN, Li WANG, Yun GUO, Yanglong GUO, Qiguang DAI, Wangcheng ZHAN (2021) Comparisons on thermal and water-resistance of Ru and Pd supported on cobalt-doped alumina nanosheets for catalytic combustion of propane. Applied Catalysis A, General, https://doi.org/10.1016/j.apcata.2021.118398.

[106] E. Lo´pez-NAVARRETE, M. OCAN˜A (2004) Aerosol-derived Mn-doped Al_2O_3 pink pigments prepared in the absence of fluxes. Dyes and Pigments. doi:10.1016/j.dyepig.2003.11.004.

[107] Majed ZABIHI, Mohammad Reza TOROGHINEJAD, Ali SHAFYEI (2013) Application of powder metallurgy and hot rolling processes for manufacturing aluminum/alumina composite strips. Materials Science and Engineering A. http://dx.doi.org/10.1016/j.msea.2012.09.103.

[108] Zia Ullah KHAN, Khalida AKHTAR (2023) Facile fabrication of monodispersed α- and γ-Al_2O_3 microspheres through controlled calcination of alumina precursors synthesized by homogeneous precipitation. Dispersion Science and Technology. https://doi.org/10.1080/01932691.2023.2228877.

[109] Yunfei YANG , Xiaolei GUO , Shicheng WANG , Haifeng LU , Haifeng LIU (2024) Experimental research on the compression behavior of ultrafine alumina powders under gas pressurization. Powder Technology. https://doi.org/10.1016/j.powtec.2023.119333.

[110] Bingying XIE, Yizhe LI, Juncheng PAN, David A. HALL (2024) Process optimisation of alumina coatings by modification of powder characteristics in the aerosol deposition method. Journal of the European Ceramic Society. https://doi.org/10.1016/j.jeurceramsoc.2023.12.085.

[111] Sang Woo BYUN, Hyeonwoo SHIN, Wo Bin BAE, Melanie J. HAZLETT, Young JIN KIM, Seong Jun LEE, Minkyu KIM, sung bong KANG (2024) Dry synthesis of alumina-supported cobalt catalyst for highly enhanced catalytic oxidation. Chemical Engineering Journal. https://doi.org/10.1016/j.cej.2023.148316.

[112] Y. El JABBAR, H. LAKHLIF, R. El OUATIB, L. ER-RAKHO, S. Guillemet-FRITSCH B. DURAND (2020) Structure, microstructure, optical and magnetic properties of cobalt aluminate nanopowders obtained by sol-gel process. Non-Crystalline Solids. https://doi.org/10.1016/j.jnoncrysol.2020.120115

[113] Masaaki NAGASHIMA, Koichi MOTOIKE, Motozo HAYAKAWA (2008) Fabrication and optical characterization of high-density Al_2O_3 doped with slight MnO dopant. Ceramic Society of Japan. https://doi.org/10.2109/jcersj2.116.645.

[114] Farah M. ABDUL RAZZAQ, Adnan S. JABUR (2024) Evaluation of α-Alumina Nanoparticles Prepared by Sol-Gel Method. Engineering Sciences. https://doi.org/10.33971/bjes.24.2.1.

[115] Md Farid AHMED, Monmon PODDER, Md. RASSEL MONI, Md. Lutfor RAHMAN, Bristy BISWAS, Juliya KHANAM, Mahmuda HAKIM, Moksodur RAHMAN, Md. Sahadat HOSSAIN, Nahid SHARMIN (2025) Investigation the effect of calcination heating rate on the structural, morphological and color properties of nano Cobalt Aluminate ($CoAl_2O_4$). Heliyon. https://doi.org/10.1016/j.heliyon.2025.e42413.

[116] Jiˇrí SVOBODA, Katarína DRDLÍKOVÁ, Daniel DRDLÍK, Aleš KROUPA, Jan MICHALIˇCKA, Karel MACA (2022) Doping of alumina ceramics by manganese – Thermodynamical and experimental approach. Processing and Application of Ceramics. https://doi.org/10.2298/PAC2201013S.

Abstract

In this thesis work, three alumina-based powders were synthesized by the sol-gel method using aluminum nitrate, manganese nitrate, and cobalt nitrate as precursors, citric acid as a complexing agent, and ethanol as a solvent. After thermal treatment and magnetic stirring, part of the gels underwent simultaneous DTA/TGA analysis, while the remainder was calcined at various temperatures to obtain the final powders. The resulting materials were characterized using FTIR, UV–visible, and photoluminescence spectroscopy, X-ray diffraction (XRD) and microstructural morphology analysis. The analysis results highlights a single α-Al_2O_3 phase for pure alumina (crystallite size ~42 nm). Cobalt-doped alumina showed two distinct phases, Co_3O_4 and Co_2AlO_4, with an average crystallite size of 48 nm, while manganese-doped alumina exhibited a multiphase structure (Mn_3O_4, α-Al_2O_3, and γ- Al_2O_3) with the smallest crystallite size of 24 nm.

Keywords : Alumina, Cobalt, Manganese, Sol-gel, Doped.

Résumé

Dans ce travail de thèse, trois poudres à base d'alumine ont été synthétisées par la méthode sol-gel en utilisant le nitrate d'aluminium, le nitrate de manganèse et le nitrate de cobalt comme précurseurs, l'acide citrique comme agent complexant et l'éthanol comme solvant. Après traitement thermique et agitation magnétique, une partie des gels a subi une analyse ATD/ATG simultanée, tandis que le reste a été calciné à différentes températures pour obtenir les poudres finales. Les matériaux résultants ont été caractérisés par spectroscopie FTIR, UV-visible et photoluminescence, diffraction des rayons X (XRD) et analyse de la morphologie microstructurale. Les résultats de l'analyse mettent en évidence une seule phase α-Al_2O_3 pour l'alumine pure (taille des cristallites ~42 nm). L'alumine dopée au cobalt présentait deux phases distinctes, Co_3O_4 et Co_2AlO_4, avec une taille moyenne de cristallite de 48 nm, tandis que l'alumine dopée au manganèse présentait une structure multiphasée (Mn_3O_4, α-Al_2O_3 et γ-Al_2O_3) avec la plus petite taille de cristallite de 24 nm.

Mots clés : Dopage, Alumine, Cobalt, Manganèse, Sol-Gel.

الملخص

في هذه الأطروحة، تم تصنيع ثلاثة مساحيق أساسها الألومينا بطريقة السول-جل باستخدام نترات الألومنيوم ونترات المنغنيز ونترات الكوبالت كمواد أولية، وحمض الستريك كعامل معقد والإيثانول كمذيب. بعد المعالجة الحرارية والتحريك المغناطيسي، خضع جزء من المواد الهلامية لتحليل DTA/TGA في وقت واحد، بينما تم تحميص الباقي في درجات حرارة مختلفة للحصول على المساحيق النهائية. تم توصيف المواد الناتجة بواسطة FTIR، والتحليل الطيفي للأشعة فوق البنفسجية والمرئية والضوئية، وحيود الأشعة السينية (XRD)، وتحليل البنية المجهرية. تسلط نتائج التحليل الضوء على طور α-Al_2O_3 واحد للألومينا النقية (حجم البلورة ~ 42 نانومتر). أظهرت الألومينا المشبعة بالكوبالت طورين متميزين، Co_3O_4 وCo_2AlO_4، بمتوسط حجم بلوري يبلغ 48 نانومتر، بينما أظهرت الألومينا المشبعة بالمنجنيز بنية متعددة الأطوار (Mn_3O_4، α-Al_2O_3، و γ-Al_2O_3) مع أصغر حجم بلوري يبلغ 24 نانومتر.

الكلمات المفتاحية: الألومينا، الكوبالت، المنغنيز، السول -جل، الألومينا المشبعة.